https://technobius.kz/

e-ISSN
2789-7338

Technobius

A peer-reviewed open-access journal

Technobius, LLP ***Volume 6, No. 1, 2026***

Technobius

Volume 6, No. 1, 2026

A peer-reviewed open-access journal registered by the Ministry of Culture and Information of the Republic of Kazakhstan, Certificate № KZ26VPY00087928 dated 21.02.2024

ISSN (Online): 2789-7338
Thematic Directions: Construction, Materials Science
Publisher: Technobius, LLP
Address: 2 Turkestan street, office 116, 010000, Astana, Republic of Kazakhstan

Contacts:
Website: https://technobius.kz/
E-mail: technobius.research@gmail.com

CONTENTS

Technobius, 2026, 6(1), 0095, DOI: https://doi.org/10.54355/tbus/6.1.2026.0095

Technobius

https://technobius.kz/

e-ISSN 2789-7338

Article

Microstructural transition and densification behavior of modified soil: a quantitative SEM study

Assel Tulebekova[1], Natalya Ryvkina[1], Dauren Yessentay[2,*], Akmaral Yeleussinova[1]

[1]Department of Civil Engineering, L.N. Gumilyov Eurasian National University, Astana, Kazakhstan
[2]Department of Transportation Engineering and Building Materials Production, L.B. Goncharov Kazakh Automobile and Road Institute, Almaty, Kazakhstan
*Correspondence: yessentaydauren063@gmail.com

Abstract: This study investigates the microstructural transition and densification behavior of soil modified by xanthan gum (XG) using quantitative scanning electron microscopy (SEM) analysis. Soil specimens were prepared with 0%, 3%, 6%, and 9% XG content. SEM images were processed using image analysis techniques to determine the solid area fraction and characteristic particle size parameters. A densification index was introduced to quantify the ratio between solid and pore phases within the observed microstructure. The results reveal a non-monotonic structural evolution with increasing polymer content. The solid area fraction reached its maximum at 3%, indicating the most pronounced local densification of the particle structure within the analyzed micrographs. At 6%, a reduction in densification was observed, reflecting a change in particle packing configuration and the development of a more heterogeneous microstructural arrangement. At 9%, partial recovery of structural continuity occurred, accompanied by evidence of polymer agglomeration and spatial heterogeneity. Based on quantitative metrics and microstructural observations, three structural stages were identified: discrete particle stage, bridged stage, and matrix-dominated stage. The findings demonstrate that XG dosage significantly influences soil microstructure in a nonlinear manner. This SEM-based approach provides a systematic framework for identifying microstructural transitions in biopolymer-modified soils.
Keywords: xanthan gum, soil stabilization, microstructural transition, scanning electron microscopy, densification index.

1. Introduction

Soil stabilization is widely applied in geotechnical engineering to enhance the mechanical and hydraulic performance of problematic soils. Conventional stabilization techniques commonly involve cement or lime; however, these additives may significantly increase environmental impact and alter soil chemistry. In response to sustainability concerns, polymer-based treatments have attracted growing attention as an alternative ground improvement strategy [1].

Polymers interact with soil particles primarily through physicochemical mechanisms, including surface coating, interparticle bonding, and partial pore filling [2]. These interactions can alter particle packing and modify the internal microstructure without forming rigid cementitious bonds [3]. The resulting structural changes depend strongly on polymer concentration and distribution within the soil matrix. Therefore, quantitative evaluation of microstructural modifications is essential for understanding the mechanisms governing polymer-stabilized soils. Natural biopolymers such as chitosan, xanthan gum (XG), guar gum, carboxymethylcellulose, alginates, and modified starches, as well as their mixed compositions, are used as polymeric soil stabilizers, forming a spatial binding matrix in the pore space of the soil [4]. Among various biopolymers, XG has been extensively investigated for its ability to enhance soil strength and modify plasticity characteristics. Experimental studies [5] demonstrated that XG treatment increases compressive strength and cohesion, with performance strongly dependent on polymer dosage and curing conditions. Durability evaluations under cyclic wetting-drying further showed that treated soils generally retain higher residual strength than untreated materials, highlighting the practical potential of XG for geotechnical applications.

The influence of environmental weathering on biopolymer-treated soils has also been systematically examined. [6] investigated the effects of cyclic wetting-drying (W-D) and freezing-thawing (F-T) on strength durability and reported that repeated cycles gradually reduced soil strength due to water adsorption and localized dilution of the biopolymer matrix. Poorly graded sands were found to be more vulnerable to degradation; however, the presence of 15-25% fines significantly improved resistance to weathering.

Despite progressive strength loss, treated soils maintained sufficient durability under multiple W-D and F-T cycles, supporting their suitability for slope reinforcement applications. From a mechanistic perspective, XG acts as a biodegradable polysaccharide that interacts with soil particles through physicochemical bonding. [3] demonstrated that XG forms rigid matrix-like structures between uncharged grains while interacting with charged clay surfaces, thereby enhancing interparticle bonding and overall stability. The reinforcement efficiency was shown to be highest in well-graded soils containing fine particles and was governed by several key parameters, including soil type, moisture content, biopolymer concentration, and mixing method. These findings underline the importance of optimizing mixture design to achieve maximum performance.

Beyond laboratory-scale assessments, the internal erosion resistance of biopolymer-treated soils has been evaluated under full-scale embankment conditions. [7] examined the performance of soils treated with 1% XG through both laboratory and field-scale simulations. The results indicated that 1% XG provided optimal improvements in plasticity and mechanical strength. In full-scale seepage tests beneath a box culvert, untreated embankments collapsed within 1,500 s, whereas XG-treated embankments remained stable up to 2500 s due to enhanced particle bonding, increased apparent cohesion, and pore clogging. These outcomes demonstrate that even low biopolymer dosages can substantially improve embankment durability.

The effectiveness of XG has also been confirmed for highly vulnerable dispersive soils. [8] evaluated the long-term performance of XG-treated dispersive soils subjected to adverse environmental conditions using unconfined compressive strength (UCS) and cyclic wetting-drying tests. Significant strength gains were observed, with UCS increasing by 177% and 95% after 360 days for 2 soil types. After 12 wetting-drying cycles, mass loss values remained below the permissible 14% limit (9.76% and 7.04%), indicating satisfactory durability. So, although cyclic weathering influences strength degradation, XG treatment markedly enhances the long-term stability and erosion resistance of dispersive soils.

Overall, microstructural investigation has become an important approach for understanding the mechanisms of soil stabilization. Quantitative analysis of soil microstructure based on SEM images is increasingly applied in geotechnical research to characterize particle aggregation, pore distribution, and structural densification [9], [10]. Digital image processing tools [11] enable the extraction of geometric parameters, including pore area, particle size, and morphological characteristics from SEM images, allowing a more detailed interpretation of microstructural changes in modified soils.

In this study, SEM images were processed using ImageJ software to quantitatively evaluate the microstructural characteristics of polymer-modified soil. The analysis focuses on parameters describing particle arrangement and structural heterogeneity. Special attention is given to the evolution of particle packing, characteristic diameters (D10, D50, D90), and structural homogeneity under various polymer contents. By linking microstructural metrics with macroscopic behavior, this research provides deeper insight into the mechanisms governing polymer-based soil stabilization.

2. Methods

The soil used in this study was collected from the Astana region, Kazakhstan. It was taken from the subsurface layer at a depth of approximately 0.5-1.0 m, which corresponds to the typical depth of the engineering soil layer involved in shallow foundation systems and earth structures. The material was air-dried and prepared for laboratory testing under controlled conditions. The particle density of the soil was 2671 kg/m^3, with a maximum dry density of 1547 kg/m^3 and an optimum water content of 9.61% [12]. Particle size distribution analysis indicated that the soil contains 48% sand, 21% silt, and 31% clay [13]. Based on its granulometric composition, the tested soil is classified as sandy clay loam. The Atterberg limits showed a liquid limit of 19.36% and a plastic limit of 3.17%, resulting in a plasticity index of 16.19%, which reflects moderate plasticity behavior.

XG was selected as the biopolymer additive for soil stabilization in this study. Biopolymer solutions of XG were prepared at concentrations of 3%, 6%, and 9% by weight relative to 100 g of oven-dried soil (hereinafter referred to as XG3, XG6, XG9). Accordingly, 3 g, 6 g, and 9 g of XG were dissolved in distilled water to obtain homogeneous polymer solutions before mixing with the soil. The prepared solutions were then thoroughly blended with the dry soil to ensure uniform distribution of the biopolymer within the soil matrix.

Scanning electron microscopy (SEM) observations were performed using a TM4000Plus scanning electron microscope (Hitachi High-Tech Corporation, Tokyo, Japan). The analysis was carried out under an accelerating voltage of 15 kV in high-vacuum mode using the secondary electron detector to observe the surface morphology of the soil samples.

The preparation process of the sample is presented in Figure 1.

Figure 1 – Sample preparation with polymer mixing and SEM image acquisition

The obtained SEM images served as the foundation for subsequent quantitative image analysis. The acquired micrographs were then imported into ImageJ open software (version 1.53, National Institutes of Health, Bethesda, MD, USA) for quantitative processing. Each image was converted to grayscale and pre-processed using standard noise-reduction and contrast-adjustment steps to improve phase separation. Each SEM image was automatically subdivided into 30 equal regions (each measuring 213×180 pixels) using a standardized grid-based approach implemented in ImageJ. The subdivision was generated programmatically, without manual selection of areas, thereby eliminating operator bias and ensuring reproducible spatial sampling across all samples.

Morphometric analysis was performed independently within each region using the «Analyze Particles» function under identical thresholding parameters for all mixtures. Particle size was quantified using the major axis diameter of detected particles. Size distribution descriptors (D10, D50, and D90) were calculated from the cumulative distribution of measured diameters for each mixture (n=30 regions per condition). To quantitatively evaluate microstructural compactness, a densification index (DI) was introduced based on the measured solid area fraction obtained from SEM image analysis. The densification index was defined as:

$$DI = \frac{AF}{1-AF} \tag{1}$$

Where: AF – denotes the solid area fraction expressed as a decimal value; (1 − AF) – represents the corresponding pore fraction.

This ratio characterizes the relative predominance of the solid phase over the void phase within the analyzed microstructure. The solid area fraction (AF) was determined from segmented SEM images using ImageJ software and represents the proportion of the image occupied by soil particles. AF was calculated as:

$$AF = \frac{A_{soild}}{A_{total}} \quad (2)$$

Where: A_{solid} – represents the total projected area of the solid particles identified within the segmented SEM image; A_{total} – denotes the total area of the analyzed field of view.

After grayscale conversion and threshold-based segmentation, binary images were generated to distinguish the solid particle phase from the pore phase. The total analyzed image area (A_{total}) was obtained directly from the image dimensions. This parameter represents the proportion of the microstructural field occupied by the solid phase and serves as a two-dimensional approximation of packing density. A higher DI value indicates that the solid phase occupies a larger proportion of the observed section compared to pores, suggesting a denser particle arrangement. Conversely, lower DI values reflect increased void space and a more open structural configuration.

For each mixture, particle size measurements obtained from the segmented SEM images were statistically processed. The standard deviation (STDV) was calculated to assess the absolute dispersion of particle diameters, while the coefficient of variation (CV) was determined to evaluate the relative heterogeneity of the microstructure. The CV was computed as the ratio of the standard deviation to the mean particle diameter, allowing comparison between compositions with different average particle sizes. All calculations were performed using data extracted from 30 uniformly subdivided image segments.

3. Results and Discussion

SEM micrographs reveal distinct differences in particle arrangement with increasing XG content (Figure 1). The untreated soil exhibits a loose configuration characterized by visible interparticle voids and limited bonding between grains.

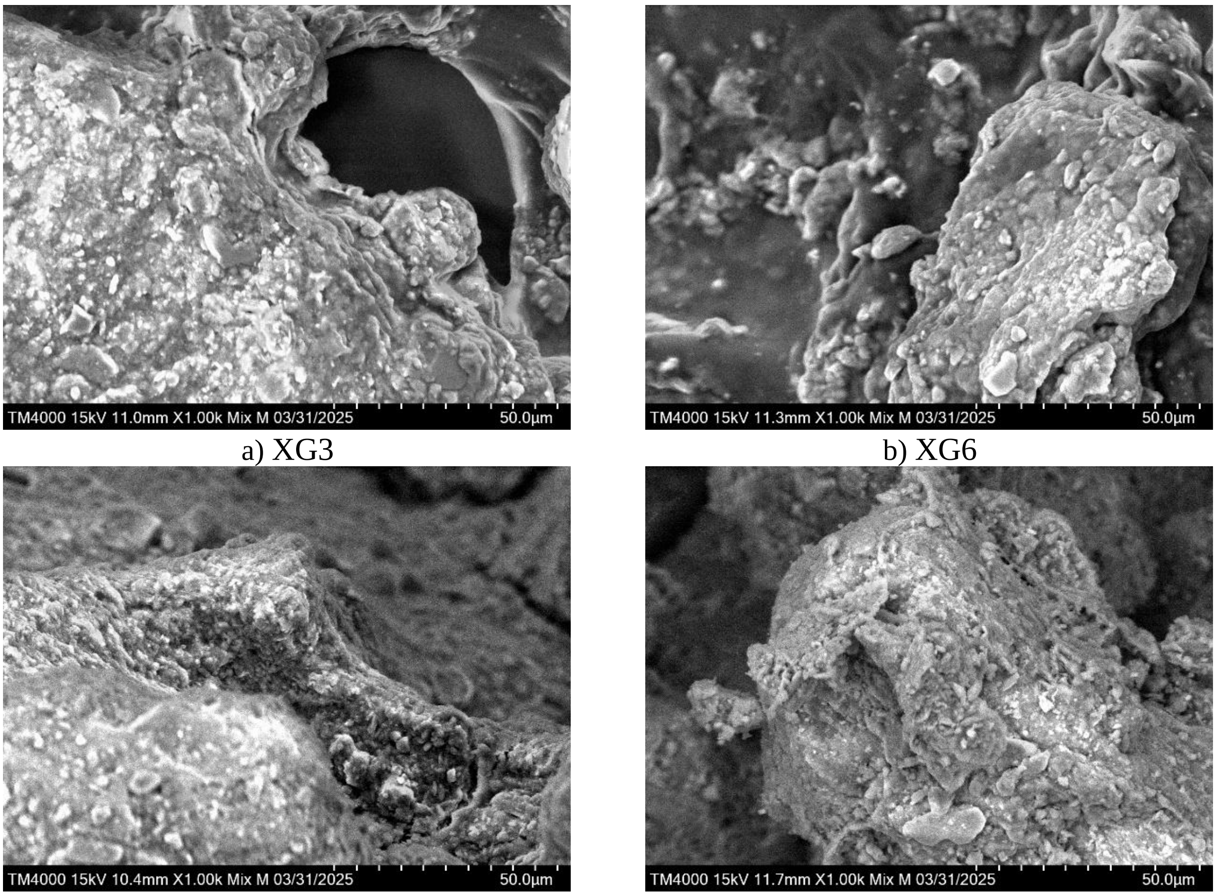

a) XG3 b) XG6

c) XG9 d) Unmodified soil

Figure 1 – SEM images of modified soil

At 3% polymer content, a more interconnected structure is observed, with evidence of particle clustering and reduced visible pore space. The 6% sample shows irregular particle distribution with localized dense regions separated by relatively open areas. At 9%, the microstructure appears more heterogeneous, with clustered particle domains and regions of enlarged voids. These visual differences suggest progressive structural modification associated with polymer incorporation.

Binary representations of the SEM images demonstrate clear separation between the solid particle phase and pore spaces across all compositions (Figure 2).

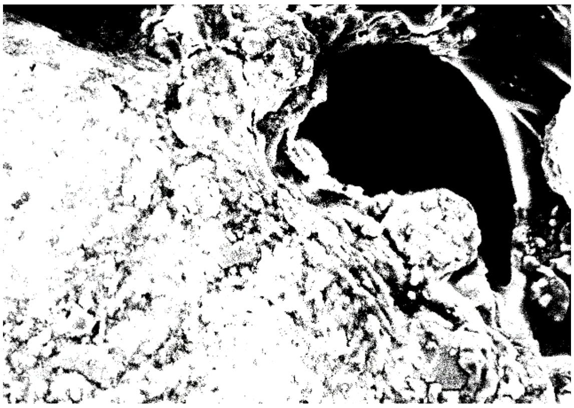

a) XG3

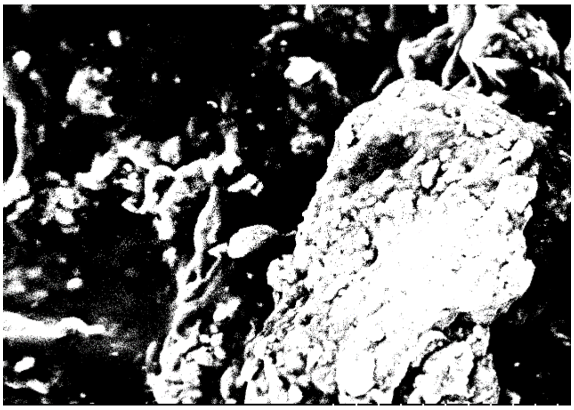

b) XG6

c) XG9

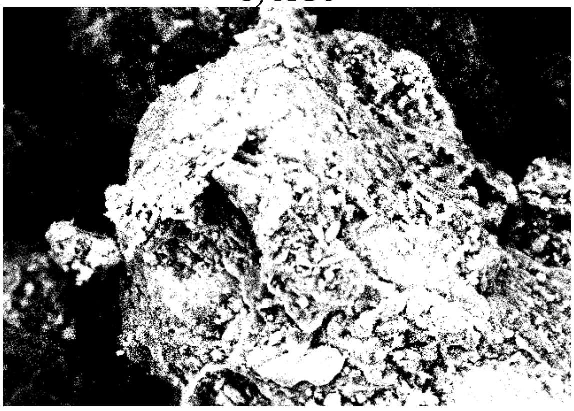

d) Unmodified soil

Figure 2 – Binary representations of the SEM images of modified soil

In untreated conditions, dark regions corresponding to voids are more widely distributed throughout the microstructural field. The segmented images provide the basis for quantitative area-based evaluation.

Table 1 presents the microstructural size distribution parameters for untreated and XG-modified soil samples at different polymer contents. The characteristic diameters D10, D50, and D90 reflect the statistical distribution of particle assemblies observed within the SEM field of view.

Table 1 – Microstructural size parameters obtained from SEM image analysis

Polymer content, %	n	D10, µm	D50, µm	D90, µm
0	30	1.925	7.435	8.480
3	30	4.716	7.066	8.605
6	30	4.786	7.326	9.229
9	30	1.770	6.033	8.858

Progressive variation in these parameters indicates that polymer incorporation alters the spatial arrangement of soil particles. In particular, the increase in D50 values with increasing XG content changes the representative structural scale of particle clusters. The differences between D10 and D90 demonstrate shifts in distribution breadth across the tested compositions. These parameters provide a quantitative basis for assessing microstructural modification induced by polymer treatment.

Table 2 summarizes the area-based structural metrics for untreated and XG-modified soil samples.

Table 2 – Derived densification metrics based on SEM area measurements

Polymer content, %	AF	DI
0	0.479	0.92
3	0.575	1.36
6	0.392	0.65
9	0.487	0.95

The solid area fraction (AF) increased from 0.479 in the untreated soil to 0.575 at 3% polymer content, indicating enhanced structural densification at this concentration. This composition exhibited the highest compactness among the tested mixtures.

At 6% polymer content, AF decreased significantly to 0.392, suggesting the formation of additional voids or structural heterogeneity, possibly due to polymer over-saturation. At 9%, the solid fraction partially recovered to 0.487, approaching the value of the untreated soil, which indicates partial structural reorganization rather than further densification (Figure 3).

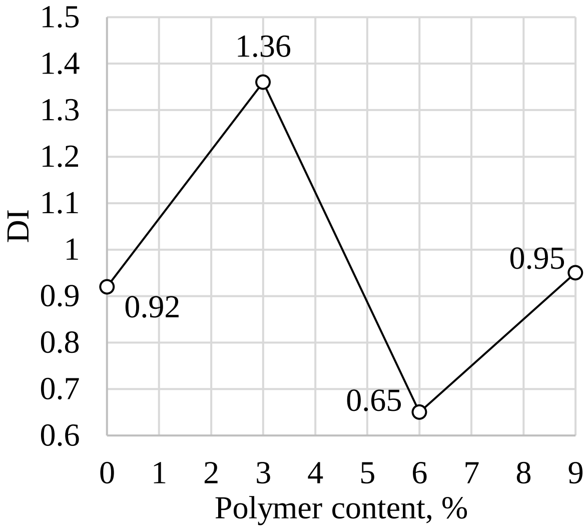

Figure 3 – Variation of densification index with XG content

A similar trend was observed for the densification index. The DI reached its maximum value of 1.36 at 3%, decreased substantially to 0.65 at 6%, and increased again to 9%, although it remained below the peak level. These results indicate a non-linear variation in the solid-to-void relationship with increasing XG dosage. Based on the calculated densification index (DI) values, four structural conditions can be distinguished. The untreated soil (DI = 0.92) represents a discrete particle arrangement characterized by a baseline solid-to-void ratio. A polymer content of 3% (DI = 1.36) produces the most compact structural state, indicating enhanced particle bridging and improved packing efficiency. Increasing the polymer content to 6% leads to a pronounced reduction in the densification index (DI = 0.65), suggesting decreased structural compactness and possible formation of additional voids due to over-saturation or local agglomeration effects. Further increase to 9% results in partial recovery of DI (0.95), approaching the untreated condition. This behavior reflects structural reorganization rather than progressive densification and is consistent with the microstructural heterogeneity observed in SEM images. The statistical dispersion analysis revealed distinct differences in structural variability among the tested polymer contents (Figure 4).

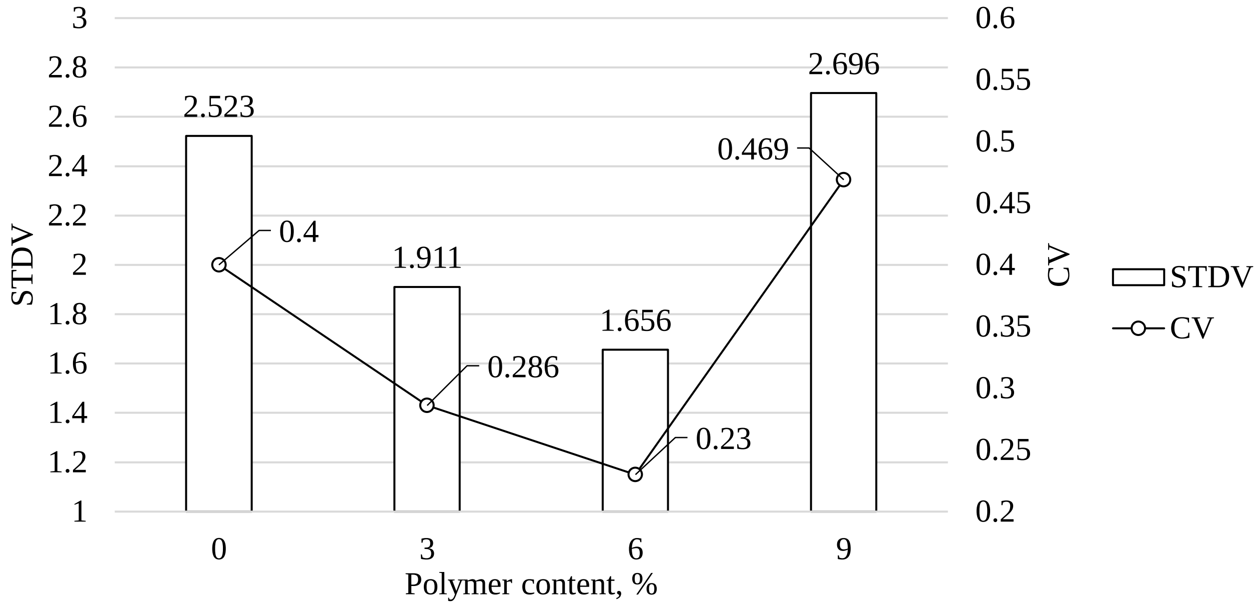

Figure 4 – Variation of particle size dispersion parameters as a function of polymer content

The untreated soil exhibited a standard deviation of 2.523, representing the baseline level of particle size dispersion. The addition of 3% polymer reduced the standard deviation to 1.911, indicating partial structural stabilization. The lowest variability was observed at 6% polymer content (SD = 1.656; CV = 0.230), suggesting the highest degree of microstructural uniformity among the investigated compositions. In contrast, the 9% condition demonstrated a marked increase in dispersion (SD = 2.696), accompanied by the highest coefficient of variation, reflecting structural heterogeneity at elevated polymer dosage.

These results indicate that maximum densification does not necessarily coincide with maximum structural homogeneity. While 3% polymer content yielded the highest compactness according to the densification index, the 6% mixture exhibited the most uniform particle distribution, as reflected by the lowest variability. This suggests that increasing polymer concentration affects not only the degree of particle packing but also the spatial organization of particle assemblies.

The observed microstructural evolution is consistent with trends reported in previous studies on XG-treated soils [14]. Earlier investigations have shown that the improvement of soil properties with increasing XG dosage tends to stabilize after reaching an optimal concentration. For example, studies on silty soils [15] reported that the UCS increased with polymer content but eventually approached a stable state at an optimal dosage of approximately 2%. SEM observations in those studies indicated that XG forms a gel-like matrix that fills pore spaces and enhances the compactness and integrity of the soil structure. These findings are consistent with the present results, where the highest densification was observed at moderate polymer dosage.

In the present study, the formulation of the densification index follows the fundamental concept of solid-void relationships commonly used in soil mechanics, adapted here to a two-dimensional SEM-based framework to enable consistent comparison between samples with different polymer contents.

It should be noted that the present study is limited to SEM-based microstructural evaluation. Therefore, the findings are confined to structural characterization at the microscale. The results contribute to a clearer understanding of dosage-dependent structural transitions in XG-modified soils and provide a quantitative framework for future studies integrating mechanical testing and durability assessment.

Beyond their geotechnical relevance, the obtained results may also support educational applications within digital learning environments. The quantified microstructural transitions identified in this study can be integrated into a soil mechanics module of an educational digital platform, enabling students to explore the relationship between polymer dosage and structural configuration. The combination of SEM visualization and area-based quantitative metrics provides an effective framework for developing interactive simulation scenarios. Such simulations may allow users to compare untreated and polymer-modified soils, analyze phase distribution patterns, and interpret densification behavior based on measurable parameters.

4. Conclusions

The results demonstrate that polymer dosage significantly influences the internal structure of the soil, leading to a dosage-dependent microstructural evolution. The main findings can be summarized as follows:

1. The untreated soil exhibited a dispersed particle arrangement with clearly distinguishable voids between individual grains. The addition of xanthan gum gradually modified the soil fabric, promoting particle association and altering the connectivity of pore spaces.
2. Binary segmentation analysis revealed distinct changes in the spatial distribution of solid and void phases. Compared with the untreated soil, polymer-treated samples showed increased interaction between soil particles and the biopolymer matrix, although the spatial organization of solid regions varied depending on polymer concentration.
3. Quantitative evaluation of the image-derived parameters indicated a non-linear response of microstructural characteristics to increasing polymer content. Variations in the densification index and phase distribution suggest that different polymer concentrations influence both particles packing and the spatial arrangement of particle clusters.

The results indicate that xanthan gum addition alters both the degree of particle aggregation and the structural organization of the soil matrix. These findings highlight that microstructural densification and structural uniformity may develop differently depending on polymer dosage.

Acknowledgments

This research has been/was/is funded by the Science Committee of the Ministry of Science and Higher Education of the Republic of Kazakhstan (Grant No. AP26195121 «Development of an educational digital platform for future builders with simulation of construction processes and integration with measuring devices via IoT»).

References

[1] J. Jang, “A Review of the Application of Biopolymers on Geotechnical Engineering and the Strengthening Mechanisms between Typical Biopolymers and Soils,” *Advances in Materials Science and Engineering*, vol. 2020, no. 1, p. 1465709, Jan. 2020, doi: 10.1155/2020/1465709.

[2] A. Tulebekova, Z. Kusbergenova, B. Dosmukhambetova, T. Abilmazhenov, and I. Zhumadilov, “Study of the impact of biopolymer and geosynthetics reinforcement on soil strengthening,” *EUREKA: Physics and Engineering*, no. 6, pp. 70–80, Nov. 2024, doi: 10.21303/2461-4262.2024.003472.

[3] I. Chang *et al.*, “Review on biopolymer-based soil treatment (BPST) technology in geotechnical engineering practices,” *Transportation Geotechnics*, vol. 24, p. 100385, Sep. 2020, doi: 10.1016/j.trgeo.2020.100385.

[4] M. Azimi, A. Soltani, M. Mirzababaei, M. B. Jaksa, and N. Ashwath, “Biopolymer stabilization of clayey soil,” *Journal of Rock Mechanics and Geotechnical Engineering*, vol. 16, no. 7, pp. 2801–2812, Jul. 2024, doi: 10.1016/j.jrmge.2023.12.020.

[5] P. Bagheri, I. Gratchev, and M. Rybachuk, “Effects of Xanthan Gum Biopolymer on Soil Mechanical Properties,” *Applied Sciences*, vol. 13, no. 2, p. 887, Jan. 2023, doi: 10.3390/app13020887.

[6] M. Lee, Y.-M. Kwon, D.-Y. Park, I. Chang, and G.-C. Cho, “Durability and strength degradation of xanthan gum based biopolymer treated soil subjected to severe weathering cycles,” *Scientific Reports*, vol. 12, no. 1, p. 19453, Nov. 2022, doi: 10.1038/s41598-022-23823-4.

[7] Y.-M. Kwon, J.-H. Moon, G.-C. Cho, Y.-U. Kim, and I. Chang, “Xanthan gum biopolymer-based soil treatment as a construction material to mitigate internal erosion of earthen embankment: A field-scale,” *Construction and Building Materials*, vol. 389, p. 131716, Jul. 2023, doi: 10.1016/j.conbuildmat.2023.131716.

[8] J. J. Reddy and B. J. S. Varaprasad, “Long-term and durability properties of xanthan gum treated dispersive soils – An eco-friendly material,” *Materials Today: Proceedings*, vol. 44, pp. 309–314, 2021, doi: 10.1016/j.matpr.2020.09.472.

[9] C.-S. Tang *et al.*, "Quantification and characterizing of soil microstructure features by image processing technique," *Computers and Geotechnics*, vol. 128, p. 103817, Dec. 2020, doi: 10.1016/j.compgeo.2020.103817.
[10] N. Ural, "The significance of scanning electron microscopy (SEM) analysis on the microstructure of improved clay: An overview," *Open Geosciences*, vol. 13, no. 1, pp. 197–218, Feb. 2021, doi: 10.1515/geo-2020-0145.
[11] G. Di Remigio, I. Rocchi, and V. Zania, "New method for a SEM-based quantitative microstructural clay analysis - MiCA," *Applied Clay Science*, vol. 214, p. 106248, Nov. 2021, doi: 10.1016/j.clay.2021.106248.
[12] "GOST 5180-2015 Soils. Laboratory methods for the determination of physical characteristics," Moscow, Russia: Standartinform, 2015, p. 24.
[13] "GOST 25100-2020, Soils. Classification," Moscow, Russia: Standartinform, 2020, p. 38.
[14] I. Chang, J. Im, A. K. Prasidhi, and G.-C. Cho, "Effects of Xanthan gum biopolymer on soil strengthening," *Construction and Building Materials*, vol. 74, pp. 65–72, Jan. 2015, doi: 10.1016/j.conbuildmat.2014.10.026.
[15] X. Zhang, W. Cao, and X. Zhang, "Experimental study on mechanical and hydraulic properties of xanthan gum improved low liquid limit silty soil," *Scientific Reports*, vol. 14, no. 1, p. 11072, May 2024, doi: 10.1038/s41598-024-61875-w.

Information about authors:
Assel Tulebekova – PhD, Professor, Department of Civil Engineering, L.N. Gumilyov Eurasian National University, Astana, Kazakhstan, azeliyatul@gmail.com
Natalya Ryvkina – Master of Sciences, Senior Lecturer, Department of Civil Engineering, L.N. Gumilyov Eurasian National University, Astana, Kazakhstan, rondv2@mail.ru
Dauren Yessentay – PhD, Associate Professor, Department of Transportation Engineering and Building Materials Production, L.B. Goncharov Kazakh Automobile and Road Institute, Almaty, Kazakhstan, yessentaydauren063@gmail.com
Akmaral Yeleussinova – Candidate of Technical Sciences, Associated Professor, Department of Civil Engineering, L.N. Gumilyov Eurasian National University, Astana, Kazakhstan, yeleussinova70@mail.ru

Author Contributions:
Assel Tulebekova – concept, methodology, testing, modeling, analysis, funding acquisition.
Natalya Ryvkina – concept, editing, funding acquisition.
Dauren Yessentay – resources, data collection, analysis.
Akmaral Yeleussinova – methodology, visualization, interpretation, drafting.

Conflict of Interest: The authors declare no conflict of interest.

Use of Artificial Intelligence (AI): AI were used to assist in literature screening and language refinement. All content was critically reviewed, verified, and edited by the authors to ensure accuracy and scientific integrity.

Received: 16.11.2025
Revised: 10.03.2026
Accepted: 12.03.2026
Published: 12.03.2026

Technobius, 2026, 6(1), 0096, DOI: https://doi.org/10.54355/tbus/6.1.2026.0096

Technobius

https://technobius.kz/

e-ISSN 2789-7338

Article

Refined analytical formulation for static bending and free vibrations of functionally graded beams

Sungat Akhazhanov, Aizhan Nurgoziyeva*, Kiyas Kutimov

Research Laboratory Applied Mechanics and Robotics, Buketov Karaganda National Research University, Karaganda, Republic of Kazakhstan

*Correspondence: aizhanzhanabai@gmail.com

Abstract. This paper presents a refined analytical theory for the bending and free vibration analysis of functionally graded (FG) beams accounting for transverse shear deformation. The material properties are assumed to vary continuously through the thickness according to a power-law distribution. Based on the adopted kinematic assumptions, the governing differential equations and effective stiffness relations are derived for both static and dynamic problems. Analytical solutions for the static bending of an FG beam under a uniformly distributed load and for the natural frequencies of free vibrations are obtained. A parametric study is performed to evaluate the influence of the material gradient index p and the beam slenderness ratio l/h. The results show that the dimensionless mid-span deflection increases from 6.2586 to 9.6986 when the gradient index changes from $p = 1$ to $p = 5$ for $l/h = 5$. The corresponding dimensionless natural frequency decreases from 3.9710 to 3.4025. Comparisons with the Timoshenko beam theory, Reddy's higher-order theory, and other refined models demonstrate very good agreement, with differences typically not exceeding 3-5%. The proposed formulation provides a realistic distribution of transverse shear stresses and converges to classical beam solutions for slender beams. The developed model can be effectively applied in the analysis and design of engineering structures made of functionally graded materials.

Keywords: functionally graded beam, shear deformation theory, static bending analysis, free vibration analysis, transverse shear stress, refined beam theory.

1. Introduction

Functionally graded materials (FGMs) constitute a class of composite materials characterized by a continuous variation of mechanical properties according to a prescribed distribution law, most commonly through the thickness of a structural element. In contrast to conventional laminated composites, which are characterized by distinct phase interfaces, FGMs provide a smooth variation of constituent volume fractions, thereby significantly reducing stress concentrations and eliminating the risk of delamination. Among various types of FGMs, metal-ceramic systems are the most widely employed, combining the high thermal resistance of the ceramic phase with the ductility and toughness of the metallic component [1].

The increasing implementation of functionally graded beams and plates in aerospace, energy, and civil engineering applications has created a strong demand for reliable theoretical models capable of accurately describing their static and dynamic behavior. Although exact solutions based on two-dimensional elasticity theory provide high accuracy, they are associated with substantial mathematical complexity and computational cost. Consequently, approximate beam theories have gained widespread application for practical analysis [2].

The classical Euler-Bernoulli beam theory (CBT) neglects transverse shear deformation and assumes that cross-sections remain plane and perpendicular to the neutral axis after deformation. As a result, this theory is generally applicable only to slender beams. To overcome this limitation, Timoshenko beam theory incorporates transverse shear deformation and allows independent rotation of the cross-sections. However, it assumes a constant shear strain distribution through the beam thickness and therefore requires the introduction of a shear correction factor to accurately predict transverse shear stresses [3]. To overcome these limitations, refined and higher-order shear deformation theories have been extensively developed in recent years.

A considerable amount of research has been devoted to the development of refined analytical and numerical models for the bending, buckling, and vibration analysis of functionally graded beams. The theoretical foundations of many higher-order structural models originate from the well-known higher-order shear deformation theory proposed by Reddy for laminated composite plates [4]. In this theory, a higher-order polynomial distribution of transverse shear strains through the thickness is assumed, which allows a more realistic representation of shear effects and automatically satisfies the zero transverse shear stress conditions on the top and bottom surfaces without the need for a shear correction factor. Later studies extended these concepts to structures with continuously varying material properties.

An exact elasticity solution for functionally graded beams was presented in [5], where the influence of material gradation on stress distribution and displacement fields was examined in detail. The free vibration characteristics of simply supported functionally graded (FG) beams were investigated in [6], demonstrating that the gradient index of material properties plays a significant role in determining the natural frequencies.

Further developments in the literature introduced refined beam formulations capable of accurately capturing shear deformation effects. A refined shear deformation theory suitable for the static and vibration analysis of FG beams was developed in [7], showing that reliable results can be obtained without employing shear correction factors. The applicability of this approach was later extended to sandwich configurations through a finite element formulation proposed in [8], which enabled the vibration and buckling behavior of functionally graded sandwich beams to be investigated.

Alternative numerical formulations were also proposed. For instance, a finite element model based on the first-order shear deformation theory was formulated in [9] to study the vibration and buckling responses of FG beams, highlighting the importance of shear deformation in structural analysis. An efficient deformation-based finite element approach for bending analysis was subsequently introduced in [10], providing accurate predictions with improved computational efficiency.

In parallel with these developments, several refined beam theories employing special forms of displacement fields have been proposed. A trigonometric shear deformation model introduced by Touratier in [11] provided an efficient representation of transverse shear deformation and became a basis for many subsequent refined theories. In this model, the transverse shear strain distribution through the thickness is described using a sinusoidal function, which allows a more realistic representation of shear effects compared with lower-order theories. An important advantage of this formulation is that the zero transverse shear stress condition on the top and bottom surfaces of the beam is satisfied automatically without requiring a shear correction factor. Later studies incorporated both shear and normal deformation effects in the modeling of FG beams. Such an approach was presented in [12], where a simplified theory accounting for transverse shear and normal strains was proposed.

Higher-order kinematic descriptions were further explored through the development of a fifth-order shear and normal deformation theory for power-law FG beams, which improved the prediction accuracy for bending and buckling responses [13]. Hyperbolic shear deformation functions were later employed for the analysis of FG beams subjected to bending, buckling, and free vibration [14]. A new higher-order shear deformation model suitable for functionally graded sandwich beams was proposed in [15], demonstrating good agreement with existing analytical and numerical solutions. More recently, refined hyperbolic shear deformation formulations have also been extended to the analysis of nonlocal functionally graded nanobeams [16].

Additional studies have focused on the development of Navier type analytical solutions for the static bending and free vibration analysis of functionally graded beams [17], as well as on the formulation of new refined finite element models [18]. In reference [19], Hadji et al. investigated the static and dynamic behavior of functionally graded beams using higher-order shear deformation theories under various boundary conditions. Their formulation accounts for the variation of material properties through the beam thickness and provides improved predictions of deflections, stresses, and natural frequencies compared with classical beam theories. The results demonstrated that higher-order shear deformation models are particularly effective for analyzing moderately thick functionally graded beams.

Despite the substantial body of published research, most existing approaches are primarily oriented either toward numerical implementation or toward specific boundary conditions. In addition, static and dynamic analyses are often formulated within different theoretical frameworks, which prevent the use of a unified mathematical basis and complicate the execution of consistent parametric studies.

In this context, the development of a unified refined analytical formulation is of particular relevance, enabling the investigation of both static bending and free vibration of functionally graded beams with continuously varying properties through the thickness within a single theoretical framework. Such an approach ensures consistency between stiffness and inertial characteristics and makes it possible to evaluate the influence of the material gradient law on deflections and natural frequencies.

In the present study, a refined analytical formulation is developed for the problem of static bending and free vibration of functionally graded beams. The material properties are assumed to vary through the thickness according to a power-law distribution. The governing differential equations are derived, analytical expressions for deflections and natural frequencies are obtained, and a parametric analysis is performed to assess the influence of the material gradient index and the geometric characteristics of the beam on its structural response.

2. Methods

A functionally graded beam of length l with a rectangular cross-section $b \times h$ is considered, where b denotes the width and h the thickness of the beam. The geometry of the structure and the adopted coordinate system are shown in Figure 1. The coordinate axes x_1 and x_3 are oriented along the longitudinal and thickness directions of the beam, respectively. The beam is considered in the domain: $0 \le x_1 \le l;\ -\frac{h}{2} \le x_3 \le \frac{h}{2}$.

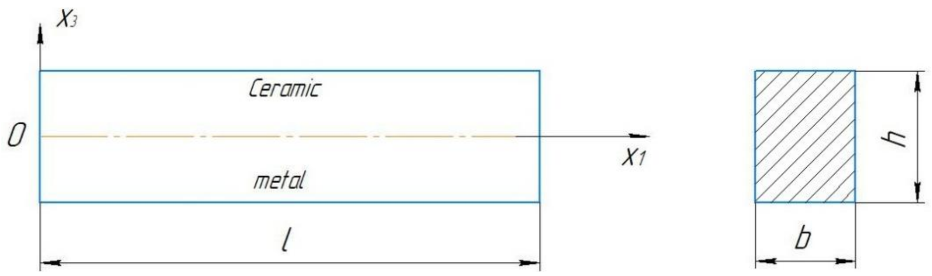

Figure 1 – Computational model of the functionally graded beam and the adopted coordinate system

The cross-section of the beam is assumed to remain constant along its length and to retain a rectangular shape. For the purpose of simplifying the subsequent mathematical derivations, the beam width may be taken as unity (b = 1), which does not reduce the generality of the obtained results.

It is assumed that the mechanical properties of the material vary continuously through the thickness in the x_3 direction according to a power-law distribution, corresponding to the class of power-law functionally graded materials (P-FGM) [20]:

$$\mathrm{E}(x_3) = E_m + (E_c - E_m)\left(\frac{1}{2} + \frac{x_3}{h}\right)^{\mathrm{p}}, \quad \rho(x_3) = \rho_m + (\rho_c - \rho_m)\left(\frac{1}{2} + \frac{x_3}{h}\right)^{\mathrm{p}}, \quad \mathrm{p} \geq 0, \tag{1}$$

where: p – denotes the material gradient index; E_m and E_c – represent the Young's moduli of the metallic and ceramic constituents; ρ_m and ρ_c – correspond to the mass densities of the metallic and ceramic phases, respectively.

The shear modulus is defined as:

$$G(x_3) = \frac{\mathrm{E}(x_3)}{2(1+\nu)} \tag{2}$$

Within the framework of the present refined shear deformation theory, the displacement field is assumed in a general form based on the kinematic assumptions of higher-order beam theories [21]:

$$U_1(x_1, x_3) = \phi(x_3)\theta(x_1), \quad \theta(x_1) = -\frac{dW_0}{dx_1} \tag{3}$$

$$U_3(x_1, x_3) = f(x_3)W(x_1), \quad W(x_1) = W_0(x_1) - \frac{D_{FG}}{A_{FG}}\frac{d^2W_0}{dx_1^2} \tag{4}$$

The thickness-wise distribution functions are expressed as follows [21]:

$$\phi(x_3) = \mathrm{h}\left(\frac{3}{2}\frac{x_3}{\mathrm{h}} - 2\frac{x_3^3}{\mathrm{h}^3}\right), \; f(x_3) = \frac{3}{2} - 6\frac{x_3^2}{\mathrm{h}^2} \tag{5}$$

For the selected functions, the following condition is satisfied, which ensures a physically consistent distribution of transverse shear strains across the thickness.

$$\frac{d\phi(x_3)}{dx_3} = f(x_3) \tag{6}$$

The function *φ(x₃)* describes the distribution of axial displacements through the beam thickness, while the function $f(x_3)$ governs the distribution of transverse shear deformation. In the proposed model these functions are related by Eq. (6), which ensures the kinematic consistency of the formulation. Moreover, the adopted form of $f(x_3)$ automatically satisfies the zero transverse shear stress condition at the top and bottom surfaces of the beam.

The longitudinal strain is defined as follows:

$$\varepsilon_1 = \frac{\partial U_1}{\partial x_1} = \phi(x_3)\frac{d\theta}{dx_1} = -\phi(x_3)\frac{d^2W_0}{dx_1^2} \tag{7}$$

The transverse shear strain, taking into account the adopted assumptions, is expressed as follows [3]:

$$\gamma_{13} = \frac{\partial U_1}{\partial x_3} + \frac{\partial U_3}{\partial x_1} \tag{8}$$

Taking into account relations (3) and (4), we obtain:

$$\gamma_{13} = -f(x_3)\frac{D_{FG}}{A_{FG}}\frac{d^3W_0}{dx_1^3} \tag{9}$$

The stress components are determined according to Hooke's law:

$$\sigma_1 = E(x_3)\varepsilon_1, \quad \tau_{13} = G(x_3)\gamma_{13} \tag{10}$$

Substituting expressions (7) and (9), we obtain:

$$\sigma_1(x_1, x_3) = -E(x_3)\phi(x_3)\frac{d^2W_0}{dx_1^2}, \quad \tau_{13}(x_1, x_3) = -G(x_3)f(x_3)\frac{D_{FG}}{A_{FG}}\frac{d^3W_0}{dx_1^3} \tag{11}$$

The bending moment, taking into account relation Eq. (11), is determined as follows:

$$M = -\frac{d^2W_0}{dx_1^2}\int_{-\frac{h}{2}}^{\frac{h}{2}} E(x_3)\phi(x_3)x_3dx_3$$

The effective bending stiffness of the FG beam is defined as:

$$D_{FG} = \int_{-\frac{h}{2}}^{\frac{h}{2}} E(x_3)\phi(x_3)x_3dx_3 \tag{12}$$

Then:

$$M = -D_{FG}\frac{d^2W_0}{dx_1^2} \tag{13}$$

The transverse shear force, after substituting relation Eq. (11), is expressed as:

$$Q = -\frac{D_{FG}}{A_{FG}}\frac{d^3W_0}{dx_1^3}\int_{-\frac{h}{2}}^{\frac{h}{2}} G(x_3)f(x_3)dx_3$$

The effective shear stiffness is introduced as follows:

$$A_{FG} = \int_{-\frac{h}{2}}^{\frac{h}{2}} G(x_3)f^2(x)dx_3 \quad (14)$$

Then:

$$Q = -D_{FG}\frac{d^3W_0}{dx_1^3} \quad (15)$$

The governing differential equation for the static bending of the functionally graded beam takes the form:

$$D_{FG}\frac{d^4W_0}{dx_1^4} = q(x_1) \quad (16)$$

Free vibrations are governed by the equation:

$$D_{FG}\frac{d^4W_0}{dx_1^4} - m_{FG}\omega^2W_0 = 0 \quad (17)$$

$$m_{FG} = \int_{-\frac{h}{2}}^{\frac{h}{2}} \rho(x_3)dx_3 \quad (18)$$

To verify the validity of the developed formulation and to assess its physical capabilities, a numerical analysis is carried out. The numerical analysis was performed using the derived analytical expressions implemented in Mathcad 15.0 (Parametric Technology Corporation, Needham, MA, USA) [22]. Problems of static bending and free vibration of functionally graded beams are considered, and the obtained results are compared with those predicted by established refined beam theories. Such a comparison makes it possible to confirm the accuracy and stability of the proposed model.

In the present study, the bending and free vibration behavior of FG beams with a rectangular cross-section is investigated. The beam has length l, thickness h, and unit width (b = 1). The geometry and coordinate system are defined such that the longitudinal axis coincides with the x_1 coordinate, while the x_3 axis is directed through the thickness of the beam. The beam is assumed to be simply supported at both ends (S-S boundary conditions).

The beam is composed of a metal-ceramic functionally graded material: Ceramic phase: alumina (E_c = 380 GPa, ν = 0.3), metallic phase: aluminum (E_m = 70 GPa, ν = 0.3), the mass density of the metal is ρ_m = 2700 kg/m^3, and the mass density of the ceramic is ρ_c = 3960 kg/m^3.

For convenience, the following dimensionless forms are introduced:

– Transverse displacement: $\overline{W} = 100\frac{E_m h^3}{q_0 l^4}W\left(\frac{l}{2},0\right)$;

– Axial stress: $\overline{\sigma_1} = \frac{h}{q_0 l}\sigma_1\left(\frac{l}{2},\frac{h}{2}\right)$;

– Transverse shear stress: $\overline{\tau_{13}} = \frac{h}{q_0 l}\,\tau_{13}\,(0,0)$;

– Dimensionless natural frequency: $\overline{\omega} = \frac{\omega l^2}{h}\sqrt{\frac{\rho_m}{E_m}}$.

3. Results and Discussion

Using the developed analytical model, numerical results are obtained for the analysis of bending and free vibration of functionally graded beams. Particular attention is devoted to examining the influence of the material gradient index, beam slenderness ratio, and transverse shear effects on the stress-strain state of FG beams. To evaluate the performance of the proposed formulation, the calculated deflections, stress distributions, and free vibration characteristics are presented in Tables 1-2 and Figures 2-6.

Table 1 – Comparison of dimensionless deflections and stresses of functionally graded beams subjected to uniformly distributed loads for various values of the power-law gradient index

p	Theory	$l/h = 5$			$l/h = 20$		
		$\overline{W}$	$\overline{\sigma_1}$	$\overline{\tau_{13}}$	$\overline{W}$	$\overline{\sigma_1}$	$\overline{\tau_{13}}$
1	Present	6.2586	5.8077	0.7187	5.7292	22.9038	0.7259
	Hadji et al.	6.1805	6.0709	0.7883	5.6965	24.0095	0.7890
	Reddy	6.2594	5.8836	0.7330	5.5685	23.2051	0.7432
	Touratier	6.2586	5.8892	0.7549	5.8049	23.2067	0.7686
	CBT	5.7746	5.7959	-	5.7746	23.1834	-
5	Present	9.6986	8.0059	0.5786	8.7031	31.3997	0.5863
	Hadji et al.	9.6933	8.3581	0.6523	8.6182	32.8183	0.6540
	Reddy	9.8281	8.1104	0.5904	8.8182	31.8127	0.6013
	Touratier	9.8367	8.1222	0.6155	8.8188	31.8159	0.6292
	CBT	8.7508	7.9428	-	8.7508	31.7711	-

Table 2 – Dimensionless numerical results for the free vibration of a simply supported (S-S) FG beam: comparison of the present model with Timoshenko and Reddy-type theories

p	Theory	$l/h = 5$	$l/h = 20$
		$\overline{\omega}$	$\overline{\omega}$
1	Present (HOBT)	3.9710	4.2038
	Present (FOBT)	3.9710	4.2038
	Timoshenko	3.9902	4.2050
	Reddy	3.9904	4.2050
5	Present (HOBT)	3.3740	3.6460
	Present (FOBT)	3.4025	3.6490
	Timoshenko	3.4312	3.6508
	Reddy	3.4012	3.6484

In the present study, the functionally graded beam is assumed to be composed of a metal and a ceramic phase. Following commonly used FG material models in the literature, aluminum is considered as the metal phase and alumina (Al_2O_3) as the ceramic phase, and Poisson's ratio is assumed to be constant through the thickness with $\nu = 0.3$.

For the purpose of comparison with existing beam theories, the deflection, normal stress, transverse shear stress, and natural frequency are presented in dimensionless form. Therefore, the normalized quantities $\overline{W}$, $\overline{\sigma_1}$, $\overline{\tau_{13}}$ and $\overline{\omega}$ are used to eliminate the influence of geometric parameters and loading conditions and to ensure a consistent comparison between different theories.

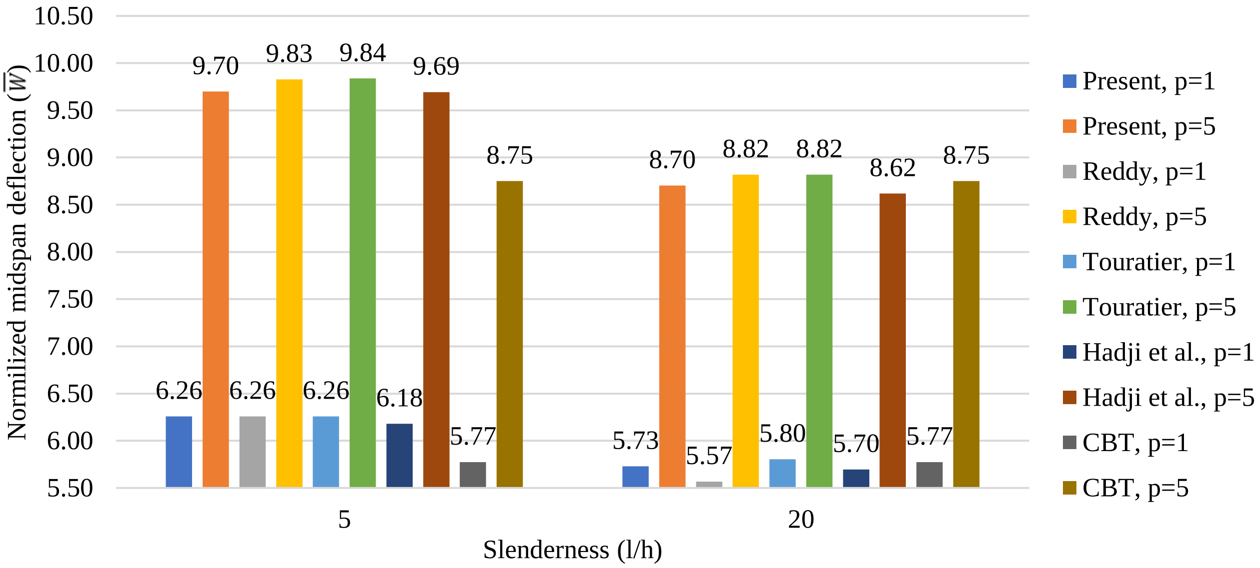

Figure 2 – Comparison of the normalized mid-span deflection obtained by different beam theories

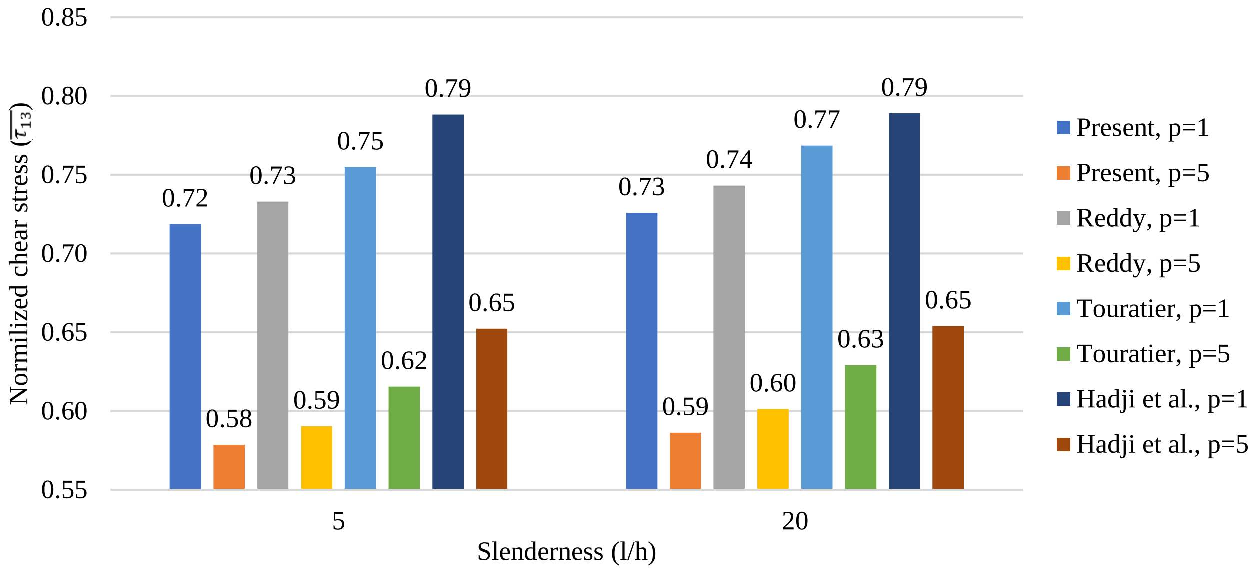

Figure 3 – Comparison of the convergence of transverse shear stresses obtained using refined theories for functionally graded beams

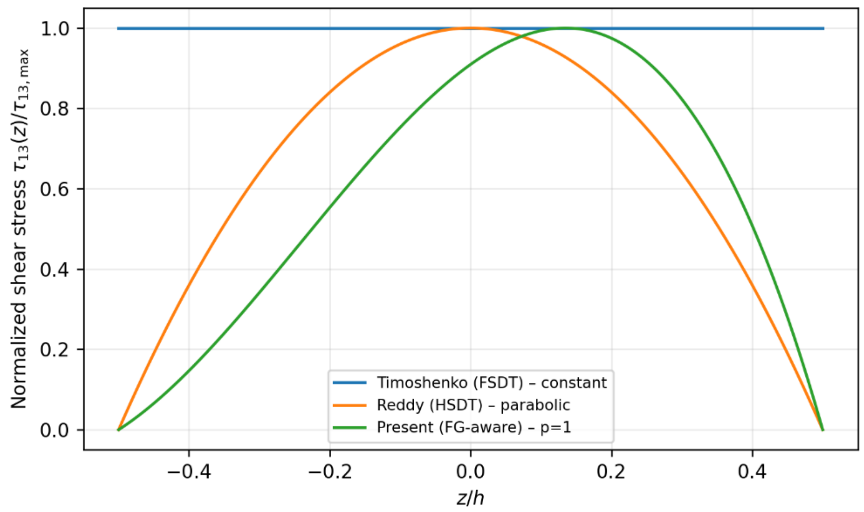

Figure 4 – Through-thickness distribution of transverse shear stresses (p = 1)

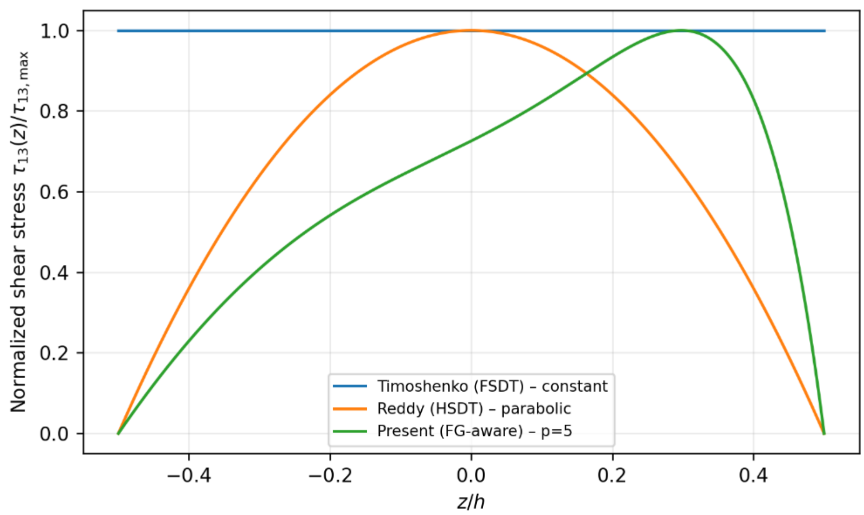

Figure 5 – Through-thickness distribution of transverse shear stresses (p = 5)

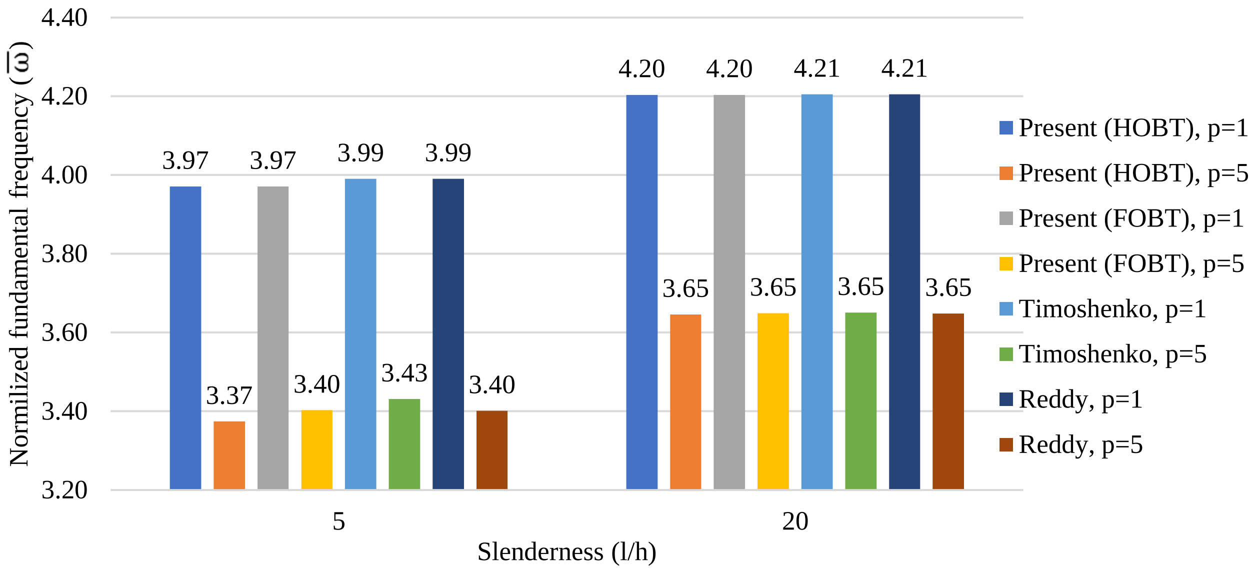

Figure 6 – Free vibration (S-S) comparison of the fundamental frequency: HOBT – Higher order beam theory; FOBT – First order beam theory.

The numerical results presented in Tables 1-2 and Figures 2-6 demonstrate that the proposed formulation provides stable predictions for both the static and dynamic behavior of functionally graded beams. The obtained results show good agreement with well-established refined beam theories reported in the literature, including the models of Timoshenko [3], Reddy [4], and Touratier [11]. This agreement confirms that the adopted kinematic assumptions and the derived governing equations are physically reasonable and mathematically consistent.

The parameter p used in Figures 2-6 represents the material gradation index, which describes the variation of material properties through the thickness of the functionally graded beam according to a power-law distribution. In particular, the parameter p controls the relative volume fractions of the metal and ceramic phases in the material. When $p = 0$, the material corresponds to a fully ceramic beam, whereas increasing values of p lead to a gradual increase in the metallic phase. The value $p = 1$ corresponds to an approximately linear variation of material properties, while $p = 5$ represents a more pronounced material gradation.

The bending analysis indicates that the main parameters of the stress-strain state, such as transverse deflection, normal stresses, and transverse shear stresses, are strongly affected by the beam slenderness ratio l/h. According to the values presented in Table 1, the discrepancies between the considered beam theories are more noticeable for relatively thick beams with $l/h = 5$. This behavior can be explained by the significant influence of transverse shear deformation in moderately thick structures. Similar conclusions were reported in earlier studies on functionally graded beams, where refined shear deformation theories were shown to provide more accurate predictions for thick beams [2], [4].

Figures 2 and 3 illustrate the influence of the slenderness ratio on the bending response of the beam. As the ratio l/h increases, the predictions of different beam theories gradually converge. This tendency corresponds to the classical asymptotic transition toward the Euler-Bernoulli beam theory, which becomes accurate for slender beams where transverse shear effects are negligible. A similar convergence behavior has also been reported in previous analytical studies of FG beams [2].

The distribution of transverse shear stresses through the beam thickness is presented in Figures 4-5. In contrast to classical beam models, where the shear stress profile depends only on geometric shape functions, the proposed formulation explicitly accounts for the variation of the material properties through the thickness. As a result, the transverse shear stress τ_{13} becomes dependent on the material gradation. When the gradient index p increases, the stress distribution becomes asymmetric and the location of the maximum stress shifts toward the stiffer region of the cross-section. Similar asymmetric stress distributions were reported in elasticity-based solutions for functionally graded beams [6].

The results of the free vibration analysis presented in Table 2 and Figure 6 confirm the correctness of the dynamic formulation. The obtained dimensionless natural frequencies show good agreement with those predicted by refined beam theories, including the Timoshenko model [3] and higher-order theories such as the formulation proposed by Reddy [4]. The differences between the models are more noticeable for thick beams, while for slender beams (l/h = 20), the results practically coincide. This behavior indicates that the proposed model correctly reproduces the transition to the classical thin-beam solution.

The influence of the material gradient index p is clearly observed in both static and dynamic responses of the beam. An increase in the value of p leads to a reduction in the effective bending stiffness and modifies the mass distribution through the thickness. Consequently, larger deflections and lower natural frequencies are obtained. This trend is consistent with the physical characteristics of functionally graded materials and agrees with the conclusions of previous investigations of FG beam behavior [2], [19].

Overall, the comparison of tabulated data and graphical results demonstrates that the proposed theory provides an energetically consistent description of the behavior of functionally graded beams. The model adequately accounts for transverse shear deformation effects, thickness-wise variation of mechanical properties, and geometric parameters without resorting to empirical correction factors. As a result, it achieves a balance between the computational efficiency of one-dimensional beam models and a level of physical fidelity approaching that of three-dimensional elasticity solutions, making the proposed approach a promising tool for the engineering analysis of advanced functionally graded structures.

From a practical engineering perspective, the obtained results can be useful for the analysis and design of structural elements made of functionally graded materials in civil engineering applications. Functionally graded beams may be used in modern building structures, bridge elements, layered structural members, and advanced composite components where gradual variation of material properties improves structural performance. The presented analytical formulation allows engineers to estimate deflections, stresses, and natural frequencies of such elements with sufficient accuracy. This information is important for evaluating structural stiffness, strength, and vibration resistance of load-bearing components in building structures.

4. Conclusions

In the present study, a refined analytical formulation has been developed for the bending and free vibration analysis of functionally graded beams, taking into account transverse shear deformation effects. The material properties are assumed to vary continuously through the beam thickness according to a power-law distribution, allowing a realistic representation of the inhomogeneous structure of FG materials.

The main findings of the study can be summarized as follows:

1. A unified analytical formulation has been established that allows the description of both static bending and free vibration of functionally graded beams within a consistent mechanical framework.

2. The obtained numerical results demonstrate good agreement with well-known refined beam theories, including the models of Timoshenko, Reddy, etc., confirming the accuracy and reliability of the proposed formulation.

3. The results show correct asymptotic convergence with increasing beam slenderness ratio l/h, indicating the mathematical consistency of the model and its compatibility with the classical thin-beam theory.

4. The developed formulation provides an explicit analytical representation of the transverse shear stresses $\tau_{13}(x_3)$, which depend on the thickness-wise variation of the shear modulus $G(x_3)$.

This feature allows the model to capture asymmetric stress distributions typical for functionally graded materials.

5. The influence of the material gradient index p on both static and dynamic responses has been demonstrated. Increasing the value of p leads to a redistribution of stiffness and mass along the beam thickness, which results in larger deflections and lower natural frequencies.

6. The dynamic behavior of the FG beam is governed by the relationship $\omega_n \sim \sqrt{\frac{D_{FG}}{m_{FG}}}$, emphasizing the importance of simultaneously accounting for the spatial variation of both stiffness and inertial properties.

Overall, the proposed formulation represents an efficient analytical tool for the study of functionally graded beams. Due to its relatively simple analytical structure and physically consistent predictions, the model can be applied to the analysis and design of advanced structural elements made of functionally graded and composite materials. The formulation can also be extended to problems involving elastic foundations, stability analysis, and structural dynamics of more complex engineering systems.

Acknowledgments

This research was funded by the Science Committee of the Ministry of Science and Higher Education of the Republic of Kazakhstan (AP22684709 – An improved method for calculating bending and free vibration of functionally graded beams resting on an elastic foundation).

References

[1] V. Birman and L. W. Byrd, “Modeling and Analysis of Functionally Graded Materials and Structures,” *Applied Mechanics Reviews*, vol. 60, no. 5, pp. 195–216, Sep. 2007, doi: 10.1115/1.2777164.

[2] H.-T. Thai and T. P. Vo, “Bending and free vibration of functionally graded beams using various higher-order shear deformation beam theories,” *International Journal of Mechanical Sciences*, vol. 62, no. 1, pp. 57–66, Sep. 2012, doi: 10.1016/j.ijmecsci.2012.05.014.

[3] S. P. Timoshenko, “On the correction for shear of the differential equation for transverse vibrations of prismatic bars,” *The London, Edinburgh, and Dublin Philosophical Magazine and Journal of Science*, vol. 41, no. 245, pp. 744–746, May 1921, doi: 10.1080/14786442108636264.

[4] J. N. Reddy, “A Simple Higher-Order Theory for Laminated Composite Plates,” *Journal of Applied Mechanics*, vol. 51, no. 4, pp. 745–752, Dec. 1984, doi: 10.1115/1.3167719.

[5] M. Aydogdu and V. Taskin, “Free vibration analysis of functionally graded beams with simply supported edges,” *Materials & Design*, vol. 28, no. 5, pp. 1651–1656, Jan. 2007, doi: 10.1016/j.matdes.2006.02.007.

[6] B. V. Sankar, “An elasticity solution for functionally graded beams,” *Composites Science and Technology*, vol. 61, no. 5, pp. 689–696, Apr. 2001, doi: 10.1016/S0266-3538(01)00007-0.

[7] T. P. Vo, H.-T. Thai, T.-K. Nguyen, and F. Inam, “Static and vibration analysis of functionally graded beams using refined shear deformation theory,” *Meccanica*, vol. 49, no. 1, pp. 155–168, Jan. 2014, doi: 10.1007/s11012-013-9780-1.

[8] T. P. Vo, H.-T. Thai, T.-K. Nguyen, A. Maheri, and J. Lee, “Finite element model for vibration and buckling of functionally graded sandwich beams based on a refined shear deformation theory,” *Engineering Structures*, vol. 64, pp. 12–22, Apr. 2014, doi: 10.1016/j.engstruct.2014.01.029.

[9] V. Kahya and M. Turan, “Finite element model for vibration and buckling of functionally graded beams based on the first-order shear deformation theory,” *Composites Part B: Engineering*, vol. 109, pp. 108–115, Jan. 2017, doi: 10.1016/j.compositesb.2016.10.039.

[10] H. Ziou, M. Himeur, H. Guenfoud, and M. Guenfoud, “An Efficient Finite Element Formulation Based on Deformation Approach for Bending of Functionally Graded Beams,” *JSM*, vol. 12, no. 2, 2020, doi: 10.22034/jsm.2019.1867884.1437.

[11] M. Touratier, “An efficient standard plate theory,” *International Journal of Engineering Science*, vol. 29, no. 8, pp. 901–916, Jan. 1991, doi: 10.1016/0020-7225(91)90165-Y.

[12] M. Bourada, K. Abdelhakim, M. S. A. Houari, and A. Tounsi, “A new simple shear and normal deformations theory for functionally graded beams,” *Steel and Composite Structures*, vol. 18, pp. 409–423, Feb. 2015, doi: 10.12989/scs.2015.18.2.409.

[13] S. M. Ghumare and A. S. Sayyad, “A New Fifth-Order Shear and Normal Deformation Theory for Static Bending and Elastic Buckling of P-FGM Beams,” *Lat. Am. j. solids struct.*, vol. 14, no. 11, pp. 1893–1911, 2017, doi: 10.1590/1679-78253972.

[14] A. Sayyad and Y. Ghugal, "Bending, buckling and free vibration responses of hyperbolic shear deformable FGM beams," *MACS*, vol. 5, no. 1, Apr. 2018, doi: 10.22075/macs.2018.12214.1117.
[15] T.-K. Nguyen, T. Truong-Phong Nguyen, T. P. Vo, and H.-T. Thai, "Vibration and buckling analysis of functionally graded sandwich beams by a new higher-order shear deformation theory," *Composites Part B: Engineering*, vol. 76, pp. 273–285, Jul. 2015, doi: 10.1016/j.compositesb.2015.02.032.
[16] D. Indronil and I. M. Nazmul, "A novel hyperbolic shear deformation beam theory for functionally graded nonlocal nanobeams," *Discov Appl Sci*, vol. 7, no. 10, p. 1204, Oct. 2025, doi: 10.1007/s42452-025-07047-5.
[17] Y. L. Pei and L. X. Li, "Comment on the Navier's solution in 'A sinusoidal beam theory for functionally graded sandwich curved beams' (Composite Structures 226 (2019) 111246)," *Composite Structures*, vol. 243, p. 112248, Jul. 2020, doi: 10.1016/j.compstruct.2020.112248.
[18] F. Rahmani, R. Kamgar, and R. Rahgozar, "Finite Element Analysis of Functionally Graded Beams using Different Beam Theories," *Civ Eng J*, vol. 6, no. 11, pp. 2086–2102, Nov. 2020, doi: 10.28991/cej-2020-03091604.
[19] L. Hadji, N. Zouatnia, and F. Bernard, "An analytical solution for bending and free vibration responses of functionally graded beams with porosities: Effect of the micromechanical models," *Structural Engineering & Mechanics*, vol. 69, no. 2, pp. 231–241, Feb. 2019, doi: 10.12989/sem.2019.69.2.231.
[20] A. S. Sayyad and Y. M. Ghugal, "Analytical solutions for bending, buckling, and vibration analyses of exponential functionally graded higher order beams," *Asian J Civ Eng*, vol. 19, no. 5, pp. 607–623, Jul. 2018, doi: 10.1007/s42107-018-0046-z.
[21] K. A. Tursynov, "Arqalyqty esepteu teoriyalary," in *Textbook*, Karaganda: Karaganda Buketov University, 2007.
[22] B. Maxfield, "Essential PTC® Mathcad Prime® 3.0: a guide for new and current users," Oxford: Academic Press, 2014, p. 563.

Information about authors:
Sungat Akhazhanov – PhD, Associate Professor, Research Laboratory Applied Mechanics and Robotics, Buketov Karaganda National Research University, Karaganda, Kazakhstan, *stjg@mail.ru*
Aizhan Nurgoziyeva – PhD, Research Laboratory Applied Mechanics and Robotics, Buketov Karaganda National Research University, Karaganda, Kazakhstan, *aizhanzhanabai@gmail.com*
Kiyas Kutimov – PhD, Research Laboratory Applied Mechanics and Robotics, Buketov Karaganda National Research University, Karaganda, Kazakhstan, *kiyas6@mail.ru*

Author Contributions:
Sungat Akhazhanov – methodology, analysis, drafting.
Aizhan Nurgoziyeva – resources, modeling, editing, funding acquisition.
Kiyas Kutimov – data collection, visualization.

Conflict of Interest: The authors declare no conflict of interest.

Use of Artificial Intelligence (AI): The authors declare that AI was not used.

Received: 07.12.2025
Revised: 16.03.2026
Accepted: 19.03.2026
Published: 21.03.2026

Technobius, 2026, 6(1), 0097, DOI: https://doi.org/10.54355/tbus/6.1.2026.0097

Technobius
https://technobius.kz/
e-ISSN
2789-7338

Review

A review of the current state of 3D subsurface cartography for geotechnical ground characterization

Nurgul Alibekova[1,2], Aleksej Aniskin[3], Kairat Mukhambetkaliev[4], Indira Makasheva[1,2,*]

[1]Solid Research Group, LLP, Astana, Kazakhstan
[2]Department of Civil Engineering, L.N. Gumilyov Eurasian National University, Astana, Kazakhstan
[3]Department of Civil Engineering, University North, Varaždin, Croatia
[4]JSC "Kazakhstan Road Research Institute", Astana, Kazakhstan
*Correspondence: indira.yergaliyeva@gmail.com

Abstract. Three-dimensional subsurface mapping is increasingly used to turn ground investigation evidence into continuous 3D models of soil layers and geotechnical properties that support decisions in ground characterization. This review summarizes the current state of 3D mapping for geotechnical purposes using a citation-guided selection based on Litmaps, resulting in a curated set of 27 studies. The literature is organized into a taxonomy aligned with the Litmaps clustering and grouped into six approach families: implicit or potential-field structural modeling, voxel models and voxel workflows, uncertainty-oriented stochastic and inversion or segmentation approaches, automation and urban-scale pipelines, geophysics-driven 3D modeling, and interoperability and engineering delivery. The comparative analysis shows that practical outcomes depend not only on the final model type but also on workflow design, including data harmonization, modeling rules, and update procedures. Credibility depends on validation methods matched to the target variable and on uncertainty outputs that show where the model is strongly supported by data and where it relies on extrapolation. The review also highlights model comparability as a key operational issue, since mismatches between neighboring models can arise from inconsistent conceptual rules, discretization differences, uneven data density, and asymmetric auxiliary constraints. The paper concludes with an applicability framework, including a decision flow and compact criteria, to guide selection, evaluation, and reporting of decision-grade 3D subsurface mapping products for geotechnical ground characterization.

Keywords: 3D subsurface mapping, geotechnical ground characterization, voxel models, implicit structural modeling, uncertainty and validation.

1. Introduction

Urban development increasingly depends on reliable knowledge of the shallow subsurface, yet the ground remains one of the least directly observable components of the built environment. Standard site-investigation outputs, borehole logs, laboratory tests, and a limited number of interpretive cross-sections are indispensable, but they are not, by themselves, designed to represent spatial continuity and variability in 3D, nor to communicate uncertainty as an explicit "map product". Geotechnical properties are well known to exhibit substantial natural variability; random-field perspectives emphasize that this variability can be concisely characterized by parameters such as the coefficient of variation and correlation structure (scale of fluctuation), which implies that sparse point sampling may miss meaningful lateral changes [1]. The need for improved subsurface characterization is amplified in urban settings where subsurface conditions evolve under interacting natural and anthropogenic drivers. For instance, leakage from underground water and drainage pipelines is widely recognized as a contributor to soil erosion, voiding, sinkhole formation, and ground collapse risk, motivating stronger monitoring and mapping practices for near-surface strata [2]. In parallel, the broader geotechnical literature has increasingly framed modeling as only one part of decision-making, emphasizing that the principal obstacle to effective application is often the lack of explicit, transparent accounting for uncertainty (covering soil properties, stratification, and model performance) rather than the absence of computational tools [3]. Against this background, 3D subsurface cartography for geotechnical purposes can be defined as the set of methods that transform heterogeneous subsurface observations (e.g., boreholes and complementary information) into spatially continuous, easy to explore, and visualizable 3D representations of soil stratigraphy, together with uncertainty where possible. In this sense, "cartography" is not merely a 3D visualization; it is a structured representation that supports repeatable cartographic operations: slicing cross-sections, extracting virtual boreholes, generating volumes and surfaces, and communicating confidence in a form that is interpretable by multiple stakeholders. Early developments in attributed 3D geological modeling explicitly highlighted the value of 3D models of the shallow subsurface as an organizing framework for disparate data and interpretations, bridging conceptual models and decision-support needs [4]. However, the move from 2D documentation to 3D cartographic products introduces distinct methodological and practical challenges. Subsurface datasets are typically sparse, clustered, and inconsistent in classification and quality; resulting 3D models are sensitive to interpretive assumptions and parameter choices. More fundamentally, geological and geotechnical models contain both aleatory components (natural variability) and epistemic components (limited knowledge and interpretation uncertainty). Evidence-based treatments of geological model confidence and uncertainty emphasize that credibility depends on making these uncertainties visible and traceable, rather than embedding them implicitly in a single deterministic model [5]. This becomes especially important when 3D subsurface maps must be compared or integrated across neighboring sites (e.g., urban blocks or infrastructure corridors), where inconsistent conceptual assumptions and boundary conditions can lead to discontinuities and mismatches that undermine trust in the mapped products. Over the last two decades, 3D subsurface modeling has expanded from specialist geological modeling toward broader urban and engineering applications. Studies coupling 3D geological models to urban underground-space evaluation illustrate how 3D representations can directly influence planning-oriented assessments, while also implicitly stressing the dependence of such applications on the quality and credibility of the underlying models [6]. Yet, despite rapid progress, the relevant literature remains distributed across engineering geology, geophysics, GIS, and computational modeling communities. As a result, readers seeking to use 3D subsurface maps for geotechnical characterization face practical questions that are not consistently answered: what constitutes a "decision-grade" 3D subsurface cartographic product, which approach families are best suited for which data regimes and scales, how uncertainty should be evaluated and communicated, and how interoperability and updateability should be treated when models become living datasets rather than static figures.

This review is therefore necessary to consolidate the current state of 3D subsurface cartography for geotechnical purposes and to synthesize how modeling choices translate into the credibility, usability, and applicability of subsurface information. The objectives of this review are to: (1) develop a taxonomy of major approach families used for 3D subsurface mapping in geotechnical contexts; clearly compare their representations and inference strategies; (2) synthesize how different approaches transform available observations into 3D stratigraphic and/or property models; (3) critically analyze validation practices and uncertainty treatment, emphasizing how credibility is established and communicated; (4) examine comparability and integration challenges, including the practical issue of mismatches between neighboring 3D models along shared boundaries; and (5) translate the evidence into practical guidance (an applicability matrix and reporting checklist) to support rigorous selection, evaluation, and communication of 3D subsurface cartographic products for geotechnical subsurface characterization.

2. Methods

This review was designed as a targeted synthesis of the current state of 3D subsurface cartography for geotechnical purposes, with emphasis on subsurface information products and their applicability for ground characterization. The methodological workflow follows a transparent evidence synthesis logic for identifying, screening, and including sources, consistent with established reporting guidance for systematic reviews [7].

The literature set was constructed using Litmaps as a citation-guided discovery environment, where relationships among candidate papers were explored through forward and backward citation links while simultaneously viewing publication recency and citation prominence in the network (Figure 1). This supported both coverage of influential foundational contributions and identification of more recent clusters that represent active research directions.

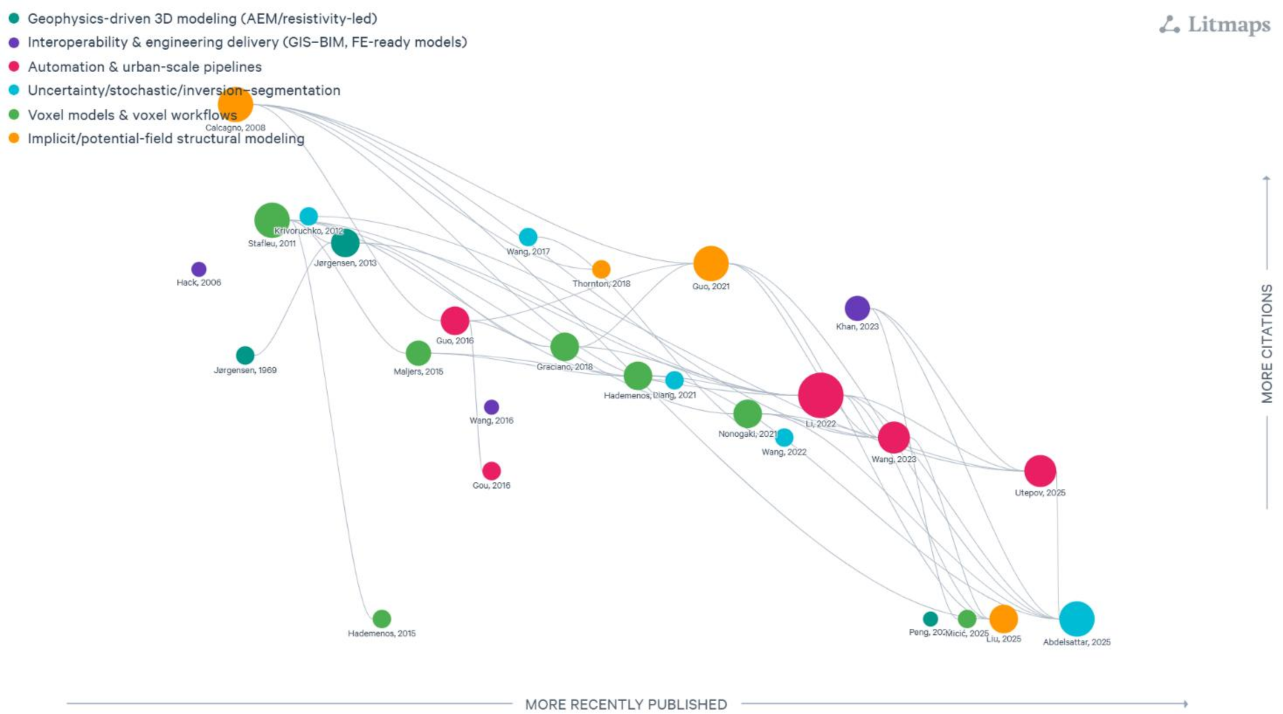

Figure 1 – Litmaps citation network of the 27 selected papers, showing citation links and the axes of publication recency and citation count

Starting from seed papers relevant to 3D subsurface mapping, the Litmaps network was iteratively expanded by adding candidate studies connected through citation links. The expansion was continued until additional inclusions became repetitive or outside the defined scope. A two-stage screening process was applied. First, titles and abstracts were screened to remove studies clearly unrelated to 3D subsurface cartography for geotechnical characterization. Second, full texts were screened to confirm that each retained study contributed directly to at least one of the following dimensions, namely representation of the subsurface in 3D, inference engines used to estimate layers and or properties, uncertainty and validation practice, data fusion, automation and scalability, or interoperability and delivery of models for downstream use.

To enable consistent cross-paper comparison across engineering geology, geophysics, GIS, and computational modeling communities, each included paper was coded using a structured extraction form. The extracted information captured the conditioning data used for model building, including boreholes and logs, laboratory or in situ measurements, geological maps and cross-sections, geophysical constraints, and prior conceptual rules, together with the target variables represented in the model, such as stratigraphic interfaces, lithological classes, and continuous property fields. The coding also recorded the 3D representation type, the inference engine used for estimation or classification, how discontinuities such as faults or unconformities were handled when relevant, the validation strategy and reported metrics, the presence and form of uncertainty quantification and communication, and the final deliverables including file formats, GIS or web visualization, database structures, and pathways for BIM or FE oriented use. In addition, explicit limitations and future work statements were extracted verbatim and later grouped into recurring themes to support a gap analysis grounded in author reported evidence.

To align the review structure with the Litmaps tool [8] visualization (Figure 1), each paper was assigned one primary tag corresponding to one of six approach families, namely geophysics driven 3D modeling that is AEM or resistivity led (teal green legend), interoperability and engineering delivery including GIS BIM and FE ready models (purple legend), automation and urban scale pipelines (red legend), uncertainty oriented approaches including stochastic modeling and inversion or segmentation (blue legend), voxel models and voxel workflows (green legend), and implicit or potential field structural modeling (orange legend). The one paper, one primary tag rule was used to preserve the readability of the Litmaps figure, while cross-cutting characteristics were captured through the extracted coding fields and are discussed comparatively in the synthesis.

The synthesis proceeds by first constructing a taxonomy that compares representations and inference engines across the six approach families, then analyzing workflow level differences in data regimes, automation level, scalability, and delivery, and finally evaluating credibility through validation and uncertainty practice with specific attention to comparability across neighboring models and boundary mismatch issues. Recurring limitations and future work themes across the 27 papers are then consolidated into an applicability matrix and a reporting checklist intended to support transparent selection, evaluation, and communication of 3D subsurface cartographic products for geotechnical subsurface characterization.

3. Taxonomy of 3D subsurface cartography approaches

The current section establishes the taxonomy used in this review and links it directly to the six approach families defined in the Litmaps-based tagging scheme presented in Figure 1. The purpose of the taxonomy is not only to classify methods by their technical implementation, but also to compare them in terms of the type of subsurface information they produce and the extent to which those products are suitable for geotechnical ground characterization. Across the 27 reviewed papers, the strongest distinctions are observed in the way the subsurface is represented in 3D, the inference engine used to estimate geometry and or properties, and the intended delivery format for downstream use. These distinctions are evident across the implicit structural modeling line (for example [9], [10], [11], [12]), the voxel-model line (for example [13], [14], [15], [16], [17], [18], [19]), uncertainty and stochastic approaches (for example [20], [21], [22], [23], [24]), automation and urban-scale pipelines (for example [25], [26], [27], [28], [29]), geophysics-driven modeling (for example [30], [31], [32]), and interoperability or engineering-delivery focused studies (for example [33], [34], [35]).

To make the comparison explicit and reusable in the later sections, the taxonomy is summarized in Table 1, which organizes the reviewed literature by approach family, dominant representation, common inference logic, typical outputs, and principal geotechnical relevance.

Table 1 – Taxonomy of cartography approaches and their geotechnical information products

No.	Approach family	Typical representation	Dominant inference / modeling logic	Typical input data regime	Typical output products	Main geotechnical relevance
1	Implicit or potential-field structural modeling [9], [10], [11], [12]	Continuous scalar or vector fields, implicit surfaces, structural surfaces	Structural interpolation constrained by interfaces, orientations, stratigraphic rules, and topological relations	Borehole contacts, interpreted interfaces, orientations, geological rules, sometimes auxiliary sections	Stratigraphic surfaces, solids, structural frameworks, exportable meshes	Strong for coherent layer geometry and structural continuity; useful when stratigraphic architecture is the primary target
2	Voxel models and voxel workflows [13], [14], [15], [16], [17], [18], [19]	Regular 3D grids (voxels), categorical and or continuous volumetric fields	Interpolation, classification, rule-based assignment, gridding, voxel population and refinement	Boreholes and logs, property values, lithology classes, open borehole databases, optional geophysical constraints	Lithology volumes, property volumes, 3D queries, cross-sections, statistics, web-ready blocks	Strong for volumetric querying, spatial statistics, and practical GIS workflows; useful for multi-attribute subsurface mapping
3	Uncertainty, stochastic, inversion and segmentation approaches [20], [21], [22], [23], [24]	Multiple realizations, probabilistic class fields, uncertainty volumes, stochastic structures	Geostatistical estimation, stochastic simulation, Bayesian or likelihood-based inference,	Boreholes, geophysics, priors, training labels, model constraints, synthetic benchmarks	Uncertainty maps or volumes, probability of class or interface, ensembles,	Essential for credibility assessment, risk-aware interpretation, and transparent

			inversion and segmentation frameworks		confidence indicators	communication of model confidence
4	Automation and urban-scale pipelines [25], [26], [27], [28], [29]	Mixed representations, often workflow-centric and conversion-based	Automated processing chains, database-driven model generation, rule-guided reconstruction, GIS geoprocessing	Large borehole archives, heterogeneous logs, urban datasets, standardized inputs, workflow scripts	Scalable 3D urban subsurface models, repeatable pipelines, batch products, updateable datasets	Important for operational deployment at city or corridor scale and for repeatable mapping under practical constraints
5	Interoperability and engineering delivery (GIS-BIM, FE-ready) [33], [34], [35]	Exchange-ready 3D ground models, converted analytical grids and meshes, integrated information structures	Model translation, schema alignment, geometric conversion, data exchange and delivery workflows	Existing geological or geotechnical models plus target platform requirements (GIS, BIM, FE)	FE-ready models, GIS/BIM integrated datasets, transferable ground information objects	Critical for practical use of subsurface models in engineering workflows and digital project environments
6	Geophysics-driven 3D modeling (AEM or resistivity led) [30], [31], [32]	Voxel or layered geophysical-geological models, interpreted geophysical volumes	Geophysical inversion interpretation, cognitive geological interpretation, integration of geophysics with boreholes and prior geology	AEM, resistivity, geophysical sections or volumes, calibration boreholes, geological interpretation	Large-area 3D geological models with stronger areal coverage than borehole-only workflows	Particularly valuable for extending spatial coverage and constraining regional to corridor-scale subsurface structure

To complement the taxonomy, Figure 2 presents representative examples of 3D subsurface products associated with the approach families. This gallery is not to compare visual quality across studies, but to illustrate the different forms of outputs that are ultimately delivered to users, including structural surfaces, voxel products, uncertainty representations, and engineering-oriented models.

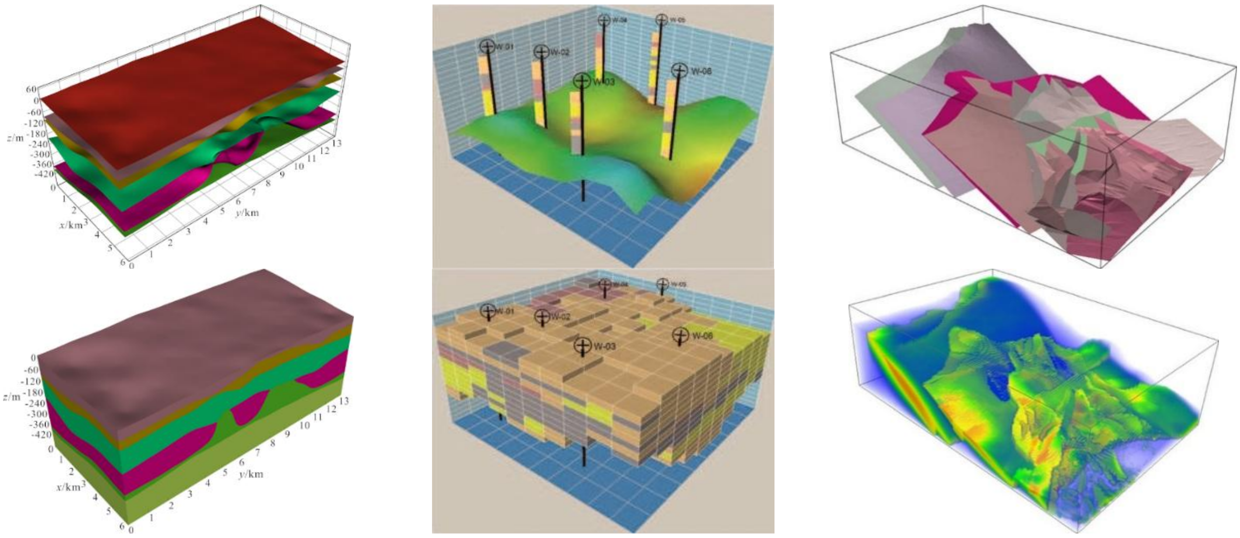

a) Approach family No. 1 [12] b) Approach family No. 2 [13] c) Approach family No. 3 [22]

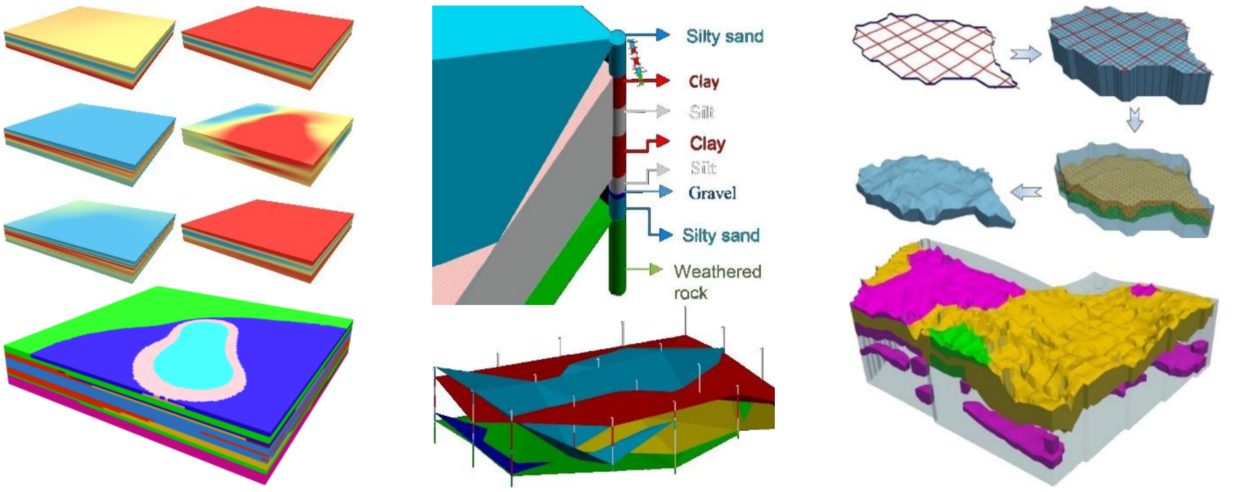

d) Approach family No. 4 [29] e) Approach family No. 5 [35] f) Approach family No. 6 [32]

Figure 2 – Representative gallery of typical 3D subsurface products across the approach families

The taxonomy in Table 1, together with the representative output gallery in Figure 2, shows that the reviewed studies are not separated by a single methodological boundary. Instead, they differ across three intersecting dimensions. The first dimension is the representation of the subsurface, which ranges from surface-based structural frameworks to full volumetric discretization. The second dimension is the inference strategy, which ranges from deterministic and rule-based interpolation to explicitly probabilistic and stochastic formulations. The third dimension is the intended destination of the model, which ranges from scientific interpretation and visualization to engineering delivery through GIS, BIM, or finite-element compatible formats. This is why some papers sit close together in the Litmaps network while still serving different roles in practice, for example [27] and [28] in automation-oriented workflows, or [34] and [35] in interoperability and engineering delivery.

A key implication of this taxonomy is that no single approach family is universally optimal for geotechnical subsurface characterization.

Implicit structural models are often advantageous when the principal task is reconstruction of stratigraphic architecture with strong structural coherence ([9], [10], [11], [12]), whereas voxel workflows are often more suitable when the objective includes volumetric statistics, grid-based spatial querying, and property field analysis across many attributes ([13], [17], [18], [19]).

Uncertainty-oriented approaches are indispensable when confidence reporting and risk-aware interpretation are central ([20], [22], [23], [24]), but they may require higher methodological overhead and clearer communication protocols for practical adoption.

Geophysics-driven models can substantially improve areal continuity in settings where boreholes are sparse ([30], [31], [32]), while interoperability-focused studies highlight that even technically strong 3D models can remain underused unless they are deliverable in formats and schemas compatible with engineering workflows ([33], [34], [35]).

The taxonomy also clarifies the role of automation as a separate family rather than merely a feature of other methods. In the reviewed corpus, automation and urban-scale pipeline studies emphasize repeatability, throughput, and updateability under real-world data heterogeneity ([25], [26], [27], [28], [29]). This makes them especially relevant for municipal databases, corridor projects, and iterative mapping contexts where new boreholes or revised logs are added over time. At the same time, automation does not eliminate the need for human geological judgement. Instead, it shifts expert intervention toward rule definition, quality control, and interpretation of ambiguous or conflicting evidence. The taxonomy developed in this section serves as the analytical backbone for the next three sections.

4. From data to model: workflows, automation, and scalability

This section examines how the reviewed studies move from heterogeneous subsurface observations to usable 3D cartographic products, with emphasis on workflow logic, automation, and scalability.

The reviewed corpus shows that the practical difference between methods is often not only the final representation, but also the sequence of transformations applied to the data before modeling begins. In the workflow-oriented literature, this sequence is treated as a first-class methodological component rather than a hidden preprocessing step [25]. In urban-scale studies, the workflow itself becomes the main contribution because repeatability and updateability are necessary when large borehole archives are involved [28]. In GIS-centered implementations, the workflow is explicitly operationalized as a geoprocessing chain so that model generation can be rerun after parameter or data updates [29].

Before presenting the detailed comparison, the general workflow pattern identified across the reviewed studies is summarized in Figure 3 below. This workflow is a synthesis produced in this review and is intended to provide a common reference for comparing otherwise different modeling traditions.

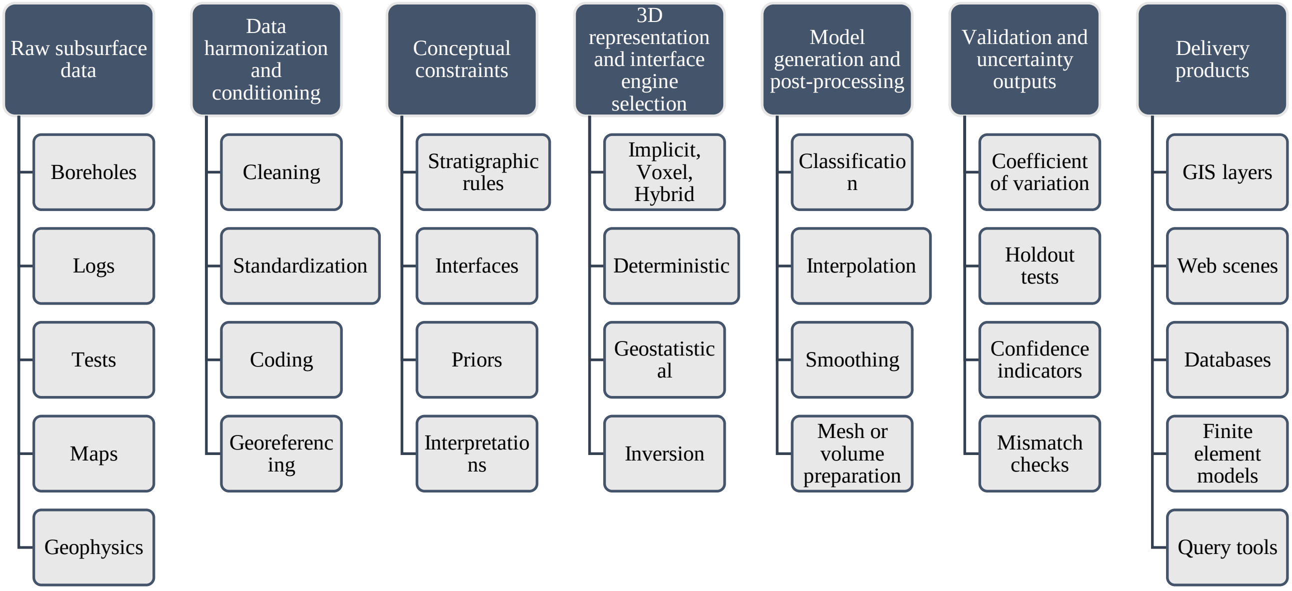

Figure 2 – Generalized data-to-model workflow for 3D subsurface cartography

A recurring workflow requirement is the transformation of heterogeneous records into a consistent internal representation before any interpolation or reconstruction is performed. In migration-oriented modeling work, conversion from legacy 2D geological materials into a structured 3D workflow is presented as a central technical challenge because the original data were not prepared for direct 3D reconstruction [26]. A similar conversion focus is visible in studies that reconstruct 3D geological objects from 2D interpretation elements, where the sequence of preprocessing and geometric organization strongly influences the quality of later model generation [25]. In practical voxel-building studies using open borehole archives, data standardization is emphasized because the consistency of lithology coding directly controls the reliability of voxel class assignment [18].

The reviewed papers also show that workflow design is tightly coupled with the intended model representation. In implicit structural modeling, the workflow is typically organized around interfaces, orientations, and stratigraphic relationships because these are the principal constraints used to reconstruct continuous geological surfaces [9]. In structurally complex settings, the workflow remains strongly interpretation-led even when computational tools are advanced, because the ordering and consistency of geological constraints determine whether the resulting implicit framework is geologically plausible [10]. Recent implicit urban workflows move toward more automation, but they still retain rule-based geological guidance to preserve stratigraphic coherence when processing dense drilling records [11]. The potential-field extension proposed for unconformable interfaces further demonstrates that workflow changes are sometimes required specifically to handle difficult contact relationships that standard implicit implementations represent poorly [12].

In voxel workflows, the workflow emphasis shifts from surface reconstruction to volumetric discretization, category allocation, and multi-attribute storage. National and regional voxel model initiatives show that the workflow must support repeated integration of new observations and revised interpretations over time, which makes database structure and rule consistency as important as the interpolation step itself [13]. Comparative voxel model evolution studies also indicate that later generation workflows improve usability by refining update procedures and improving the organization of voxel attributes rather than only changing the final visualization [15]. Practical shallow subsurface voxel modeling studies demonstrate that voxel workflows can be tailored to engineering use by aligning grid construction and attribute assignment with user-oriented map products [14]. Later developments in the same line reinforce the importance of uncertainty-aware voxel update procedures when models are reused for planning and subsurface management [17]. Compression and representation studies show that voxel workflow performance can also depend on storage and rendering choices, which affects how feasible large 3D models are in routine use [16]. In engineering delivery contexts, voxel-based ground information can be structured to support downstream numerical analysis, which requires workflow planning from the beginning rather than post hoc conversion [19].

Automation appears in the reviewed corpus as a spectrum rather than a binary property. Some studies automate only repetitive preprocessing tasks while preserving manual interpretation at key stratigraphic decisions [26]. Other studies automate larger portions of the pipeline, including data ingestion, classification, and model construction, especially when the target is urban-scale production from many boreholes [28]. A GIS geoprocessing workflow can be highly automated in execution while still requiring expert selection of interpolation settings and classification logic, which highlights that automation shifts effort toward parameterization and quality control rather than removing expert judgement [29]. Hybrid modeling and rendering workflows further show that automation may be introduced for performance reasons, such as splitting regular voxel structures to improve display efficiency and web usability [27].

The data regime strongly influences which workflow architecture is feasible. Geophysics-led studies demonstrate that large-area coverage can be improved when airborne or ground geophysical information is integrated with boreholes, which changes the workflow from sparse point interpolation toward iterative interpretation and integration of areal or volumetric geophysical evidence [30]. AEM-based cognitive voxel modeling explicitly shows a workflow in which geophysical models are interpreted jointly with boreholes to construct geological volumes at scales that would be difficult to support with boreholes alone [31]. In offshore or infrastructure-oriented large-area modeling, multi-source integration is used to compensate for uneven direct investigation density, which again makes the workflow itself a critical methodological contribution [32].

Uncertainty-oriented methods also reshape the workflow because validation and uncertainty outputs are not appended only at the end, but influence model-building choices. Empirical Bayesian kriging is relevant in this context because it embeds uncertainty estimation within the interpolation process and therefore affects how property mapping workflows are configured and evaluated [20]. Hidden Markov random field style geological segmentation introduces a workflow in which probabilistic labeling and spatial context are integral to model construction, rather than optional post-processing [21]. Multi-source uncertainty analysis in 3D structural modeling shows that workflow stages must preserve source-specific uncertainty information if the final confidence assessment is to remain meaningful [22]. Synthetic-geology-based uncertainty studies further demonstrate that benchmark design and controlled experiments can be used as workflow components for testing how modeling choices influence uncertainty in outputs [23]. Recent geostatistical lithological modeling frameworks also indicate that predictive uncertainty is central to the model product and should be reflected in the workflow from data preparation onward [24].

Scalability is another major differentiator across the reviewed papers. In site-scale workflows, the primary objective is often a detailed local representation, which allows more manual intervention and tuning if data density is sufficient [10]. In city-scale or regional workflows, throughput, standardization, and updateability become dominant design constraints because the number of boreholes and the heterogeneity of records make bespoke modeling impractical [13]. Urban archive-based pipelines illustrate that the uneven spatial distribution of boreholes requires workflow logic that can detect data density contrasts and prevent overconfident extrapolation into poorly constrained zones [28]. GIS-based voxel workflows at site scale provide an intermediate case in which methods are detailed enough for geotechnical property mapping, but still structured in a way that supports reproducibility and later transfer to larger deployments [29].

To summarize the workflow comparison in a compact form for later use in further sections, Table 2 condenses the main distinctions in data regime, automation emphasis, and scaling behavior across the six taxonomy families.

Table 2 – Workflow and scalability patterns across the approach families

Approach family*	Dominant workflow bottleneck	Typical automation emphasis	Typical scale tendency	Main risk if workflow is weak
1	Constraint consistency and stratigraphic rule definition	Partial automation with expert-guided interpretation	Site to district	Geologically implausible continuity or interface conflicts
2	Data harmonization and voxel assignment consistency	Batch gridding, classification, attribute updating	Site to regional	False continuity and class artifacts in sparsely constrained cells
3	Preserving uncertainty information through model steps	Integrated probabilistic estimation and testing	Site to regional	Confidence outputs that do not reflect true workflow assumptions
4	Standardization of heterogeneous archives	Data ingestion, repeatable processing chains, batch generation	District to city	High throughput with low interpretive quality control
5	Schema conversion and geometry translation	Format conversion and delivery pipelines	Site to corridor / project system	Technically valid models becoming unusable in target platforms
6	Joint interpretation of geophysics and borehole constraints	Semi-automated inversion plus interpretation workflows	District to regional / corridor	Overinterpretation of geophysical patterns without sufficient calibration

* Enumeration of the approach family corresponds to Table 1.

The scalability patterns in Table 2 indicate that workflow robustness is a prerequisite for applicability. A method that performs well in a small expert-controlled demonstration can become unreliable when transferred to a municipal archive if data harmonization and automated quality control are not built into the pipeline [28]. Conversely, a highly automated pipeline may produce visually complete 3D outputs that are difficult to trust if the workflow does not preserve explicit uncertainty or validation checkpoints [22]. This tradeoff explains why several recent studies combine automation with stronger model checking or uncertainty-aware components rather than optimizing only processing speed [24].

The workflow perspective also clarifies that interoperability is not only an end-stage delivery issue. In FE-conversion studies, the possibility of generating analysis-ready ground models depends on earlier workflow decisions regarding geometric consistency and property assignment [34]. In broader geological information modeling and exchange studies, model updateability and data exchange are treated as design requirements that influence how the workflow is structured from the start [35]. Conceptual engineering-geology discussions similarly stress that the practical value of 3D ground models depends on fitness for purpose, which in workflow terms means aligning the modeling sequence with the intended decisions and users rather than producing a generic 3D model [33].

To support the reader visually, Figure 3 provides an infographic that positions the six approach families along two operational axes that recur in the reviewed corpus, namely automation intensity and dependence on expert interpretation. This figure is not a ranking, but a comparative orientation tool that complements the taxonomy in Table 1.

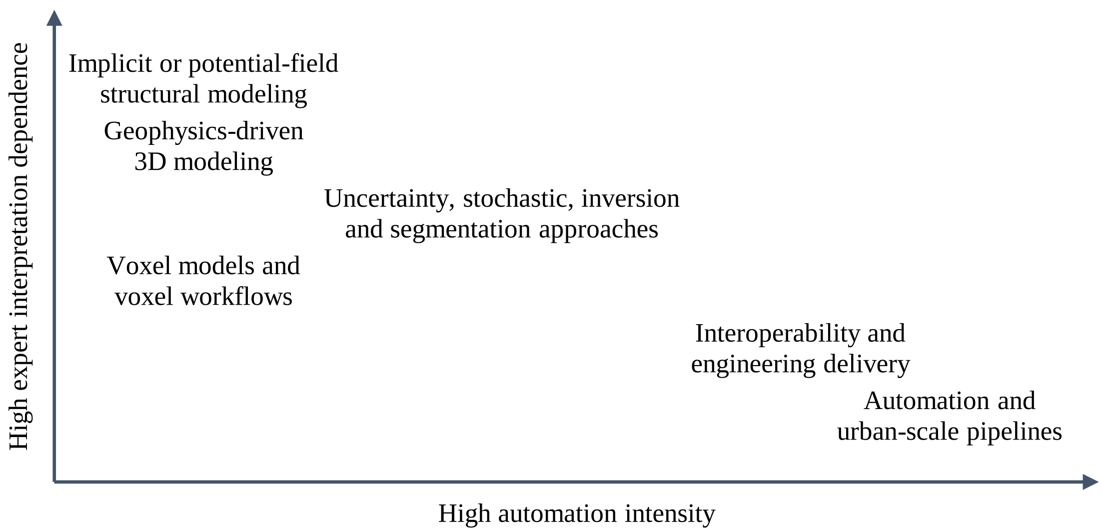

Figure 3 – Workflow automation intensity and dependence on expert interpretation (positions are schematic and indicate dominant workflow tendencies, not absolute properties of each family)

Overall, the reviewed literature shows that data-to-model workflows are central to the performance, credibility, and scalability of 3D subsurface cartography. The workflow determines how heterogeneous evidence is transformed, how much expert judgement is embedded or formalized, how uncertainty can be preserved, and whether the resulting model can be updated and delivered for practical use. This is why the next section shifts from workflow mechanics to credibility, focusing on validation, uncertainty, and comparability, including the boundary-mismatch problem, which becomes critical when multiple 3D models are used together.

5. Credibility: validation, uncertainty, and comparability

The credibility of a 3D subsurface cartographic product depends on whether it can be defended as an evidence-based representation rather than a visually plausible reconstruction. Within the reviewed corpus, credibility is established through three interconnected elements: validation of predictive behavior against observations, explicit treatment of uncertainty, and comparability of outputs when models are reused, updated, or combined across adjacent domains. In workflow-driven property mapping, credibility is often established through the repeatable evaluation of interpolation behavior and the systematic reporting of model performance across the 3D extent [29]. In structural reconstruction, credibility is closely tied to the consistency of constraints and the ability of the model to honor interface and orientation information without producing implausible artifacts [9]. In geophysics-led modeling, credibility is strongly influenced by how calibration boreholes anchor interpretations of geophysical volumes, because geophysical patterns alone can be ambiguous without ground truth constraints [31].

Validation practices differ by target variable and representation. When the mapped variable is continuous, validation is frequently expressed as predictive performance of an estimator at withheld locations, which aligns naturally with cross-validation logic in geostatistical workflows [20]. When the target is categorical, such as lithology or stratigraphic class, the validation problem becomes one of classification reliability and boundary correctness rather than numeric error alone, which motivates segmentation or probabilistic labeling formulations that incorporate spatial context [21]. In multi-source structural modeling, validation extends beyond point-wise error and includes the internal consistency of the reconstructed framework under varying combinations of input sources, because different data types may constrain different aspects of the geometry [22]. A complementary approach to validation appears in benchmark-oriented work where synthetic geology is used to test how uncertainty grows from modeling choices under controlled conditions, which provides a structured way to assess methodological sensitivity [23].

Uncertainty treatment is a second pillar of credibility because 3D subsurface mapping necessarily extrapolates beyond direct observation. In EBK-based approaches, uncertainty is not only a post-processing annotation but an intrinsic output associated with the estimation process, which enables uncertainty-aware interpretation of property fields [20]. In predictive geostatistical frameworks for lithological modeling, uncertainty can be treated as a primary deliverable that complements the most likely class assignment and supports decision-making under incomplete knowledge [24]. In large-scale voxel workflows, uncertainty is often addressed indirectly through model generation logic and update procedures, which can influence perceived reliability even when explicit probabilistic volumes are not produced [17]. In national or regional ground model programs, uncertainty and credibility are also linked to the governance of data updates and model revisions because a map changing over time must retain traceable provenance of inputs and assumptions [13].

Comparability is the third pillar and becomes critical once 3D subsurface cartography moves from single-case demonstrations to operational use. Comparability includes reproducibility of results under reruns, consistency under updates, and coherence when neighboring models are combined. In urban-scale production, uneven borehole density and heterogeneous logging practices create spatially varying confidence, which means that comparability across a city is partly a quality-control problem rather than only a modeling problem [28]. In voxel models intended for web delivery, representation choices such as voxel splitting and hierarchical organization can improve usability but also introduce discretization-dependent boundary behaviors that affect how adjacent tiles or model blocks align [27]. In interoperability and delivery contexts, comparability is affected by the conversion process itself because translation to FE-ready form can modify geometry and property allocation, which requires explicit checks to avoid introducing artificial discontinuities [34].

The reviewed literature implies that mismatches along shared boundaries arise through several recurring mechanisms. One mechanism is inconsistent conceptual constraints across models, such as different stratigraphic rules or horizon definitions, which can lead to incompatible surfaces even when both models honor local data [9]. A second mechanism is discretization mismatch, where different voxel sizes, grid origins, or conversion rules produce seams that are numerical artifacts rather than geological features [27]. A third mechanism is heterogeneity of uncertainty across the boundary, where one side is well constrained by dense investigation and the other is not, causing one model to extrapolate with unwarranted confidence relative to its neighbor [28]. A fourth mechanism is data-fusion asymmetry, where one model uses geophysical constraints and the adjacent model does not, which can produce different continuity assumptions in areas with sparse boreholes [30]. These mechanisms are actionable because they can be translated into seam-focused checks and reporting practices that complement traditional validation.

Figure 4 summarizes the credibility logic synthesized from the reviewed corpus. The scheme highlights where validation and uncertainty should be inserted into the workflow and where seam comparability checks are necessary when multiple models are intended to be mosaicked or compared.

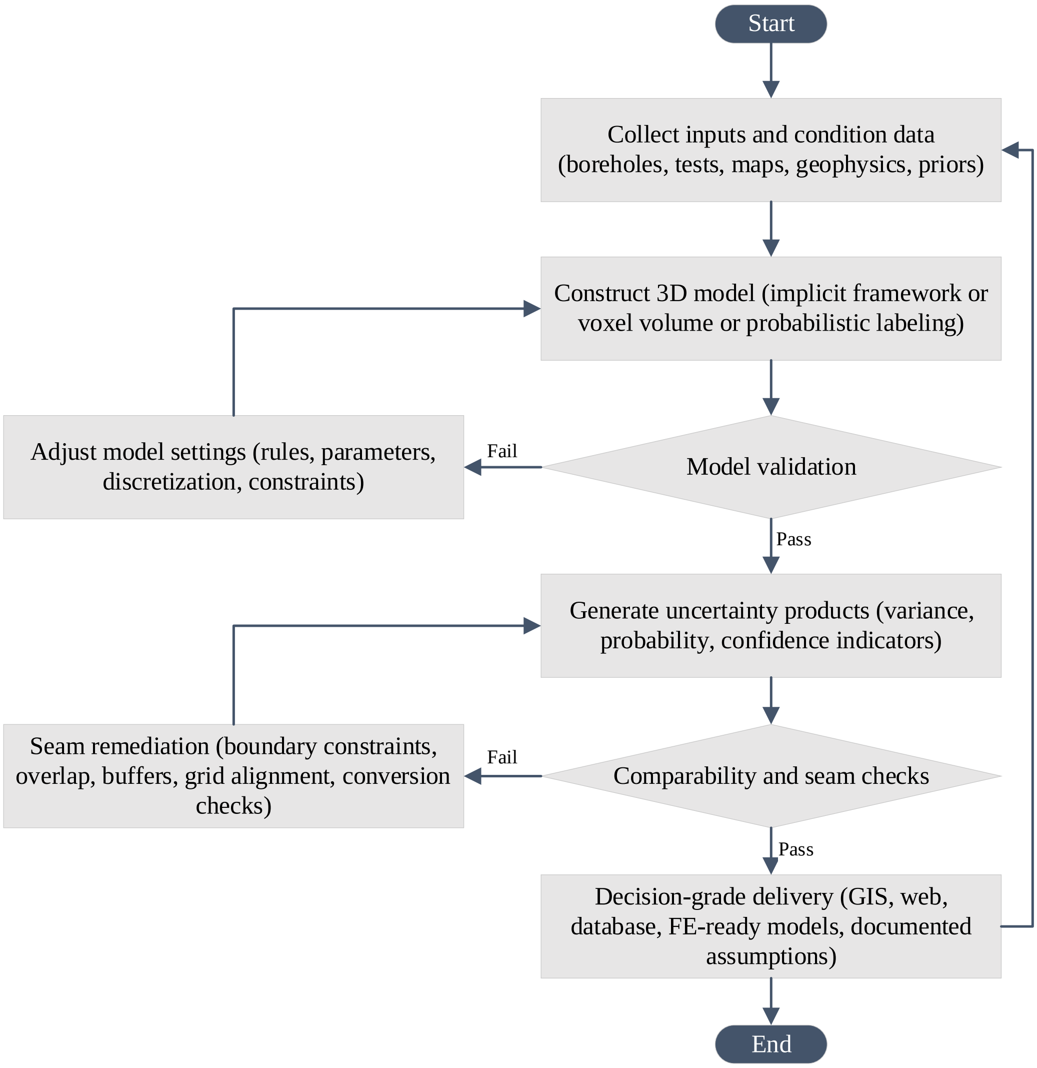

Figure 4 – Scheme of credibility building in 3D subsurface cartography

To support a compact comparison that can be used in the next section, Table 3 lists representative credibility features from selected studies. The intent is not to rank methods, but to show how validation, uncertainty, and seam comparability are treated across different approach families.

Table 3 – Representative credibility practices across the reviewed approach families

Paper	Primary credibility focus	Validation approach emphasized	Uncertainty product emphasized	Comparability implication
[20]	Estimator behavior and uncertainty	Cross-validation as estimator evaluation	Prediction uncertainty associated with EBK	Enables uncertainty-aware comparison between areas
[21]	Categorical model reliability	Spatially contextual labeling for classes	Probabilistic classification behavior	Supports boundary interpretation as uncertainty zones
[22]	Multi-source confidence assessment	Sensitivity to input source combinations	Explicit uncertainty assessment under multi-source inputs	Highlights risk of inconsistent constraints across neighbors
[23]	Method sensitivity under controlled truth	Synthetic benchmark testing	Quantified uncertainty driven by modeling choices	Provides basis for comparing methods on shared benchmarks
[28]	Operational quality control at urban scale	Handling uneven borehole distributions	Confidence varies with data density	Seams often reflect differing constraint strength across districts
[34]	Delivery credibility after conversion	Consistency during FE-ready conversion	Implicit uncertainty introduced by translation	Seams can be introduced by conversion rules if unchecked

Overall, credibility in 3D subsurface cartography emerges as an interplay between modeling choices and verification culture. Methods that provide explicit uncertainty products make it easier to communicate where the model is informative and where it is speculative, which strengthens interpretability for geotechnical ground characterization [24]. Workflows that scale to city or regional settings must treat data harmonization and quality control as credibility mechanisms because the model inherits biases and inconsistencies from the archive [18]. Approaches designed for practical delivery must include comparability checks at the interface between modeling and downstream platforms because translation can otherwise compromise the integrity of mapped layers and properties [35]. These findings motivate the translation of the reviewed evidence into applicability guidance and reporting requirements for decision-grade 3D subsurface cartographic products.

6. Applicability to geotechnical subsurface decision support

This section translates the reviewed evidence into practical guidance on when a 3D subsurface cartographic product can be treated as decision-grade for geotechnical ground characterization. In this review, applicability is defined as fitness for the purpose of the subsurface information product, meaning that the model must be consistent with the available evidence, transparent about uncertainty, and deliverable in a form that supports engineering use. [33] frames the practical value of 3D ground models in terms of suitability for the intended decisions rather than visual completeness, which motivates an applicability lens that evaluates products by their constraints, outputs, and limitations rather than by their geometric sophistication.

A first applicability condition concerns the dominant target of mapping. When the central goal is stratigraphic architecture, implicit structural modeling is often used because it is built around interfaces, orientations, and stratigraphic consistency constraints rather than cell-by-cell assignment [9]. When the central goal is multi-attribute volumes, voxel workflows are frequently chosen because they support volumetric querying, property statistics, and consistent grid-based extraction of information products [13]. When a project requires decision support under incomplete and heterogeneous evidence, approaches that treat uncertainty as a primary output become more directly applicable due they can communicate where the model is informative and where it is speculative [24].

A second applicability condition concerns spatial coverage and data regime. In regions where boreholes are sparse or uneven, geophysics-driven modeling can improve areal continuity by providing volumetric constraints that are then calibrated against boreholes [31]. In urban settings with dense but heterogeneous borehole archives, applicability depends strongly on whether the workflow includes systematic ingestion and quality control because uneven distribution can otherwise produce misleading extrapolation patterns [28]. In practical implementations based on open borehole logs, applicability increases when the workflow emphasizes consistent coding and pragmatic modeling choices that match the quality and granularity of available logs [18].

A third applicability condition is credibility, which is inseparable from validation and uncertainty communication. [20] shows that geostatistical estimation can provide uncertainty outputs together with predictions, which supports uncertainty-aware interpretation of continuous property fields. [21] demonstrates that categorical subsurface modeling benefits from probabilistic labeling ideas where spatial context is used to improve class assignment reliability, which is particularly relevant when the map product is a lithology volume. [23] argues that controlled benchmark settings using synthetic geology can reveal how modeling choices propagate into uncertainty, which supports method selection and reporting for decision-grade mapping.

A fourth applicability condition is comparability and integration. [27] highlights that performance-oriented voxel structuring can be essential for delivery and usability, but discretization choices can influence how seams and boundaries appear when models are tiled or merged. [34] shows that conversion to analysis-ready formats is not a neutral step because translation can alter geometry and property allocation if constraints are not preserved, which affects whether a subsurface model remains decision-grade after delivery. [35] emphasizes the importance of interoperable ground information structures and exchange logic, which becomes a practical applicability requirement when multiple stakeholders and platforms must reuse the same subsurface product.

Figure 5 provides a review-generated decision flow that operationalizes these conditions as a minimal applicability screening procedure. The scheme is designed to be applied before adopting a 3D subsurface cartographic product in a geotechnical decision-support context.

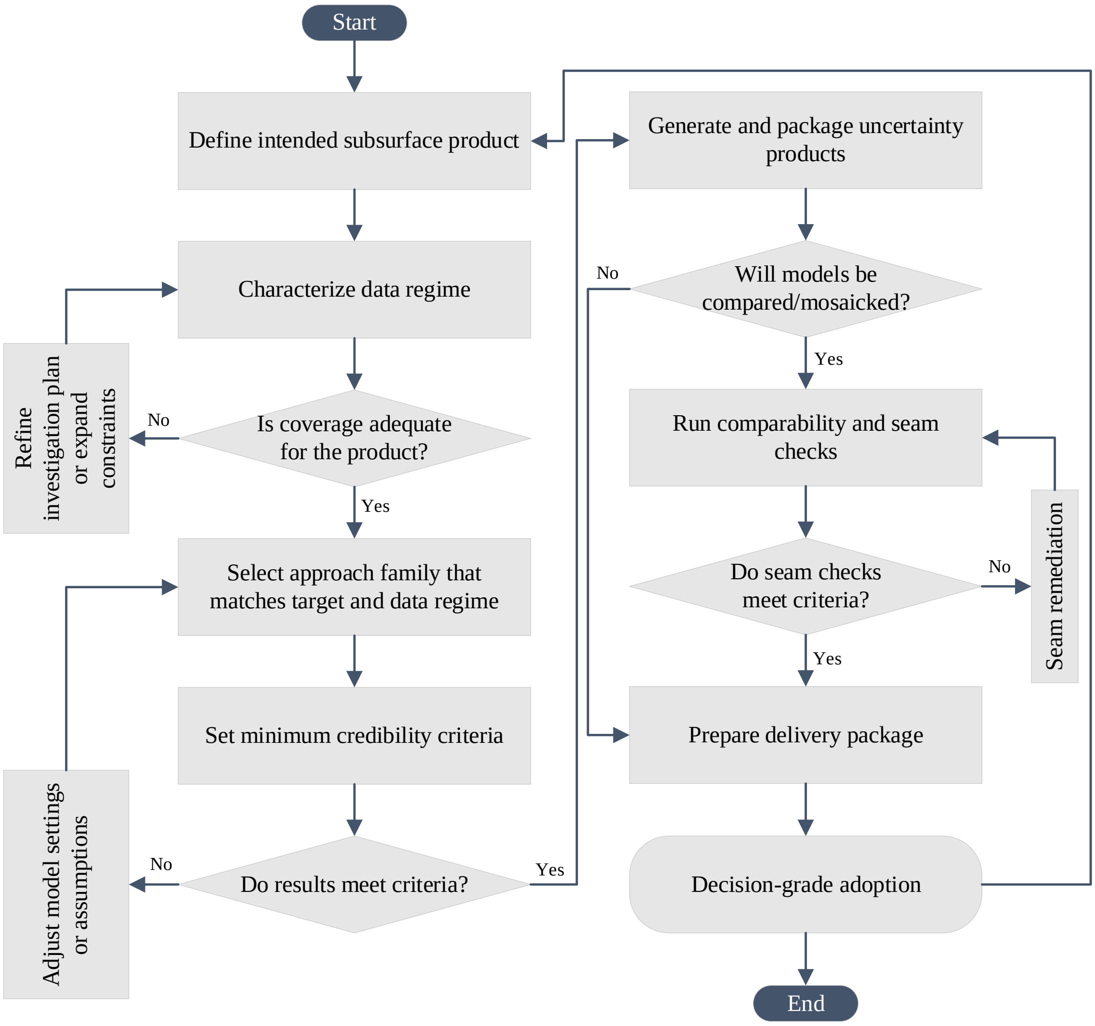

Figure 5 – Applicability screening flow for 3D subsurface cartographic products

To make applicability guidance concrete, Table 4 summarizes representative use-case patterns that recur in the reviewed corpus. Each row is grounded in one paper that exemplifies the decision context and the associated workflow implications.

Table 4 – Use-case patterns for decision-grade 3D subsurface mapping

Decision-support need	Dominant data regime	Recommended approach family	Minimum credibility evidence expected	Representative source
Coherent stratigraphic architecture for site-scale interpretation	Interfaces, orientations, stratigraphic constraints, limited property targets	Implicit or potential-field structural modeling	Plausibility and constraint-consistency checks that demonstrate honored inputs	[9]
Multi-attribute volumetric subsurface map for querying and statistics	Boreholes and logs with multiple attributes in a consistent coding scheme	Voxel models and voxel workflows	Demonstrated robustness of voxel assignment rules and traceable update logic	[13]
Urban-scale production from large heterogeneous borehole archives	Dense but uneven and heterogeneous borehole distribution	Automation and urban-scale pipelines	Quality-control logic that accounts for data-density contrasts and prevents overconfident extrapolation	[28]
Extending spatial coverage beyond borehole-only constraints	Geophysical models with calibration boreholes	Geophysics-driven 3D modeling	Explicit calibration logic tying geophysics interpretation to borehole control	[31]
Decision-support where uncertainty must be communicated explicitly	Mixed constraints with incomplete coverage	Uncertainty-focused geostatistical framework	Uncertainty products paired with predictions that can be interpreted as confidence indicators	[24]
Analysis-ready subsurface product for downstream numerical modeling	Existing model plus requirement for conversion to FE-ready form	Interoperability and engineering delivery	Verification that conversion preserves geometry and property allocation constraints	[34]

Across the corpus, the strongest determinant of applicability is not the label of the method family but whether the produced 3D map satisfies a small set of decision-grade conditions. [10] shows that structurally complex cases demand careful constraint management because even powerful modeling tools can produce misleading continuity if structural rules are not enforced. [17] indicates that voxel models used for planning and management benefit when uncertainty and model revision behavior are addressed as operational issues rather than treated as a one-time model build. [29] demonstrates that a reproducible GIS workflow strengthens applicability by making model generation repeatable under new parameter settings or updated datasets, which is important when the subsurface map is treated as a living product.

Based on these patterns, the following applicability checklist can be used as a compact reporting and adoption guide, and it will be expanded into a formal reporting checklist in the final synthesis. [32] illustrates that for large-area ground model applications, explicit documentation of data sources, coverage limitations, and integration logic is essential because spatial completeness can otherwise be mistaken for evidential completeness. [22] shows that in multi-source contexts, applicability improves when uncertainty contributions from different sources are preserved and compared rather than merged without traceability.

Checklist items to report or verify before treating a 3D subsurface map as decision-grade for geotechnical ground characterization include a stated target variable and decision context, an explicit description of the data regime and coverage limitations, a documented representation and inference choice with key settings, validation evidence appropriate to the target variable, uncertainty communication appropriate to the use-case, and integration details covering delivery formats, update procedure, and seam comparability expectations where models will be mosaicked. [33] supports this orientation by emphasizing that the operational value of a 3D ground model follows from its alignment with the intended engineering use, which in this review is formalized as applicability conditions.

7. Conclusions

This review synthesized the current state of 3D subsurface cartography for geotechnical purposes by organizing the selected literature into a taxonomy aligned with the Litmaps-based clustering and by comparing how different approach families transform subsurface observations into

3D stratigraphic and or property products. The analysis indicates that there is no single dominant solution. Instead, complementary families prioritize different outcomes, including structural consistency of stratigraphy, volumetric querying of lithology and properties, explicit uncertainty communication, operational automation at urban scale, geophysics-led extension of spatial coverage, and interoperability for engineering delivery.

A key finding is that workflow design is as important as the final representation. Decision-grade mapping requires explicit data harmonization, traceable assumptions, and repeatable processing rather than only visually complete models. Credibility depends on validation logic appropriate to the mapped product and on uncertainty communication that clarifies where the model is constrained by evidence and where it is extrapolative.

Comparability becomes critical when models are reused, updated, or combined across adjacent domains. Boundary mismatches can arise from inconsistent conceptual rules, discretization differences, unequal data density, and asymmetric auxiliary constraints. For this reason, seam checks and remediation strategies should be treated as standard workflow elements when mosaicking or cross-area comparison is expected.

This review is subject to several limitations. Because the literature corpus was assembled through a Litmaps citation-network workflow, the selection may favor well-connected and more frequently cited studies, while very recent papers, less-cited contributions, regional publications, and non-indexed sources may be underrepresented. In addition, although the coding and tagging procedure was applied consistently, the assignment of papers to approach families involved author judgement. Accordingly, the proposed taxonomy should be interpreted as a transparent synthesis of the selected corpus rather than as an exhaustive or uniquely fixed classification of the entire field.

Overall, the reviewed evidence supports an applicability view where method selection should be guided by the mapping objective and data regime, then verified against minimum credibility and integration requirements. Future work should prioritize workflow-level uncertainty propagation, more standardized evaluation practices, improved seam-consistency methods, and stronger interoperability across GIS, web visualization, databases, and engineering delivery environments.

Acknowledgments

This research was funded by the Science Committee of the Ministry of Science and Higher Education of the Republic of Kazakhstan (Grant No. AP26198009).

References

[1] K.-K. Phoon and F. H. Kulhawy, "Characterization of geotechnical variability," *Can. Geotech. J.*, vol. 36, no. 4, pp. 612–624, Nov. 1999, doi: 10.1139/t99-038.

[2] H. Ali and J. Choi, "A Review of Underground Pipeline Leakage and Sinkhole Monitoring Methods Based on Wireless Sensor Networking," *Sustainability*, vol. 11, no. 15, p. 4007, Jul. 2019, doi: 10.3390/su11154007.

[3] K.-K. Phoon *et al.*, "Geotechnical uncertainty, modeling, and decision making," *Soils and Foundations*, vol. 62, no. 5, p. 101189, Oct. 2022, doi: 10.1016/j.sandf.2022.101189.

[4] M. G. Culshaw, "From concept towards reality: developing the attributed 3D geological model of the shallow subsurface," *QJEGH*, vol. 38, no. 3, pp. 231–284, Aug. 2005, doi: 10.1144/1470-9236/04-072.

[5] R. A. Bowden, "Building confidence in geological models," *SP*, vol. 239, no. 1, pp. 157–173, Jan. 2004, doi: 10.1144/GSL.SP.2004.239.01.11.

[6] W. Hou *et al.*, "Assessing quality of urban underground spaces by coupling 3D geological models: The case study of Foshan city, South China," *Computers & Geosciences*, vol. 89, pp. 1–11, Apr. 2016, doi: 10.1016/j.cageo.2015.07.016.

[7] M. J. Page *et al.*, "The PRISMA 2020 statement: an updated guideline for reporting systematic reviews," *BMJ*, p. n71, Mar. 2021, doi: 10.1136/bmj.n71.

[8] "Litmaps – About." Accessed: Oct. 16, 2025. [Online]. Available: https://www.litmaps.com/about/us

[9] P. Calcagno, J. P. Chilès, G. Courrioux, and A. Guillen, "Geological modelling from field data and geological knowledge," *Physics of the Earth and Planetary Interiors*, vol. 171, no. 1–4, pp. 147–157, Dec. 2008, doi: 10.1016/j.pepi.2008.06.013.

[10] J. M. Thornton, G. Mariethoz, and P. Brunner, "A 3D geological model of a structurally complex Alpine region as a basis for interdisciplinary research," *Sci Data*, vol. 5, no. 1, p. 180238, Oct. 2018, doi: 10.1038/sdata.2018.238.

[11] J. Guo *et al.*, "Three-dimensional geological modeling and spatial analysis from geotechnical borehole data using an implicit surface and marching tetrahedra algorithm," *Engineering Geology*, vol. 284, p. 106047, Apr. 2021, doi: 10.1016/j.enggeo.2021.106047.

[12] P. Liu, Z. Li, G. Yu, and Z. Li, "Three-Dimensional Geological Modeling Method Based on Potential Vector Fields," *Applied Sciences*, vol. 15, no. 7, p. 3594, Mar. 2025, doi: 10.3390/app15073594.

[13] J. Stafleu, D. Maljers, J. L. Gunnink, A. Menkovic, and F. S. Busschers, "3D modelling of the shallow subsurface of Zeeland, the Netherlands," *Netherlands Journal of Geosciences*, vol. 90, no. 4, pp. 293–310, Dec. 2011, doi: 10.1017/S0016774600000597.

[14] Hademenos, V., Van Lancker, V., Missiaen, T., and Stafleu, J., "Preliminary results on the 3D voxel model of the subsurface of the Belgian Continental Shelf," in *Book of abstracts – VLIZ Young Scientists' Day*, Brugge, Belgium: VLIZ Special Publication, 71, 2015, p. 69.

[15] D. Maljers, J. Stafleu, M. J. Van Der Meulen, and R. M. Dambrink, "Advances in constructing regional geological voxel models, illustrated by their application in aggregate resource assessments," *Netherlands Journal of Geosciences*, vol. 94, no. 3, pp. 257–270, Sep. 2015, doi: 10.1017/njg.2014.46.

[16] A. Graciano, A. J. Rueda, and F. R. Feito, "Real-time visualization of 3D terrains and subsurface geological structures," *Advances in Engineering Software*, vol. 115, pp. 314–326, Jan. 2018, doi: 10.1016/j.advengsoft.2017.10.002.

[17] V. Hademenos, J. Stafleu, T. Missiaen, L. Kint, and V. R. M. Van Lancker, "3D subsurface characterisation of the Belgian Continental Shelf: a new voxel modelling approach," *Netherlands Journal of Geosciences*, vol. 98, p. e1, 2019, doi: 10.1017/njg.2018.18.

[18] S. Nonogaki, S. Masumoto, T. Nemoto, and T. Nakazawa, "Voxel modeling of geotechnical characteristics in an urban area by natural neighbor interpolation using a large number of borehole logs," *Earth Sci Inform*, vol. 14, no. 2, pp. 871–882, Jun. 2021, doi: 10.1007/s12145-021-00600-x.

[19] K. Micić, H.-G. Bui, and J. Ninić, "Computer-aided ground modelling incorporating soil variability for geotechnical applications," in *Proceedings of the Southeastern Europe Tunnelling Conference (SETC-2025)*, Belgrade, Serbia: Serbian Association for Tunnels and Underground Structures (ITA Serbia), 2025, pp. 283–293. doi: 10.5937/SETC25026M.

[20] K. Krivoruchko, "Empirical Bayesian Kriging Implemented in ArcGIS Geostatistical Analyst," *ArcUser*, vol. 15, no. 4, pp. 6–10, 2012.

[21] H. Wang, J. F. Wellmann, Z. Li, X. Wang, and R. Y. Liang, "A Segmentation Approach for Stochastic Geological Modeling Using Hidden Markov Random Fields," *Math Geosci*, vol. 49, no. 2, pp. 145–177, Feb. 2017, doi: 10.1007/s11004-016-9663-9.

[22] D. Liang, W. Hua, X. Liu, Y. Zhao, and Z. Liu, "Uncertainty assessment of a 3D geological model by integrating data errors, spatial variations and cognition bias," *Earth Sci Inform*, vol. 14, no. 1, pp. 161–178, Mar. 2021, doi: 10.1007/s12145-020-00548-4.

[23] S.-J. Wang, Q. C. Nguyen, Y.-C. Lu, Y. G. Doyoro, and D.-H. Tran, "Evaluation of geological model uncertainty caused by data sufficiency using groundwater flow and land subsidence modeling as example," *Bull Eng Geol Environ*, vol. 81, no. 8, p. 331, Aug. 2022, doi: 10.1007/s10064-022-02832-7.

[24] A. Abdelsattar and E. E.-D. Hemdan, "A Geostatistical Predictive Framework for 3D Lithological Modeling of Heterogeneous Subsurface Systems Using Empirical Bayesian Kriging 3D (EBK3D) and GIS," *Geomatics*, vol. 5, no. 4, p. 60, Oct. 2025, doi: 10.3390/geomatics5040060.

[25] J. Gou, W. Zhou, and L. Wu, "IMPLICIT THREE-DIMENSIONAL GEO-MODELLING BASED ON HRBF SURFACE," *Int. Arch. Photogramm. Remote Sens. Spatial Inf. Sci.*, vol. XLII-2/W2, pp. 63–66, Oct. 2016, doi: 10.5194/isprs-archives-XLII-2-W2-63-2016.

[26] J. Guo, L. Wu, W. Zhou, J. Jiang, and C. Li, "Towards Automatic and Topologically Consistent 3D Regional Geological Modeling from Boundaries and Attitudes," *IJGI*, vol. 5, no. 2, p. 17, Feb. 2016, doi: 10.3390/ijgi5020017.

[27] J. Li, P. Liu, X. Wang, H. Cui, and Y. Ma, "3D geological implicit modeling method of regular voxel splitting based on layered interpolation data," *Sci Rep*, vol. 12, no. 1, p. 13840, Aug. 2022, doi: 10.1038/s41598-022-17231-x.

[28] X. Wang *et al.*, "Towards automatic and rapid 3D geological modelling of urban sedimentary strata from a large amount of borehole data using a parallel solution of implicit equations," *Earth Sci Inform*, vol. 17, no. 1, pp. 421–440, Feb. 2024, doi: 10.1007/s12145-023-01164-8.

[29] Y. Utepov, A. Aldungarova, A. Mukhamejanova, T. Awwad, S. Karaulov, and I. Makasheva, "Voxel Interpolation of Geotechnical Properties and Soil Classification Based on Empirical Bayesian Kriging and Best-Fit Convergence Function," *Buildings*, vol. 15, no. 14, p. 2452, Jul. 2025, doi: 10.3390/buildings15142452.

[30] F. Jørgensen, R. Rønde Møller, P. B. E. Sandersen, and L. Nebel, "3-D geological modelling of the Egebjerg area, Denmark, based on hydrogeophysical data," *GEUS Bulletin*, vol. 20, pp. 27–30, Jul. 2010, doi: 10.34194/geusb.v20.4892.

[31] F. Jørgensen, R. R. Møller, L. Nebel, N.-P. Jensen, A. V. Christiansen, and P. B. E. Sandersen, "A method for cognitive 3D geological voxel modelling of AEM data," *Bull Eng Geol Environ*, vol. 72, no. 3–4, pp. 421–432, Dec. 2013, doi: 10.1007/s10064-013-0487-2.

[32] X. Peng *et al.*, "Development of a 3D Ground Model for an Offshore Wind Farm with Complex Interlayering of Silty Soils," in *Proceedings of the 7th International Conference on Geotechnical and Geophysical Site Characterization*, Barcelona, Spain: CIMNE, 2024. doi: 10.23967/isc.2024.301.
[33] R. Hack, B. Orlic, S. Ozmutlu, S. Zhu, and N. Rengers, "Three and more dimensional modelling in geo-engineering," *Bull Eng Geol Environ*, vol. 65, no. 2, pp. 143–153, May 2006, doi: 10.1007/s10064-005-0021-2.
[34] B. Wang and S. Bauer, "Converting heterogeneous complex geological models to consistent finite element models: methods, development, and application to deep geothermal reservoir operation," *Environ Earth Sci*, vol. 75, no. 20, p. 1349, Oct. 2016, doi: 10.1007/s12665-016-6138-8.
[35] M. S. Khan, I. S. Kim, and J. Seo, "A boundary and voxel-based 3D geological data management system leveraging BIM and GIS," *International Journal of Applied Earth Observation and Geoinformation*, vol. 118, p. 103277, Apr. 2023, doi: 10.1016/j.jag.2023.103277.

Information about authors:
Nurgul Alibekova – PhD, Associate Professor; 1) Scientific Supervisor, Solid Research Group, LLP, Astana, Kazakhstan; 2) Associate Professor, Department of Civil Engineering, L.N. Gumilyov Eurasian National University, Astana, Kazakhstan; nt_alibekova@mail.ru
Aleksej Aniskin – Candidate of Technical Sciences, Associate Professor, Department of Civil Engineering, University North, Varaždin, Croatia, aaniskin@unin.hr
Kairat Mukhambetkaliev – Candidate of Technical Sciences, Leading Researcher, JSC "Kazakhstan Road Research Institute", Astana, Kazakhstan, k.mukhambetkaliyev@qazjolgzi.kz
Indira Makasheva – MSc; 1) Junior Researcher, Solid Research Group, LLP, Astana, Kazakhstan; 2) PhD Student, Department of Civil Engineering, L.N. Gumilyov Eurasian National University, Astana, Kazakhstan; indira.yergaliyeva@gmail.com

Author Contributions:
Nurgul Alibekova – concept, methodology, resources, interpretation.
Aleksej Aniskin – methodology, editing.
Kairat Mukhambetkaliev – analysis, funding acquisition.
Indira Makasheva – data collection, analysis, visualization, drafting.

Conflict of Interest: The authors declare no conflict of interest.

Use of Artificial Intelligence (AI): Litmaps was used to assist with identifying and organizing relevant publications, and Grammarly was used to improve language and clarity. All methodological decisions, interpretations, and final wording were verified and approved by all the authors.

Received: 19.12.2025
Revised: 18.03.2026
Accepted: 19.03.2026
Published: 22.03.2026

Technobius, 2026, 6(1), 0098, DOI: https://doi.org/10.54355/tbus/6.1.2026.0098

Technobius

https://technobius.kz/

e-ISSN 2789-7338

Article

Effect of waste glass powder particle size, content, and compaction pressure on the properties of autoclaved silicate brick

Sarsenbek Montayev [1], Bolatbek Sakhiev[1,*], Sabit Zharylgapov[1], Ainur Montayeva[2]

[1]Research Laboratory of Construction Materials and Technologies, West Kazakhstan Agrarian and Technical University named after Zhangir Khan, Uralsk, Republic of Kazakhstan
[2]Department of Architecture and Construction, Korkyt Ata Kyzylorda University, Kyzylorda, Republic of Kazakhstan
*Correspondence: bolatbeksahiev5@gmail.com

Abstract. The present study evaluates the influence of waste glass powder particle size distribution, dosage, and compaction pressure on the performance of autoclaved silicate brick. Glass powder produced from container glass waste was incorporated into a quartz–lime mixture at 5, 10, and 15 wt.% in four fractions: ≤63, 63-140, 140-315, and 315-630 μm. The specimens were formed by semi-dry pressing and subjected to autoclave curing. Their average density, compressive strength, water absorption, thermal conductivity, and frost resistance were then determined. The results demonstrated that the modifying effect of glass powder strongly depends on its dispersity. The most favorable performance was obtained with the finest fraction (≤63 μm) at 10 wt.% and 10 MPa compaction pressure, where the average density reached 1860 kg/m^3, compressive strength 14.5 MPa, water absorption 11.3%, and thermal conductivity 0.77 W/(m·°C). Coarser fractions showed a progressively weaker effect, and the 315–630 μm fraction was unfavorable relative to the reference composition. Frost resistance remained at F50 for all specimens. Increasing compaction pressure from 5 to 15 MPa enhanced densification and strength development while only slightly changing thermal conductivity. The results confirm the potential of finely ground waste glass as an effective modifying additive for silicate brick production.
Keywords: autoclaved silicate brick, waste glass powder, particle size distribution, compaction pressure, compressive strength, water absorption, thermal conductivity.

1. Introduction

Silicate brick remains an important wall material because it combines relatively simple raw materials with hydrothermal curing, and its service properties are governed not only by composition but also by particle packing, molding pressure, and phase formation during autoclaving [1]. Interest in this material has grown further in the context of sustainable construction, since sand-lime products can serve as a platform for incorporating industrial by-products and recycled mineral components without abandoning established production technology [2]. At the same time, conventional silicate products still face a practical materials challenge: their overall performance must be improved in a balanced way, because strength, density, water absorption, thermal conductivity, and durability are interrelated rather than independent characteristics [3].

One of the most promising approaches is the use of waste glass, since soda-lime glass is rich in amorphous silica and can act not only as an inert filler but also as a reactive component under alkaline and hydrothermal conditions [4]. Finely ground glass is known to exhibit pozzolanic reactivity, and its activity increases as particle size decreases because the specific surface area rises and the amorphous network becomes more accessible to dissolution and secondary hydrate formation [5]. The ability of glass powder to react with calcium-bearing systems has also been confirmed in studies showing that it can consume portlandite and contribute to the formation of additional binding phases, which explains why the particle size of the glass component often becomes a key technological variable rather than a secondary parameter [6].

In autoclaved sand-lime systems, this issue is especially important because replacing part of the quartz component with glass changes both the kinetics of hydrothermal reactions and the resulting pore structure. [2] reported that glass sand can improve the compressive strength of autoclaved products relative to traditional silicate units, linking this effect to the altered course of hydrothermal synthesis and the formation of a favorable microstructure. In a later study, the same research group showed that glass-containing autoclaved bricks differ from conventional ones not only in strength but also in reaction temperature, phase assemblage, and bond formation, confirming that amorphous glass behaves differently from crystalline quartz during processing [3]. Pore-structure analysis of autoclaved materials modified with glass sand further demonstrated that the glass component can substantially change the distribution and character of pores, which is directly relevant to water absorption and density [7].

At the same time, the literature does not support a universally positive effect of glass addition, and this makes optimization necessary. [6], who examined autoclaved silica-lime materials made with different waste container glasses, found that the type of glass and the resulting structure strongly influenced density, water absorption, and strength, so the benefit of glass incorporation depended on the specific formulation rather than on the fact of replacement alone [8]. Similar non-monotonic behavior is also seen in related autoclaved systems modified by other mineral wastes. For example, basalt powder in sand-lime products showed the best results at around 10% addition, while higher dosages became less favorable [9]. A later microstructural study of basalt-modified autoclave brick confirmed that moderate waste additions can improve performance, whereas excessive replacement disrupts the optimal structure formation pathway [10]. In the same way, mixture-design work on sand-lime bricks produced with coal tailings showed that strength responds sensitively to raw-material proportions, so there is a narrow compositional window in which desirable properties are maximized [11].

The role of particle size is equally unresolved in the broader brick literature. In fired bricks containing waste glass, [12] showed that glass particle size significantly affects density, water absorption, compressive strength, and thermal conductivity, and that not every increase in fineness is beneficial. [13] also reported that waste glass can increase compressive strength and decrease water absorption in brick materials, but the magnitude of the effect depends on dosage and the way the glass modifies porosity. [14] found an optimum replacement level for waste glass powder in fired bricks rather than a linear improvement with increasing content, which again points to the need for dosage optimization. [12], [13], [14] are not directly transferable to autoclaved silicate brick, but they consistently show that glass content and dispersity control the balance between densification, reactivity, and pore development.

Thermal performance adds another layer to the problem. In some sand-lime systems, porous glass-based additives markedly reduce thermal conductivity by lowering density and increasing closed porosity. In contrast, [15] observed in fired clay bricks with waste glass sludge that denser microstructures created by glass addition can improve strength while increasing thermal conductivity, showing that the thermal effect of glass is system-specific and must be interpreted together with density and pore structure [16]. Autoclaved lime-based bricks produced from fly ash, sand, and lime also demonstrate that forming pressure has a direct effect on density, compressive strength, water absorption, and thermal conductivity, which means that raw-material optimization alone is insufficient if technological parameters are not considered simultaneously [1]. Likewise, autoclaved lime-saline soil bricks exhibited property changes that depended strongly on composition and processing, including durability behavior under freezing and thawing [16].

Therefore, the current research problem is not simply whether waste glass can be used in silicate brick, but what particle size distribution, dosage, and compaction pressure provide the best combined set of physical, mechanical, thermophysical, and durability properties in an autoclaved quartz-lime system. Existing studies [2], [3], [8] confirm the relevance of glass waste utilization in sand-lime materials, but they do not sufficiently resolve the combined influence of fractional particle size distribution, moderate glass content variation, and semi-dry compaction pressure within one experimental program. This gap is practically important because an additive that lowers water absorption may not necessarily maximize strength, and a denser structure may not automatically give the most favorable thermal conductivity.

Against this background, the present study aims to determine how the fraction size of powdered glass waste, its content in the silicate mixture, and the applied compaction pressure influence the comprehensive performance of autoclaved silicate brick. To achieve this aim, the study evaluates the effects of four glass powder fractions and three dosage levels on density, compressive strength, water absorption, thermal conductivity, and frost resistance, identifies the most effective glass fraction and content, and then investigates how varying compaction pressure affects the properties of the composition found to be optimal. In this way, the work addresses both the scientific issue of structure-property relationships in glass-modified silicate systems and the practical issue of selecting technologically justified parameters for recycling glass waste in silicate brick production.

2. Methods

2.1 Materials

The experimental study was carried out based on a conventional quartz-lime system widely used in the production of silicate brick. The initial raw material was a base silicate mixture obtained from a silicate brick manufacturing plant (JSC West Kazakhstan Corporation of Building Materials, Uralsk, Kazakhstan).

According to regulatory documentation [17] for the production of silicate products, the silicate mixture consists of quartz sand, construction lime, and water.

Quartz-feldspar sand from the Melovye Gorki deposit, located 5.5-6 km southeast of Uralsk (Kazakhstan), was used as the siliceous component. The silica (SiO_2) content in the sand was approximately 83.5%, confirming its suitability for use in silicate materials according to [18]. The content of quartz sand in the mixture ranged from 70 to 85%. Ground quicklime of slow slaking type (Grade I) was used as the binding component. The lime was introduced into the mixture in an amount of 8-10 wt.%. The content of amorphous SiO_2 in the glass powder is approximately 70-74%. The glass powder was introduced into the silicate mixture in amounts of 5, 10, and 15 wt.% with partial replacement of quartz sand. Glass powder obtained from container glass waste was used as a modifying additive. The glass waste was preliminarily crushed and then ground in a laboratory ball mill (dry grinding type) of the MSHSP-08 model (JSC Tyazhmash, Syzran, Russia), followed by sieving. The particle size distribution of the glass powder was determined by sieve analysis using a laboratory vibrating sieve SLV-200-11 (VIBROTECHNIK LLC, Saint Petersburg, Russia). Based on the results, the powder was classified into the following particle size fractions: ≤63 μm, 63-140 μm, 140-315 μm, and 315-630 μm. The selected parameters above correspond to standard technological requirements for silicate brick production [19].

2.2 Experimental program

The experimental program was aimed at evaluating the influence of the particle size distribution of glass powder, its content, and compaction pressure on the performance properties of silicate brick. The following parameters were investigated:

- Glass powder content (5, 10, and 15 wt.%);
- Particle size distribution (≤63, 63-140, 140-315, and 315-630 μm);
- Compaction pressure (5-15 MPa).

The optimal particle size fraction and dosage of glass powder were determined based on a comprehensive analysis of the physical, mechanical, and thermophysical properties of the obtained specimens.

2.3 Specimens preparation

The initial components were first subjected to dry manual mixing under laboratory conditions until a homogeneous mixture was obtained. After dry mixing, water was added to achieve a moisture content of 6-8 wt.%, which corresponds to the requirements of semi-dry pressing technology widely used in silicate brick production [20]. Specimen forming was carried out using the semi-dry pressing method with a hydraulic press, PSU-10 (Tehmash LLC, Chelyabinsk, Russia). At the first stage of the experiment, cylindrical specimens with dimensions of 50×50 mm were produced at a compaction pressure of 10 MPa (Figure 1). At this stage, the influence of different particle size fractions and glass powder content was investigated.

Figure 1 – Formed specimens

At the second stage, the compaction pressure was varied in the range of 5-15 MPa for the optimal fraction and content of glass powder to assess the combined effect of particle dispersity and degree of compaction on the material properties. The incorporation of glass components into silicate materials and variations in forming parameters significantly affect the formation of calcium hydrosilicate structures and the physical-mechanical properties of autoclaved products [6].

2.4 Autoclave treatment

The formed specimens were subjected to autoclave treatment under conditions corresponding to the industrial technology of silicate brick production (Figure 2). The treatment was carried out in an autoclave (Chemical Equipment and Industrial Fittings Plant, Kielce, Poland). The autoclaving regime corresponded to the technological mode applied at the silicate brick plant in Uralsk: temperature increase to 174-175 °C over 1.5-2 hours, followed by isothermal holding at 174-175 °C and a saturated steam pressure of approximately 0.8 MPa for 6-8 hours. This was followed by gradual pressure reduction and cooling to atmospheric conditions over 2 hours.

a) Autoclaving b) Cooling

Figure 2 – Treatment of specimens

After completion of the autoclave treatment, the specimens were cooled and conditioned under laboratory conditions until stable temperature and mass values were achieved.

2.5 Physical-mechanical testing

The average density, water absorption, and compressive strength (Figure 3) were determined in accordance with the requirements of the regulatory documents [21], [22] in force in the Republic of Kazakhstan, which govern testing methods for silicate brick and autoclaved silicate products. Compressive strength tests were carried out on cylindrical specimens with dimensions of Ø50×50 mm. The reported strength values were taken as the average results obtained from a series of tests.

Figure 3 – Compression test of specimens

Frost resistance of the specimens was evaluated using a method of repeated freeze-thaw cycles in accordance with national regulatory requirements for silicate products [21]. Freezing of the specimens was performed in a laboratory freezing chamber of the XR series (YUKON, Moscow, Russian Federation).

2.6 Determination of thermal conductivity

The thermal conductivity was determined on specimens that were preliminarily dried to constant mass. Measurements were carried out using an ITP-MG4 device (Stroypribor LLC, Chelyabinsk, Russia) based on the probe method. The tests were performed on prepared specimens using the transient heat flow method. Measurements were conducted at room temperature. For each composition, at least three measurements were performed, and the average value of the thermal conductivity coefficient was calculated based on the obtained results.

3. Results and Discussion

3.1 Effect of particle size distribution and glass powder content

Table 1 and Figure 4 present the physical, mechanical, and thermophysical properties of silicate brick produced in different fractions and contents of finely ground glass powder.

Table 1 – Effect of glass powder particle size distribution and content on the properties of silicate brick (applied compaction pressure of 10 MPa)

Fraction, μm	Glass content, %	Average density, kg/m^3	Average compressive strength, MPa	Average water absorption, %	Average thermal conductivity, W/(m·°C)	Frost resistance, F
	0*	1850	14.2	14.7	0.87	
≤63	5	1820	13.4	12.6	0.80	
	10	1860	14.5	11.3	0.77	
	15	1835	13.8	11.9	0.78	
63-140	5	1795	12.4	13.4	0.81	
	10	1825	13.4	12.0	0.79	
	15	1810	13.0	12.6	0.80	F50
140-315	5	1785	12.0	13.9	0.82	
	10	1795	12.3	13.5	0.81	
	15	1780	12.1	13.8	0.82	
315-630	5	1765	11.6	14.3	0.83	
	10	1770	11.6	14.0	0.83	
	15	1760	11.4	14.5	0.84	

* Reference specimen.

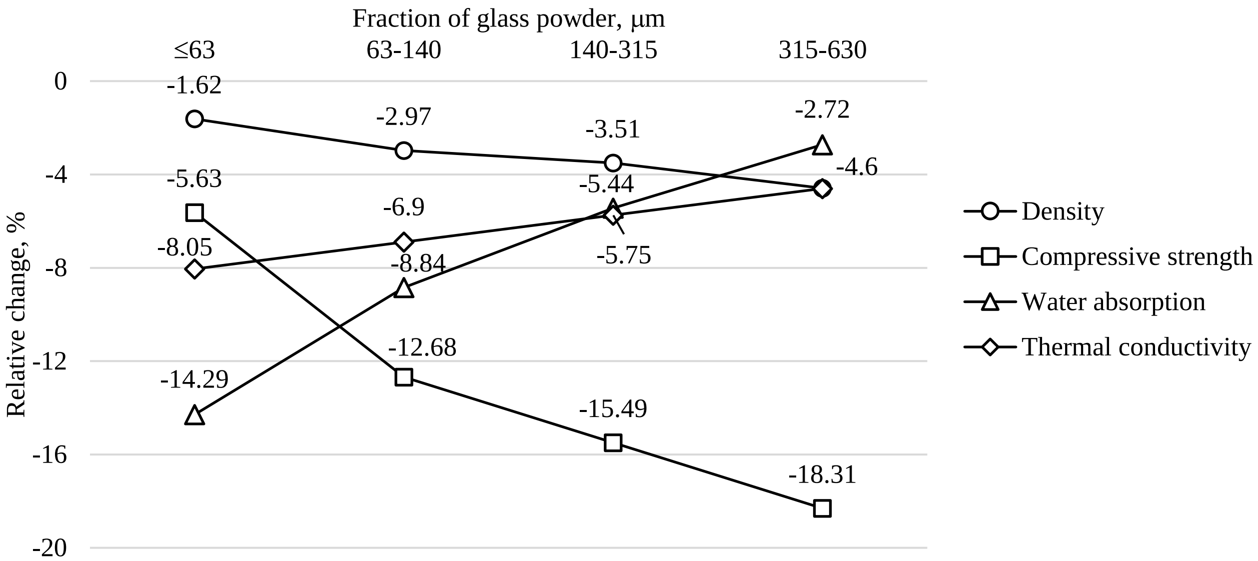

a) Glass content of 5 %

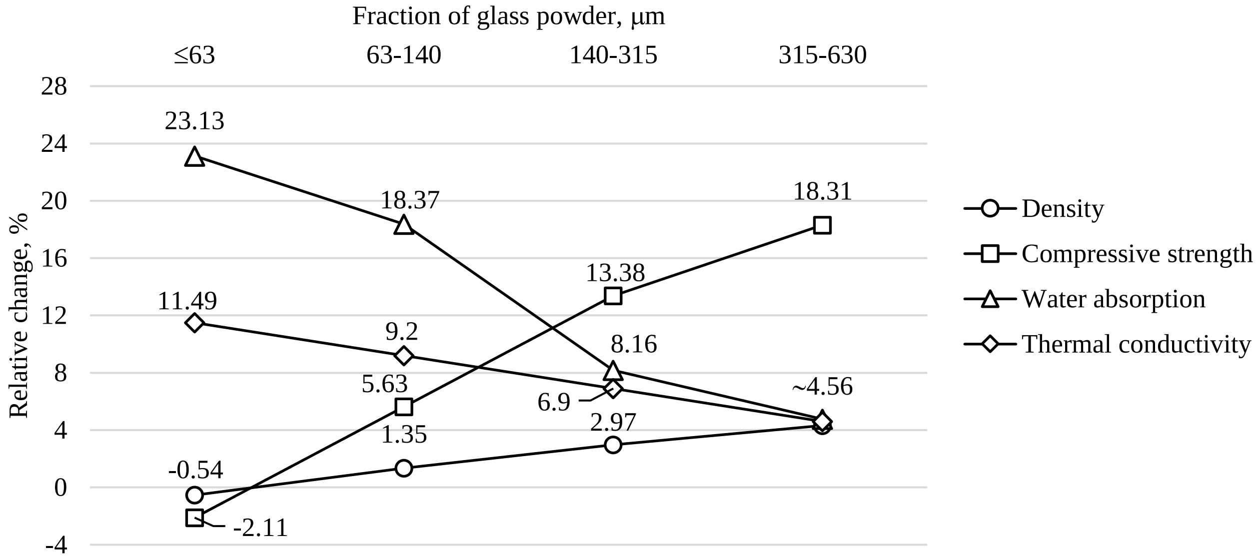

b) Glass content of 10%

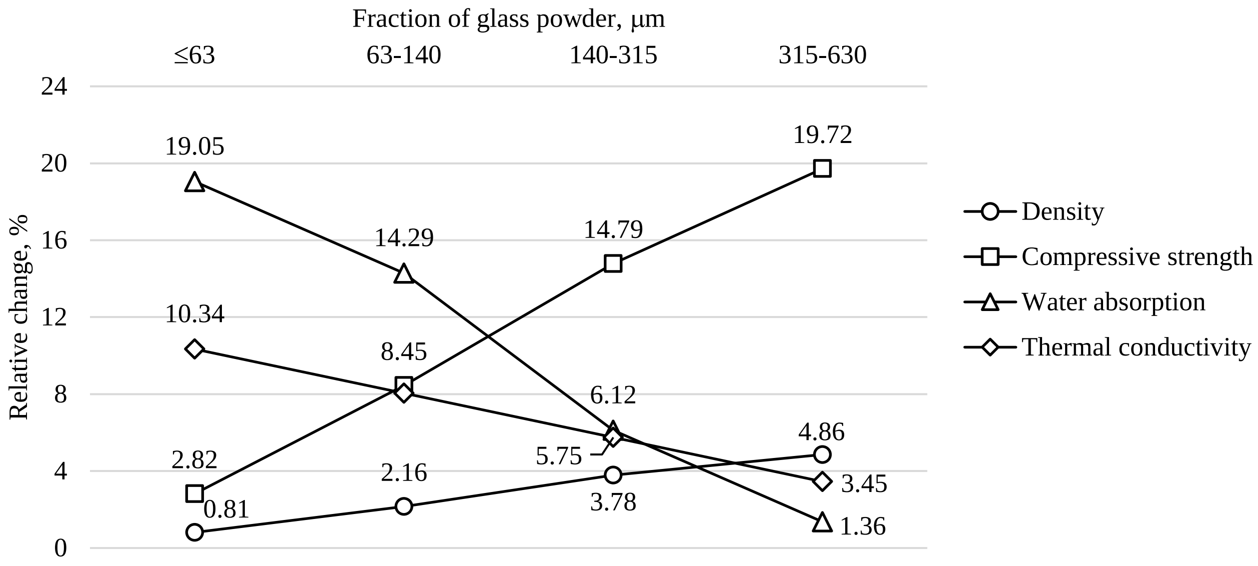

c) Glass content of 15%

Figure 4 – Relative change in the properties of silicate brick compared to the reference specimen

Table 1 and Figure 4 jointly show that the effect of glass powder on silicate brick is controlled by both particle size distribution and content, with the finest fraction giving the best overall results. The clearest positive effect is observed for the ≤63 μm fraction at 10% addition, where the average density increases from 1850 to 1860 kg/m^3, compressive strength from 14.2 to 14.5 MPa, while water absorption decreases from 14.7 to 11.3% and thermal conductivity from 0.87 to 0.77 W/(m·°C). Figure 4 confirms this as the most favorable combination, corresponding to +0.54% in density, +2.11% in compressive strength, −23.13% in water absorption, and −11.49% in thermal conductivity relative to the reference specimen. A similar positive effect of glass incorporation in autoclaved sand-lime systems was reported by [2] and [3], who showed that glass-containing autoclaved materials can exhibit improved strength and reduced water uptake due to favorable hydrothermal structure formation.

At the same time, Table 1 and Figure 4 show that increasing the content of the same fine fraction from 10% to 15% weakens the positive effect: density falls to 1835 kg/m^3, compressive strength to 13.8 MPa, and the relative change in strength becomes negative (−2.82%). Although water absorption (11.9%) and thermal conductivity (0.78 W/(m·°C)) remain better than in the reference specimen, the overall performance is lower than at 10%, suggesting that excessive glass powder reduces structural uniformity. The presence of an optimum additive content rather than a monotonic improvement is consistent with the results of [9], who also found that moderate waste addition in autoclaved brick was more beneficial than higher dosages.

For the 63-140 μm fraction, the values in Table 1 remain less favorable than for the finest powder, although some improvement is still observed. At 10% glass content, density reaches 1825 kg/m^3, compressive strength 13.4 MPa, water absorption 12.0%, and thermal conductivity 0.79 W/(m·°C). Figure 4 shows that these changes are moderate: density is still 1.35% below the reference and compressive strength 5.63% lower, even though water absorption and thermal conductivity decrease by 18.37% and 9.20%, respectively. This suggests that with increasing particle size, glass powder remains beneficial mainly for physical and thermophysical properties, while its strengthening effect becomes weaker. This weaker strengthening effect with increasing glass particle size agrees with the general trend reported by [12], who showed that waste-glass particle size strongly controls density, strength, and absorption behavior in brick materials.

For the 140-315 μm fraction, Table 1 shows only limited variation with glass content: density remains within 1780-1795 kg/m^3, compressive strength within 12.0-12.3 MPa, water absorption within 13.5-13.9%, and thermal conductivity within 0.81-0.82 W/(m·°C). Figure 4 likewise shows that all relative changes remain modest and compressive strength stays below the reference level at all dosages. Thus, this fraction has only a weak modifying effect. The limited modification effect observed here is also comparable to the pore-structure study of [7], where the performance of autoclaved glass-modified materials was closely linked to how effectively the additive altered the porous structure.

The 315-630 μm fraction gives the least favorable results. According to Table 1, density decreases to 1760-1770 kg/m^3, compressive strength to 11.4-11.6 MPa, while water absorption rises to 14.0-14.5% and thermal conductivity to 0.83-0.84 W/(m·°C). Figure 4 confirms the negative trend, especially for compressive strength, which decreases by 18.31-19.72% relative to the reference specimen. Thus, the unfavorable behavior of the coarsest fraction further supports the conclusion that glass in autoclaved silicate systems is most effective in a sufficiently fine state, as also indicated in studies of glass-based autoclaved materials [2], [3].

Overall, Table 1 provides the absolute values, while Figure 4 clearly highlights the relative trends: the beneficial effect of glass powder is strongest for the finest fraction and reaches an optimum at 10% content. As particle size increases, the improvement becomes progressively weaker, and for the coarsest fraction, the effect becomes unfavorable.

3.2 Frost resistance

Despite differences in physical and mechanical properties, all investigated specimens demonstrated frost resistance at the level of F50.

3.3 Effect of compaction pressure

Figure 5 illustrates the effect of compaction pressure on the properties of silicate brick produced using the optimal glass powder fraction (≤63 μm) at a content of 10%.

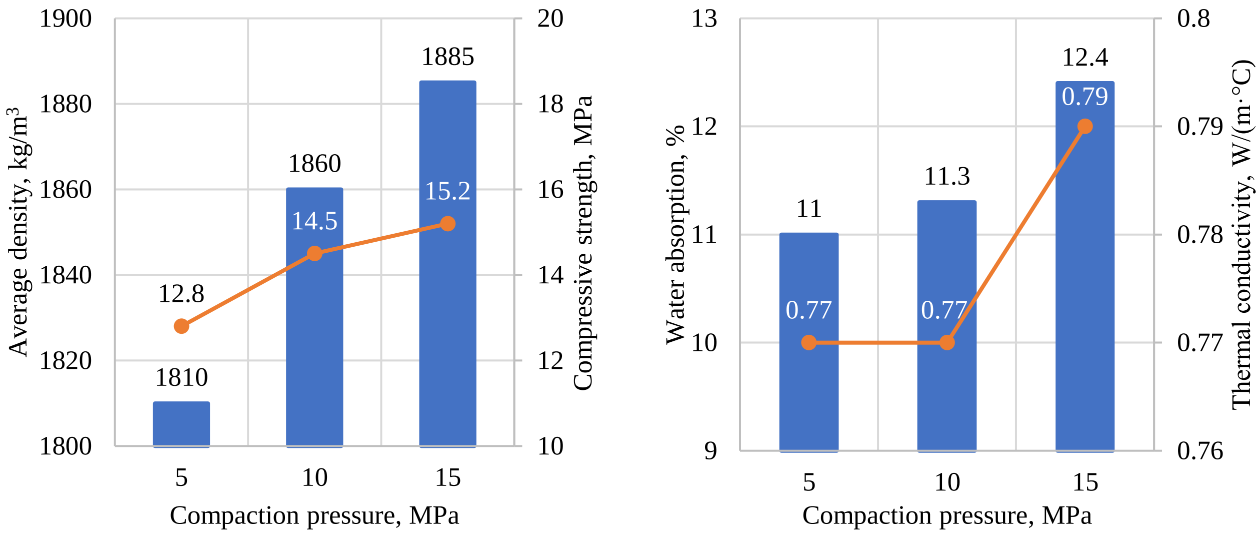

a) Physical-mechanical properties b) Hydro-thermal properties

Figure 5 – Effect of applied compaction pressure on the properties of silicate brick

The results show that increasing the compaction pressure from 5 to 15 MPa leads to an increase in the average density of the material from 1810 to 1885 kg/m^3, and in compressive strength from 12.8 to 15.2 MPa. An increase in compaction pressure promotes the reduction of intergranular voids and results in denser particle packing, leading to the formation of a more compact silicate matrix. At the same time, water absorption decreases from 12.4 to 11.0%, indicating a reduction in the volume of open pores within the material structure. The thermal conductivity coefficient varies within the range of 0.77-0.79 W/(m·°C), which indicates a minor influence of compaction pressure on the thermophysical properties of the material. The observed increase in density and compressive strength, together with lower water absorption at higher compaction pressure, is consistent with the behavior of other autoclaved lime-based bricks, where denser packing and more favorable structure formation improved the main performance characteristics [1].

3.5. Limitations of the study and prospects for future research

Despite the obtained results, certain limitations of the present study should be noted. The work considered a limited range of glass powder particle size distributions and compaction pressure. In future research, it is advisable to expand the range of dispersity parameters investigated, as well as to conduct a more detailed microstructural analysis using SEM and XRD methods in order to achieve a deeper understanding of the structure formation mechanisms in modified silicate systems.

4. Conclusion

This study established that the performance of autoclaved silicate brick modified with glass powder depends on the combined influence of particle size distribution, additive content, and compaction pressure. Among the investigated fractions, the finest glass powder (≤63 μm) showed the highest modification efficiency. At a content of 10 wt.% and a compaction pressure of 10 MPa, the material exhibited the most balanced set of properties, reaching an average density of 1860 kg/m^3, compressive strength of 14.5 MPa, water absorption of 11.3%, and thermal conductivity of 0.77 W/(m·°C). These results indicate that finely ground glass powder contributes to the densification of the silicate matrix and improvement of both mechanical and thermophysical performance.

An increase in glass powder content from 10 to 15 wt.% did not provide further overall improvement, which indicates the presence of an optimum dosage. In addition, as the particle size of the glass powder increased from ≤63 μm to coarser fractions, the positive effect became progressively weaker, and for the 315-630 μm fraction, the modification efficiency was unfavorable relative to the reference composition. This confirms that the reactivity and modifying effect of glass powder in silicate systems are strongly controlled by dispersity.

The variation of compaction pressure for the optimal composition showed that increasing pressure from 5 to 15 MPa led to an increase in density from 1810 to 1885 kg/m^3 and compressive strength from 12.8 to 15.2 MPa, while water absorption decreased from 12.4 to 11.0%. At the same time, thermal conductivity remained within a narrow range of 0.77-0.79 W/(m·°C), indicating that compaction pressure had a stronger effect on physical-mechanical properties than on thermophysical behavior.

For all investigated compositions, frost resistance remained at the level of F50, which confirms that the incorporation of glass powder within the studied range did not reduce the frost durability of the silicate brick. Overall, the use of glass powder with a particle size ≤63 μm at a content of 10 wt.% can be regarded as the most effective solution among the studied variants, and the results confirm the practical potential of recycling glass waste in the production of silicate brick with improved performance characteristics.

Acknowledgments

This research was funded by the Science Committee of the Ministry of Science and Higher Education of the Republic of Kazakhstan (Grant No. BR24993125 – “Rational Technology for the Utilization of Glass Waste in the Production of Silicate Brick to Improve the Thermal Insulation Properties of Enclosing Structures during the Reconstruction of Housing and Public Utilities Facilities”).

References

[1] T. Cicek and M. Tanrıverdi, “Lime based steam autoclaved fly ash bricks,” *Construction and Building Materials*, vol. 21, no. 6, pp. 1295–1300, Jun. 2007, doi: 10.1016/j.conbuildmat.2006.01.005.

[2] A. Stepien, M. Leśniak, and M. Sitarz, "A Sustainable Autoclaved Material Made of Glass Sand," *Buildings*, vol. 9, no. 11, p. 232, Nov. 2019, doi: 10.3390/buildings9110232.
[3] A. Stepien, B. Potrzeszcz-Sut, D. P. Prentice, T. J. Oey, and M. Balonis, "The Role of Glass Compounds in Autoclaved Bricks," *Buildings*, vol. 10, no. 3, p. 41, Feb. 2020, doi: 10.3390/buildings10030041.
[4] C. Shi, Y. Wu, C. Riefler, and H. Wang, "Characteristics and pozzolanic reactivity of glass powders," *Cement and Concrete Research*, vol. 35, no. 5, pp. 987–993, May 2005, doi: 10.1016/j.cemconres.2004.05.015.
[5] K. Zheng, "Pozzolanic reaction of glass powder and its role in controlling alkali–silica reaction," *Cement and Concrete Composites*, vol. 67, pp. 30–38, Mar. 2016, doi: 10.1016/j.cemconcomp.2015.12.008.
[6] K. Borek and P. Czapik, "Utilization of Waste Glass in Autoclaved Silica–Lime Materials," *Materials*, vol. 15, no. 2, p. 549, Jan. 2022, doi: 10.3390/ma15020549.
[7] A. Stepien, "Analysis of Porous Structure in Autoclaved Materials Modified by Glass Sand," *Crystals*, vol. 11, no. 4, p. 408, Apr. 2021, doi: 10.3390/cryst11040408.
[8] I. Jasińska, R. Dachowski, and M. Jaworska-Wędzińska, "Thermal Conductivity of Sand-Lime Products Modified with Foam Glass Granulate," *Materials*, vol. 14, no. 19, p. 5678, Sep. 2021, doi: 10.3390/ma14195678.
[9] P. Kostrzewa-Demczuk, A. Stepien, R. Dachowski, and A. Krugiełka, "The use of basalt powder in autoclaved brick as a method of production waste management," *Journal of Cleaner Production*, vol. 320, p. 128900, Oct. 2021, doi: 10.1016/j.jclepro.2021.128900.
[10] P. Kostrzewa-Demczuk, A. Stepien, R. Dachowski, and R. B. D. Silva, "Influence of Waste Basalt Powder Addition on the Microstructure and Mechanical Properties of Autoclave Brick," *Materials*, vol. 16, no. 2, p. 870, Jan. 2023, doi: 10.3390/ma16020870.
[11] R. B. Da Silva, A. Matoski, A. Neves Junior, and P. Kostrzewa-Demczuk, "Study of compressive strength of sand-lime bricks produced with coal tailings using mixture design," *Construction and Building Materials*, vol. 344, p. 127986, Aug. 2022, doi: 10.1016/j.conbuildmat.2022.127986.
[12] L. Mao, H. Zhou, M. Peng, L. Hu, and W. Zhang, "Effects of waste glass particle size on improving the property and environmental safety of fired brick containing electroplating sludge," *Construction and Building Materials*, vol. 257, p. 119583, Oct. 2020, doi: 10.1016/j.conbuildmat.2020.119583.
[13] Md. R. Hasan, A. Siddika, Md. P. A. Akanda, and Md. R. Islam, "Effects of waste glass addition on the physical and mechanical properties of brick," *Innov. Infrastruct. Solut.*, vol. 6, no. 1, p. 36, Mar. 2021, doi: 10.1007/s41062-020-00401-z.
[14] M. Tripathi and V. B. Chauhan, "Evaluation of waste glass powder to replace the clay in fired brick manufacturing as a construction material," *Innov. Infrastruct. Solut.*, vol. 6, no. 3, p. 134, Sep. 2021, doi: 10.1007/s41062-021-00492-2.
[15] S. M. S. Kazmi, M. J. Munir, Y.-F. Wu, A. Hanif, and I. Patnaikuni, "Thermal performance evaluation of eco-friendly bricks incorporating waste glass sludge," *Journal of Cleaner Production*, vol. 172, pp. 1867–1880, Jan. 2018, doi: 10.1016/j.jclepro.2017.11.255.
[16] T.-C. Ling, K. H. Mo, L. Qu, J. Yang, and L. Guo, "Mechanical strength and durability performance of autoclaved lime-saline soil brick," *Construction and Building Materials*, vol. 146, pp. 403–409, Aug. 2017, doi: 10.1016/j.conbuildmat.2017.04.106.
[17] "EN 771-2:2011+A1:2015 Specification for masonry units - Part 2: Calcium silicate masonry units," Brussels, Belgium: CEN, 2015, p. 45.
[18] "GOST 8736-2014 Sand for construction works. Specifications," Moscow, Russia: Standardinform, 2014, p. 8.
[19] "GOST 379-2015 Silicate bricks, stones, blocks and partition blocks. General specifications," Moscow, Russia: Standardinform, 2015, p. 19.
[20] L. Ilina, L. Tatski, and L. Baryshok, "Quality Improvement of semi-dry pressing ceramic bricks from low-quality raw materials by the directional additives," *IOP Conf. Ser.: Mater. Sci. Eng.*, vol. 962, no. 2, p. 022007, Nov. 2020, doi: 10.1088/1757-899X/962/2/022007.
[21] "GOST 7025-91 Ceramic and calcium silicate bricks and stones. Methods for water absorption and density determination and frost resistance control," Moscow, Russia: Standardinform, 2006, p. 10.
[22] "GOST 8462-85 Wall materials. Methods for determination of ultimate compressive and bending strength," Moscow, Russia: Standardinform, 1985, p. 6.

Information about authors:

Sarsenbek Montayev – Doctor of Technical Sciences, Professor, Head, Research Laboratory of Construction Materials and Technologies, West Kazakhstan Agrarian and Technical University named after Zhangir Khan, Uralsk, Republic of Kazakhstan, montaevs@mail.ru

Bolatbek Sakhiev – PhD Student, Research Laboratory of Construction Materials and Technologies, West Kazakhstan Agrarian and Technical University named after Zhangir Khan, Uralsk, Republic of Kazakhstan, bolatbeksahiev5@gmail.com

Sabit Zharylgapov – PhD, Associate Professor, Research Laboratory of Construction Materials and Technologies, West Kazakhstan Agrarian and Technical University named after Zhangir Khan, Uralsk, Republic of Kazakhstan, sabit.raisa@mail.ru
Ainur Montayeva – PhD, Senior Lecturer, Department of Architecture and Construction, Korkyt Ata Kyzylorda University, Kyzylorda, Republic of Kazakhstan, asmontay@gmail.com

Author Contributions:
Sarsenbek Montayev – concept, analysis, resources, funding acquisition.
Bolatbek Sakhiev – data collection, interpretation, drafting.
Sabit Zharylgapov – methodology, editing.
Ainur Montayeva – testing, modeling, visualization.

Conflict of Interest: The authors declare no conflict of interest.

Use of Artificial Intelligence (AI): Disclose the use of AI in the preparation of the article.

Received: 17.01.2026
Revised: 17.03.2026
Accepted: 25.03.2026
Published: 27.03.2026

Technobius, 2026, 6(1), 0099, DOI: https://doi.org/10.54355/tbus/6.1.2026.0099

Technobius
https://technobius.kz/

e-ISSN
2789-7338

Article

Effect of waste glass and silica fume additions on the properties of fired clay ceramics

Zhanar Zhumadilova[1], Maratbek Zhuginissov[1], Ruslan Nurlybayev[2], Yelzhan Orynbekov[1], Aigerim Tolegenova[1,*], Adlet Zhagifarov[1]

[1]Institute of Architecture and Civil Engineering named after T.K. Bassenov, Satbayev University, Almaty 050013, Republic of Kazakhstan
[2]Institute of Mining and Metallurgy, Satbayev University, Almaty 050013, Republic of Kazakhstan
*Correspondence: a.tolegenova@satbayev.university

Abstract. This study investigates the influence of crushed waste glass (GL) and silica fume (SF) on the densification and microstructural characteristics of fired clay ceramics. Ceramic specimens were prepared by partially replacing clay with 10, 15, and 20 wt.% of GL and SF. They fired at 1050, 1100, and 1125 °C to evaluate the effect of temperature on bulk density and to determine the optimal firing regime. Based on density measurements and visual examination, the samples fired at 1125 °C were identified as the most effective and selected for further evaluation. Water absorption testing and microstructural characterization were conducted for specimens fired at 1125 °C. Increasing firing temperature enhanced densification for all compositions. Glass-modified ceramics exhibited the highest bulk density and lowest water absorption due to intensified liquid-phase sintering and pore filling. In contrast, silica fume additions resulted in comparatively higher porosity and water absorption under identical conditions. Microstructural analysis confirmed a denser and more homogeneous matrix in glass-containing specimens with uniformly distributed Si-, Al-, and Ca-rich phases. The results demonstrate that both additives can modify the properties of fired clay ceramics; however, crushed glass provides a more pronounced improvement in densification and water resistance at 1125 °C.
Keywords: fired clay ceramics, crushed glass, silica fume, bulk density, firing temperature, microstructure, water absorption.

1. Introduction

Fired clay ceramic materials, such as ceramic bricks, tiles, and construction ceramic products, are manufactured by shaping clay raw materials followed by high-temperature firing. During firing, sintering, and vitrification (glass formation) occur, which determine the final bulk density, porosity, and water absorption (key parameters governing the durability and service performance of ceramic products) [1], [2]. As a rule, increasing the firing temperature in the range of 900-1150 °C leads to higher density and reduced open porosity; however, it is accompanied by increased energy consumption and production costs [3], [4]. Therefore, the development of compositions that enable control of sintering and structure formation through mineral additives, including those derived from industrial waste, is of particular importance.

A promising approach involves the use of silica-rich waste, particularly silica fume, which is a highly dispersed amorphous silicon dioxide with a typical particle size of less than 1 μm, capable of influencing the sintering kinetics and phase formation during firing [5]. Incorporation of silica fume in amounts up to 10 wt.% has been shown to increase the strength and density of fired bricks at temperatures of 1000-1100 °C, whereas at lower firing temperatures a tendency toward reduced density is observed [6]. In several studies, silica fume has also been investigated as part of complex waste-containing systems with a total waste content of up to 90 wt.%, highlighting its technological potential while simultaneously indicating a strong sensitivity of properties to firing temperature [7].

In parallel with silica fume, waste glass has been extensively studied as an additive for clay ceramics. Waste glass has been demonstrated to act as a flux, forming a liquid phase and intensifying liquid phase sintering at temperatures as low as 900-1000 °C, thus promoting structural densification and reducing porosity [8]. Experimental studies confirm that the incorporation of glass waste at levels of 5-10 wt.% leads to increased density and strength and reduced water absorption of fired clay bricks; moreover, at 900 °C, properties comparable to those of reference samples fired at 1000 °C can be achieved [9].

The properties of ceramic materials are influenced not only by composition and additive type but also by firing conditions, including temperature and furnace atmosphere [10]. Variations in firing conditions (oxidization or reduction atmosphere) at temperatures of approximately 1100-1170 °C have been established to significantly alter the phase composition and physical and mechanical properties of ceramic products, including increases in density and strength of 10-20% [11]. Related studies also indicate that glass waste retains a positive influence on the properties of cementitious and mineral materials under thermal exposure up to 600 °C, confirming its stability at elevated temperatures [12].

Several studies demonstrated the feasibility of using silica fume not only in clay-based ceramics but also in specialized high-temperature ceramic systems. For example, effective recycling of silica fume waste in the synthesis of β-eucryptite ceramics with the formation of a stable crystalline structure at 1000 °C has been reported, confirming its high reactivity during firing [13].

For clay ceramics, a more consistent positive effect has been observed with the use of waste glass. Increased glass content has been shown to be 30-40 wt.%, and raising the firing temperature to 1100 °C results in higher density and strength and a reduction in water absorption to levels below 6%, with glass particle size playing a decisive role [14]. Similar conclusions were obtained when waste glass was used in combination with sedimentary materials, where a sintering temperature of 1050 °C or higher was identified as the key factor controlling structural densification [15].

In a broader context of waste recycling in brick production, it is emphasized that the use of secondary raw materials can reduce the consumption of natural resources and energy demand [16]. However, large-scale industrial implementation remains limited, despite the strength values achieved of 15-20 MPa and water absorption below 10% [17]. Reviews of waste glass recycling practices in clay bricks also highlight the need to optimize compositions and firing regimes to ensure stable and reproducible properties [18]. At the same time, studies focusing on the combined use of silica fume with other mineral wastes indicate that brick properties are largely governed by firing temperature in the range of 700-800 °C, whereas the influence of additives may be secondary compared to the temperature factor [19].

Despite the substantial body of research on the use of industrial wastes in clay ceramics, existing studies mainly address either waste glass or silica fume individually, or as components of complex multi-waste systems. Moreover, organic and inorganic additives exert different effects on porosity (increases of up to 30-35%) and mechanical properties, underscoring the need for a clear differentiation of their roles in structure formation processes [20]. In addition, the influence of waste glass on the durability and transport properties of ceramic products, including water permeability and frost resistance, requires further systematization [21].

Considering the identified trends, it can be hypothesized that silica fume and waste glass modify the sintering behavior of clay ceramics through different mechanisms. Due to its high dispersity, silica fume exhibits pronounced temperature sensitivity and can enhance densification or increase porosity depending on firing regime [22]. In contrast, waste glass at elevated temperatures is expected to provide more stable liquid-phase sintering and pore filling, which can result in reduced water absorption and increased bulk density [23].

The objective of this study is to systematically evaluate the effects of silica fume and waste glass as partial replacements of clay at levels of 10, 15, and 20 wt.% on the densification behavior and microstructural evolution of fired clay ceramics. The specimens were fired at temperatures of 1050, 1100, and 1125 °C to assess the influence of firing temperature on bulk density and to identify a rational firing regime. Based on density results, 1125 °C was selected for detailed analysis of water absorption and microstructure using scanning electron microscopy (SEM) and energy-dispersive X-ray spectroscopy (EDS) techniques. The investigated ceramics are intended for structural and non-structural clay bricks for masonry applications, including load-bearing and facade units where controlled density and reduced water absorption are required. The scientific novelty of this work lies in the direct comparison of two widely available silica-rich wastes under identical dosages and firing conditions, enabling the establishment of microstructure-property relationships governing densification and water resistance of fired clay ceramics and expanding the potential for resource-efficient ceramic production [24].

2. Methods

2.1. Raw materials

For this study, clay obtained from the Almaty deposit (Burunday district, Almaty, Kazakhstan) served as the primary raw material. The clay is characterized by a plasticity index of 9.0, which corresponds to low plasticity, and is classified as an easy-to-melt material based on its refractoriness. According to its technological characteristics, the clay is appropriate for the production of frost-resistant ceramic bricks of grades M100 and M125 by plastic molding, in accordance with the standard requirements [25]. According to X-ray diffraction analysis, clay is a polymineral material dominated by quartz, with the presence of calcite and feldspar (plagioclase). The mineral assemblage also includes phyllosilicate phases such as mica (phlogopite) and chlorite, along with minor amounts of dolomite. The chemical composition is characterized by a predominance of SiO_2 (approximately 55-60 wt.%) and Al_2O_3 (about 15-18 wt.%), with minor contents of CaO, MgO, and Fe_2O_3, as well as Na_2O (1.88 wt.%) and SO_3 (0.74 wt.%). The loss on ignition is about 10.02%, indicating the presence of bound water and carbonate components.

As mineral additives, crushed glass (GL) and silica fume (SF) were used in combination with the clay raw material. The silica fume was supplied by “Qazaq Innotec” LLP (Almaty, Kazakhstan) and is a highly dispersed by-product of ferroalloy production, characterized by high pozzolanic activity. Due to its fine particle size, silica fume was used as a microfiller and reactive additive to improve the packing density and microstructural homogeneity of clay-based mixtures [26]. Silica fume consisted of ultrafine spherical particles (<1 μm), while crushed glass particles were irregular in shape.

Crushed glass was obtained from recycled construction and demolition glass waste (Almaty, Kazakhstan). Before using, the glass waste was ground in a planetary ball mill (XQM-4, Changsha Tianchuang Powder Technology Co., Ltd., Changsha, China) to obtain a fine powder. No additional chemical or mineralogical analysis was conducted for the crushed glass; its role was limited to that of a finely dispersed silica additive introduced into the clay matrix. Both additives were mixed with clay in doses of 10, 15, and 20 wt.% relative to the clay mass.

2.2 Preparation of ceramic specimens

Before specimen preparation, the clay was dried in a drying oven SHS 80-01 SPU (SHS 80-01 SPU, Smolensk SKTB SPU, Smolensk, Russia) at 105-110 °C, ground, and sieved through a 1 mm mesh. Silica fume and crushed glass were additionally milled until all particles passed through a 0.315 mm sieve. Two types of ceramic compositions were investigated.

After the required proportions (10, 15, and 20 wt.% relative to the clay mass) were weighed, the raw materials were first homogenized in a dry state. Subsequently, water was gradually added until a plastic and moldable mass was obtained. Cylindrical specimens with a diameter of 50 mm and a height of 55 mm were produced for further testing. The specimens were formed using a hydraulic press PGM-100MG4A (SKB Stroypribor, Chelyabinsk, Russia) under a compaction load of 6-10 kN.

The formed samples were dried in an SHS 80-01 SPU drying oven at 105-110 °C for 2 h, after which their mass and dimensions were recorded. Thermal treatment was carried out in an SNOL 1.6/1300 muffel furnace (SNOL ThermoLab, Utena, Lithuania) at temperatures of 1050, 1100, and

1125 °C for 1 hour under slightly oxidizing conditions, following the procedure described in [11] for fusible ceramic raw materials.

Two series of ceramic compositions were examined. The first series consisted of clay-silica fume mixtures, whereas the second series included clay-crushed glass systems. Based on preliminary experimental studies [11], [23], mineral additives were introduced at replacement levels of 10% (SF10 and GL10), 15% (SF15 and GL15), and 20% (SF20 and GL20) by weight of clay, resulting in ceramic charges containing 90/10, 85/15, and 80/20 clay-to-additive ratios, respectively. The reference specimen (C0) with 100% of clay has been prepared. For each composition, two specimens have been prepared. The proportions are selected based on previous research by the authors [11], [23].

Firing shrinkage was not determined quantitatively, as the study focused on densification and microstructural behavior. The specimens maintained geometric integrity at 1125 °C, while higher temperatures led to noticeable deformation due to excessive vitrification.

Figure 2 presents photographs of representative specimens fired at 1125 °C, corresponding to the temperature at which the maximum values of bulk density were achieved.

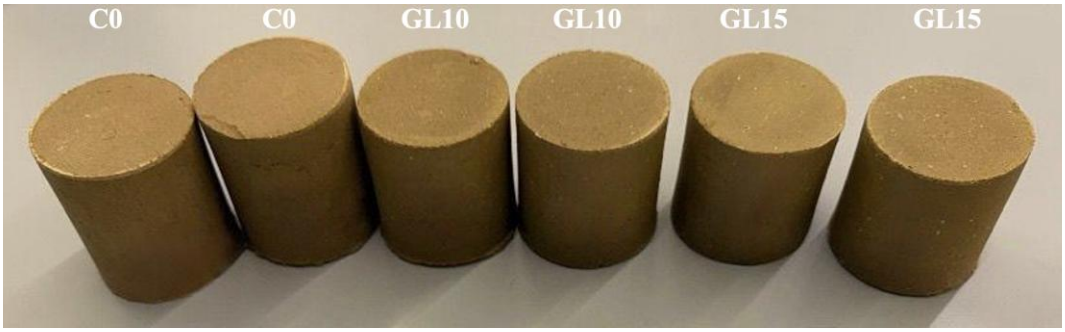

Figure 2 – Specimens with crushed glass after firing at a temperature of 1125 °C

2.2. Microstructural study

Microstructural characterization was carried out using Scanning Electron Microscopy (SEM) and Energy-Dispersive X-ray Spectroscopy (EDS). The phase composition was investigated by X-ray diffraction using a DRON-3.0 diffractometer (Bourevestnik, Saint Petersburg, Russia) equipped with CuKα radiation and a β-filter. Data were collected in θ-2θ scanning mode at an accelerating voltage of 35 kV, a current of 20 mA, and a scanning rate of 2°/min. Phase identification and semi-quantitative analysis were performed using the ICDD PDF-2 database (International Centre for Diffraction Data, Newtown Square, PA, USA). Elemental composition and microstructural features of the specimens were examined using a scanning electron microscope (JEOL JSM-7000, JEOL Ltd., Tokyo, Japan). Observations were conducted at an accelerating voltage of 10 kV, with a working distance of 14 mm, under low-vacuum conditions at ×1000 magnification.

2.3. Physical and mechanical properties

The average density of the ceramic specimens was calculated from the mass-to-volume ratio of cylindrical samples with a diameter of 50 mm and a height of 55 mm. Density values were determined in accordance with the methodology described in [23].

Water absorption was evaluated as an indicator of the degree of moisture uptake by the ceramic material after prolonged immersion in water. The test procedure followed the standard requirements [27].

3. Results and Discussion

This section presents the key experimental results on the effect of crushed waste glass and silica fume on the densification and microstructural characteristics of fired clay ceramics. The influence of additive type, replacement level, and firing temperature on bulk density, water absorption, and microstructure is analyzed with respect to ceramic materials intended for brick production. Each additive was evaluated independently to enable a direct comparison of its effects on sintering behavior and structure formation.

3.1. Effect of firing temperature on bulk density, visual appearance, and water absorption

The effect of firing temperature on the bulk density of the ceramic specimens containing silica fume and crushed glass is illustrated in Figure 1, demonstrating the pronounced influence on the compaction behavior of all investigated compositions.

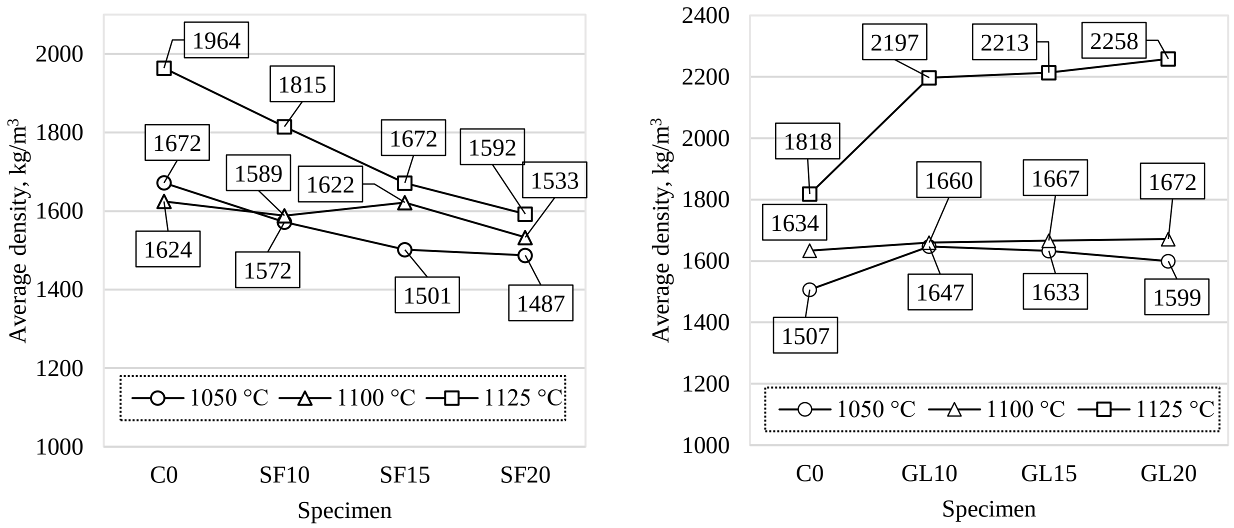

a) Silica fume (SF) b) Crushed glass (GL)

Figure 1 – Effect of firing temperature on the bulk density of ceramic specimens with SF and GL

As shown in Figure 1a, for the specimens containing silica fume (SF series), an increase in firing temperature from 1050 °C to 1125 °C led to a noticeable increase in bulk density for all additive contents. The most significant compaction was observed at 1125 °C, indicating enhanced sintering and improved consolidation of the ceramic matrix at this temperature [28]. At lower firing temperatures (1050 and 1100 °C), the density values remained comparatively lower, suggesting incomplete sintering of the ceramic body. A gradual decrease in density with an increase in the silica fume content was observed at all firing temperatures, which can be attributed to the influence of the additive on pore formation and vitrification behavior. A similar temperature-dependent trend was observed for the compositions containing crushed glass (GL series), as shown in Figure 1b. However, at 1125 °C, the highest values of bulk density among all investigated compositions were achieved for specimens with crushed glass. This pronounced compaction can be associated with the softening and partial melting of the glass phase, which promotes liquid-phase sintering and effective pore filling. In contrast, specimens fired at 1050 °C and 1100 °C exhibited reduced densification, indicating limited activation of the glass phase at lower temperatures.

The reduced bulk density observed in silica fume-modified specimens can be attributed to the ultrafine particle size and high specific surface area of silica fume [29], which increase water demand during shaping and may promote the development of a more open pore structure during firing. Similar effects of silica fume on porosity and density of clay-based ceramics have been reported in [6], [19], [22]. In contrast to crushed glass, silica fume does not contain significant amounts of fluxing oxides and therefore does not effectively promote liquid-phase sintering at the investigated temperatures [9], [14]. Consequently, densification is less pronounced compared to glass-modified compositions. The silica fume used in this study contains negligible residual carbon, and carbon burnout is not considered a governing factor affecting density [6], [13].

In general, the results confirm that 1125 °C is an effective firing temperature to achieve sufficient compaction of the ceramic compositions investigated. In particular, the specimens demonstrated the highest density values without visible deformation or structural defects. Therefore, specimens C0, GL10, and GL15 fired at 1125 °C were selected as the optimal firing temperature for subsequent water absorption measurements and microstructural characterization. A similar densification trend has been reported in previous studies on waste glass-modified clay bricks [30]. Researchers reported that the incorporation of recycled glass led to an increase in bulk density and mechanical performance due to liquid-phase sintering, particularly at elevated firing temperatures above 1000 °C. Comparable results were also observed by [31], who attributed the enhanced densification to the fluxing action of glass waste, promoting pore closure and matrix consolidation during firing. In our case, the temperatures above 1125 °C resulted in visible geometric deformation of the specimens due to excessive vitrification, suggesting that 1125 °C represents the upper practical firing limit for the investigated compositions.

Water absorption results for specimens fired at 1125 °C are shown in Figure 3.

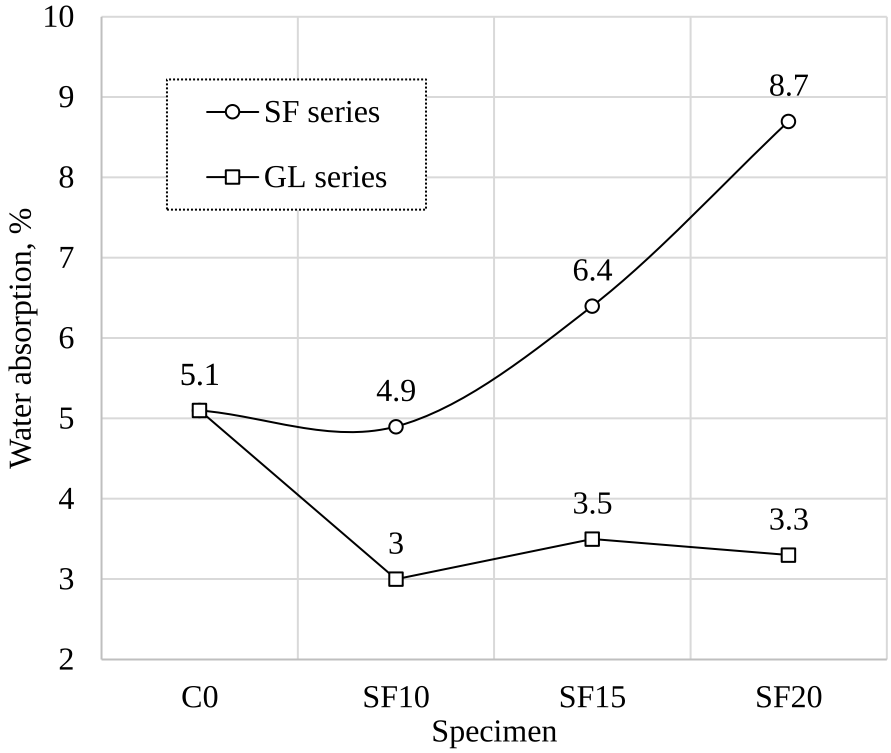

Figure 3 – Water absorption of ceramic specimens modified with SF and GL fired at 1125 °C

As shown in Figure 2, for the silica fume-modified compositions (SF series), water absorption increases with increasing additive content and exceeds 6% for SF15 and SF20, indicating the formation of a more open pore structure at higher silica fume contents. In contrast, the crushed glass-modified compositions (GL series) exhibit significantly lower water absorption compared to both the reference specimen and the SF series. The reduced water absorption of glass-containing ceramics is attributed to improved vitrification and effective pore filling during firing, resulting in improved water resistance, which is consistent with findings reported in [32], [33]. Findings [32] demonstrated that the incorporation of glass waste into clay ceramics significantly reduced water absorption due to enhanced vitrification and sealing of open pores. Similar trends were reported by [33], who showed that crushed waste glass contributes to the formation of a dense glassy phase, leading to improved water resistance of fired clay bricks.

3.2. Results of microstructural analysis using SEM and EDS

Figure 4 presents SEM micrographs of ceramic specimens fired at 1125 °C, including the reference composition and compositions containing crushed glass.

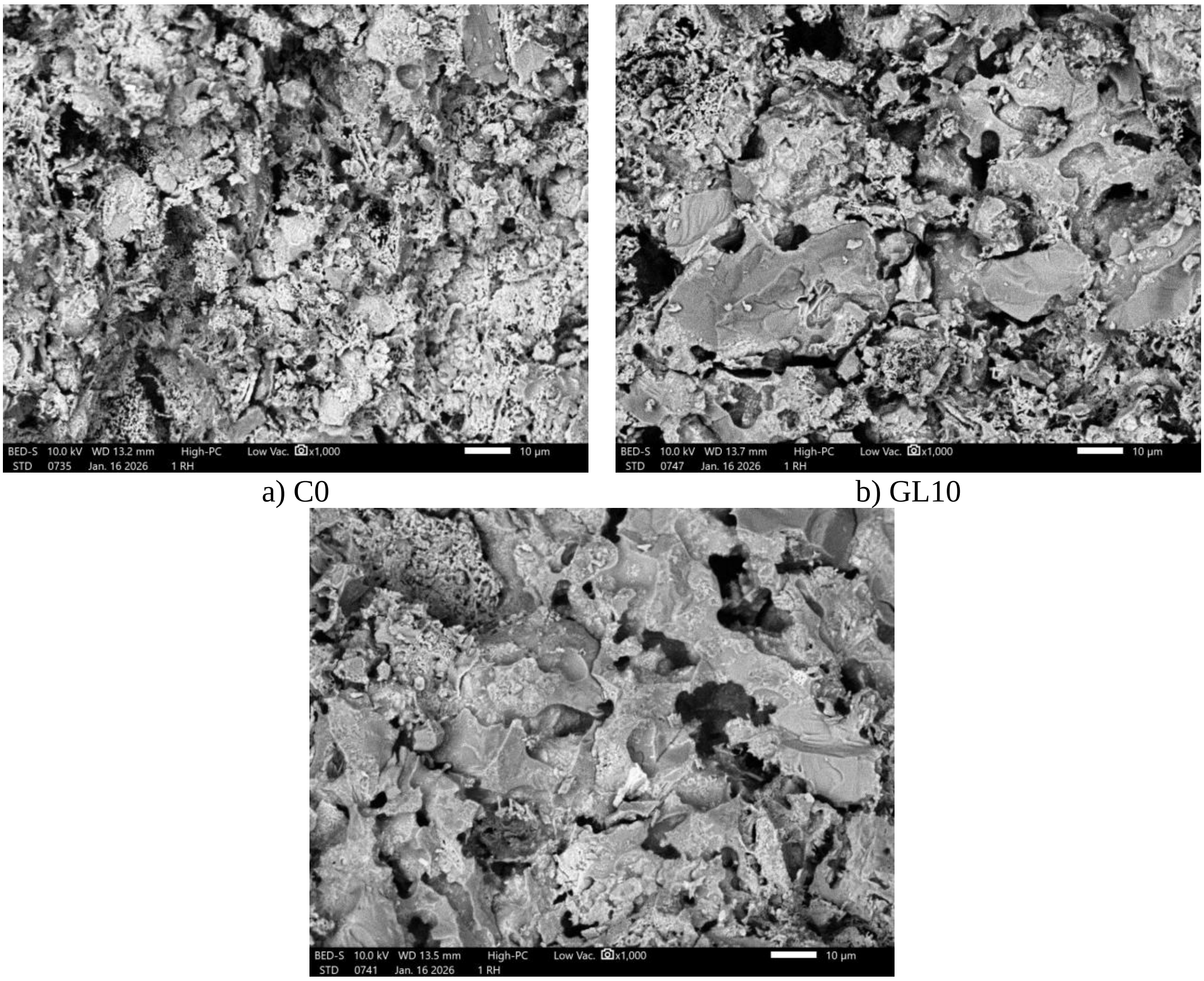

a) C0 b) GL10

c) GL15

Figure 4 – SEM micrographs of ceramic specimens fired at 1125 °C

It is seen from Figure 4a that the reference specimen (C0) exhibits a relatively heterogeneous microstructure with irregularly shaped particles and a noticeable amount of open porosity, indicating incomplete compaction of the ceramic matrix. Incorporation of 10 wt.% crushed glass (GL10) led to a more compact microstructure formation characterized by smoother particle surfaces and improved interparticle bonding, as is seen from Figure 4b. The presence of partially vitrified regions suggests the activation of liquid-phase sintering, which contributes to pore filling and enhanced matrix consolidation. Further increase in the crushed glass content to 15 wt.% (GL15) resulted in a denser and more homogeneous microstructure with reduced pore size and improved particle integration, as is seen from Figure 4c. The observed microstructural refinement is consistent with the higher bulk density values obtained for glass-containing specimens fired at 1125 °C (Figure 1b). These observations suggest the beneficial role of crushed glass in developing vitrification and compaction during high-temperature firing. Comparable microstructural features have been reported in earlier SEM investigations of glass-containing clay ceramics. Findings in [34] observed smoother particle surfaces and reduced open porosity in glass-modified bricks, which were associated with partial melting of the glass phase and enhanced interparticle bonding. Similar vitrified regions and pore-filling effects were also reported by [35] in fired ceramics produced from waste glass mixtures.

To further clarify the influence of crushed glass on the phase distribution and elemental composition of the ceramic matrix, Figure 5 shows the elemental EDS maps of the specimen containing 15 wt.% crushed glass fired at 1125 °C, as it exhibited the most favorable compaction behavior observed in Figure 4. The maps indicate a relatively uniform distribution of Si and Al throughout the ceramic matrix, confirming the formation of a continuous aluminosilicate framework.

The presence of Ca and Na is associated with the glass additive and suggests the development of a glassy phase that contributes to matrix vitrification. The corresponding EDS spectrum confirms the dominance of the Si-Al-O components with minor alkali and alkaline-earth elements, supporting the enhanced compaction observed at this firing temperature.

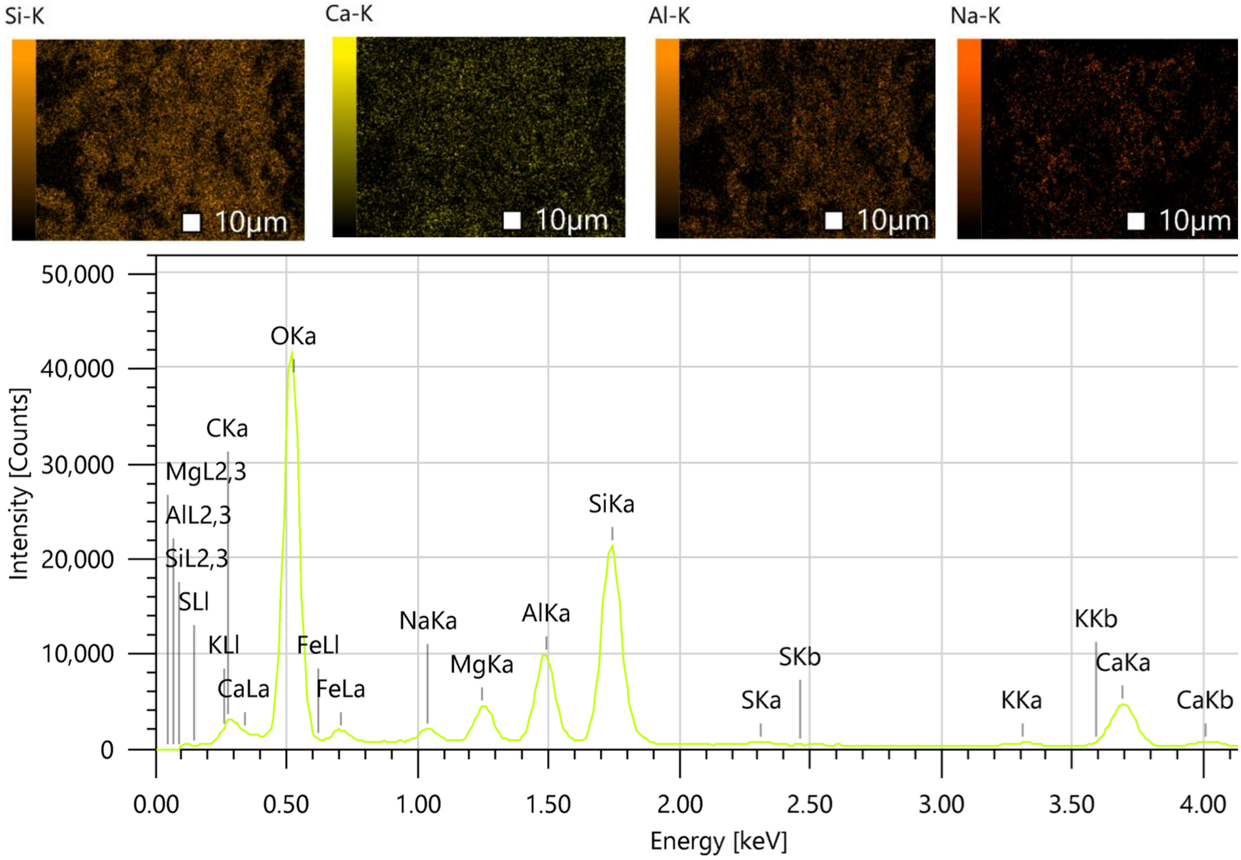

Figure 5 – EDS elemental maps and corresponding EDS spectrum of GL15 (scale bar: 10 µm)

The detected minor alkali components are consistent with the fluxing role of waste glass reported by [32], who noted that Na_2O in the glass additive promotes vitrification and contributes to denser fired clay bricks. The predominance of the Si-Al-O matrix in GL15 also agrees with the results of [34], who associated waste-glass incorporation with vitrification and glassy-phase formation in fired clay bricks. A similar glassy-phase response in glass-containing ceramics was reported by [33].

4. Conclusions

Based on the experimental results, the following conclusions can be drawn:

- Increasing the firing temperature from 1050 to 1125 °C led to a significant improvement in densification for all investigated compositions, with the highest bulk density obtained at 1125 °C, identifying this temperature as the optimal firing condition.
- The additive type strongly influenced compaction behavior. At replacement levels of 10-20 wt.%, ceramics containing crushed waste glass consistently exhibited higher bulk density than those modified with silica fume, indicating a more effective densification mechanism associated with liquid-phase sintering.
- Water absorption measurements at 1125 °C showed a clear reduction in open porosity with increasing densification. Glass-modified ceramics demonstrated the lowest water absorption, confirming the pore-filling effect of the glassy phase formed during firing.

- SEM and EDS analyses revealed that crushed glass addition produced a denser and more homogeneous ceramic matrix with reduced pore size and uniform distribution of Si-, Al-, and Ca-rich phases, explaining the enhanced compactness and reduced water absorption.

Overall, the study demonstrated that the crushed waste glass fired at 1125 °C performs as an effective mineral additive for improving the density, porosity-related properties, and microstructural characteristics of fired clay ceramics, while further research is required to assess long-term durability and industrial applicability.

Acknowledgments

This research is funded by the Committee of Science of the Ministry of Science and Higher Education of the Republic of Kazakhstan (Grant No. BR28713711 – "Development of technologies and organization of production for innovative construction materials derived from industrial mining waste and local clay raw materials").

References

[1] P. J. Sánchez-Soto, V. García-Garzón, S. Martínez-Martínez, L. Pérez-Villarejo, J. A. Sánchez-Garrido, and E. Garzón, "Influence of features and firing temperature on the ceramic properties and phase evolution of raw kaolins," *Construction and Building Materials*, vol. 466, p. 140215, Mar. 2025, doi: 10.1016/j.conbuildmat.2025.140215.

[2] P. J. Sánchez-Soto, E. Garzón, L. Pérez-Villarejo, and D. Eliche-Quesada, "Sintering behaviour of a clay containing pyrophyllite, sericite and kaolinite as ceramic raw materials: Looking for the optimum firing conditions," *Boletín de la Sociedad Española de Cerámica y Vidrio*, vol. 62, no. 1, pp. 26–39, Jan. 2023, doi: 10.1016/j.bsecv.2021.09.001.

[3] Y. Rakcho *et al.*, "Effect of firing temperature on porous ceramic properties fabricated by Moroccan red clay and oil shale," *Materials Today: Proceedings*, p. S2214785324000221, Jan. 2024, doi: 10.1016/j.matpr.2024.01.022.

[4] A. Bilgil, O. Şimşek, Ö. Sevim, and İ. Demir, "Development of lightweight and thermally efficient clay bricks using expansion additives: effects of firing temperature and additive ratios on physicomechanical properties," *J Aust Ceram Soc*, vol. 61, no. 4, pp. 1351–1363, Sep. 2025, doi: 10.1007/s41779-025-01170-7.

[5] C. Qian *et al.*, "The effect of particle size distribution on the microstructure and properties of Al2O3 ceramics formed by stereolithography," *Ceramics International*, vol. 48, no. 15, pp. 21600–21609, Aug. 2022, doi: 10.1016/j.ceramint.2022.04.133.

[6] M. S. Baspinar, I. Demir, and M. Orhan, "Utilization potential of silica fume in fired clay bricks," *Waste Manag Res*, vol. 28, no. 2, pp. 149–157, Feb. 2010, doi: 10.1177/0734242X09104385.

[7] Ç. Öztürk, "Utilization potential of borogypsum and silica fume in producing lightweight building material," *Journal of Boron*, Dec. 2022, doi: 10.30728/boron.1153669.

[8] Z. Kaliyeva, D. Mazhit, G. Satmagambetov, and K. Korniejenko, "Utilization of waste glass, ceramic scraps, and slag in manufacturing ceramic building materials," *tbus*, vol. 5, no. 4, p. 0092, Dec. 2025, doi: 10.54355/tbus/5.4.2025.0092.

[9] N. Phonphuak, S. Kanyakam, and P. Chindaprasirt, "Utilization of waste glass to enhance physical–mechanical properties of fired clay brick," *Journal of Cleaner Production*, vol. 112, pp. 3057–3062, Jan. 2016, doi: 10.1016/j.jclepro.2015.10.084.

[10] R. Hay, S. Haider, A. AlTantawi, and K. Celik, "Color modification of ceramics with controlled firing," *Ceramics International*, vol. 50, no. 1, pp. 566–574, Jan. 2024, doi: 10.1016/j.ceramint.2023.10.134.

[11] M. T. Zhuginissov, R. E. Nurlybayev, Y. S. Orynbekov, Z. O. Zhumadilova, Y. Y. Khamza, and M. Z. Bulenbayev, "The Influence of the Burning Environment on the Properties of Ceramic Products Based on Fusible Raw Materials," *Ceramics*, vol. 6, no. 2, pp. 872–885, Mar. 2023, doi: 10.3390/ceramics6020050.

[12] Z. A. Hasan, S. Q. Abdulridha, and S. Z. Abeer, "Sustainable Mortar Made with Local Clay Bricks and Glass Waste Exposed to Elevated Temperatures," *Civ Eng J*, vol. 7, no. 8, pp. 1341–1354, Aug. 2021, doi: 10.28991/cej-2021-03091729.

[13] R. M. Khattab, H. E. H. Sadek, M. A. Taha, and A. M. EL-Rafei, "Recycling of silica fume waste in the manufacture of β-eucryptite ceramics," *Materials Characterization*, vol. 171, p. 110740, Jan. 2021, doi: 10.1016/j.matchar.2020.110740.

[14] H. Abdeen and S. Shihada, "Properties of Fired Clay Bricks Mixed with Waste Glass," *JSRR*, vol. 13, no. 4, pp. 1–9, Jan. 2017, doi: 10.9734/JSRR/2017/32174.

[15] C.-W. Tang, "Properties of Fired Bricks Incorporating TFT-LCD Waste Glass Powder with Reservoir Sediments," *Sustainability*, vol. 10, no. 7, p. 2503, Jul. 2018, doi: 10.3390/su10072503.

[16] J. Fořt and R. Černý, "Transition to circular economy in the construction industry: Environmental aspects of waste brick recycling scenarios," *Waste Management*, vol. 118, pp. 510–520, Dec. 2020, doi: 10.1016/j.wasman.2020.09.004.

[17] L. Zhang, "Production of bricks from waste materials – A review," *Construction and Building Materials*, vol. 47, pp. 643–655, Oct. 2013, doi: 10.1016/j.conbuildmat.2013.05.043.

[18] Y. Xin, “Possible recycling of waste glass in sustainable fired clay bricks: A review,” *GEOMATE*, vol. 20, no. 78, Feb. 2021, doi: 10.21660/2021.78.Gx260.
[19] E. M. Abdel Hamid, “Investigation of using granite sludge waste and silica fume in clay bricks at different firing temperatures,” *HBRC Journal*, vol. 17, no. 1, pp. 123–136, Jan. 2021, doi: 10.1080/16874048.2021.1904549.
[20] N. Phonphuak, S. Lawanwadeekul, and P. Chindaprasirt, “Fired clay brick containing waste glass and agricultural waste,” in *Advances in Sustainable Masonry Bricks and Blocks*, Elsevier, 2026, pp. 263–284. doi: 10.1016/B978-0-443-40389-7.00005-9.
[21] S. E. Chidiac and L. M. Federico, “Effects of waste glass additions on the properties and durability of fired clay brickThis article is one of a selection of papers published in this Special Issue on Masonry.,” *Can. J. Civ. Eng.*, vol. 34, no. 11, pp. 1458–1466, Nov. 2007, doi: 10.1139/L07-120.
[22] M. S. Elmaghraby and A. I. M. Ismail, “Effect of Silica Fume Addition and Firing Temperature on Physico-Mechanical Properties of Clay Bricks,” *Interceram. - Int. Ceram. Rev.*, vol. 65, no. 4–5, pp. 166–172, Aug. 2016, doi: 10.1007/BF03401165.
[23] R. E. Nurlybayev, M. T. Zhuginissov, Z. O. Zhumadilova, A. A. Joldassov, Y. S. Orynbekov, and A. A. Murzagulova, “An Investigation of the Effects of Additives and Burning Temperature on the Properties of Products Based on Loam,” *Applied Sciences*, vol. 12, no. 7, p. 3352, Mar. 2022, doi: 10.3390/app12073352.
[24] A. V. Hrachanikau, Kauchur, A.S., P. I. Manak, and I. A. Tsimanov, “Research on the effectiveness of using the additive of break glass in the production of ceramic materials,” vol. 49, no. 3, p. 85, 2024, doi: 10.24412/2079-7958-2024-3-85-96.
[25] “GOST 530-2012 Ceramic brick and stone. General specifications,” Moscow, Russia: Standardinform, 2013, p. 28.
[26] E. Kuldeyev, Z. Zhumadilova, A. Zhagifarov, A. Tolegenova, M. Kuttybay, and A. Alikhan, “Physicochemical properties of silica fume and fly ash from Tau-Ken Temir LLP and Pavlodar CHP for potential use in self-compacting concrete,” *tbus*, vol. 5, no. 1, p. 0076, Mar. 2025, doi: 10.54355/tbus/5.1.2025.0076.
[27] “GOST 7025-91 Ceramic and calcium silicate bricks and stones. Methods for water absorption and density determination and frost resistance control,” Moscow, Russia: Standardinform, 2008, p. 10.
[28] M. L. Jalaluddin, U. A.-A. Azlan, M. W. A. Rashid, and N. Tamin, “Effect of sintering temperatures on the physical, structural properties and microstructure of mullite-based ceramics,” *AIMSMATES*, vol. 11, no. 2, pp. 243–255, 2024, doi: 10.3934/matersci.2024014.
[29] H. M. Hamada *et al.*, “Effect of silica fume on the properties of sustainable cement concrete,” *Journal of Materials Research and Technology*, vol. 24, pp. 8887–8908, May 2023, doi: 10.1016/j.jmrt.2023.05.147.
[30] V. Loryuenyong, T. Panyachai, K. Kaewsimork, and C. Siritai, “Effects of recycled glass substitution on the physical and mechanical properties of clay bricks,” *Waste Management*, vol. 29, no. 10, pp. 2717–2721, Oct. 2009, doi: 10.1016/j.wasman.2009.05.015.
[31] S. M. S. Kazmi, S. Abbas, M. L. Nehdi, M. A. Saleem, and M. J. Munir, “Feasibility of Using Waste Glass Sludge in Production of Ecofriendly Clay Bricks,” *J. Mater. Civ. Eng.*, vol. 29, no. 8, p. 04017056, Aug. 2017, doi: 10.1061/(ASCE)MT.1943-5533.0001928.
[32] Y. Xin *et al.*, “Recycling Crushed Waste Beer Bottle Glass in Fired Clay Bricks,” *Buildings*, vol. 11, no. 10, p. 483, Oct. 2021, doi: 10.3390/buildings11100483.
[33] A. S. C. Morais, C. M. F. Vieira, R. J. S. Rodriguez, S. N. Monteiro, V. S. Candido, and C. L. Ferreira, “Fluorescent Lamp Glass Waste Incorporation into Clay Ceramic: A Perfect Solution,” *JOM*, vol. 68, no. 9, pp. 2425–2434, Sep. 2016, doi: 10.1007/s11837-016-1985-z.
[34] Y. Xin, D. Robert, A. Mohajerani, P. Tran, and B. K. Pramanik, “Transformation of waste-contaminated glass dust in sustainable fired clay bricks,” *Case Studies in Construction Materials*, vol. 18, p. e01717, Jul. 2023, doi: 10.1016/j.cscm.2022.e01717.
[35] V. Karayannis, A. Moutsatsou, A. Domopoulou, E. Katsika, C. Drossou, and A. Baklavaridis, “Fired ceramics 100% from lignite fly ash and waste glass cullet mixtures,” *Journal of Building Engineering*, vol. 14, pp. 1–6, Nov. 2017, doi: 10.1016/j.jobe.2017.09.006.

Information about authors:

Zhanar Zhumadilova – PhD, Associate Professor, Institute of Architecture and Civil Engineering named after T.K. Bassenov, Satbayev University, Almaty 050013, Republic of Kazakhstan, z.zhumadilova@satbayev.university
Maratbek Zhuginissov – Doctor of Technical Sciences, Professor, Institute of Architecture and Civil Engineering named after T.K. Bassenov, Satbayev University, Almaty 050013, Republic of Kazakhstan, m.zhuginissov@satbayev.university
Ruslan Nurlybayev – PhD, Research Professor, Institute of Mining and Metallurgy, Satbayev University, Almaty 050013, Republic of Kazakhstan, rusya_nre@mail.ru

Yelzhan Orynbekov – Candidate of Technical Sciences, Associate Professor, Institute of Architecture and Civil Engineering named after T.K. Bassenov, Satbayev University, Almaty 050013, Republic of Kazakhstan, eljan_79@mail.ru
Aigerim Tolegenova – PhD, Senior Lecturer, Institute of Architecture and Civil Engineering named after T.K. Bassenov, Satbayev University, Almaty 050013, Republic of Kazakhstan, a.tolegenova@satbayev.university
Adlet Zhagifarov – PhD, Senior Lecturer, Institute of Architecture and Civil Engineering named after T.K. Bassenov, Satbayev University, Almaty 050013, Republic of Kazakhstan, a.zhagifarov@satbayev.university

Author Contributions:
Zhanar Zhumadilova – resources, funding acquisition.
Maratbek Zhuginissov – analysis, editing, interpretation.
Ruslan Nurlybayev – concept, visualization.
Yelzhan Orynbekov – editing, interpretation.
Aigerim Tolegenova – analysis, methodology, drafting, data collection.
Adlet Zhagifarov – testing, visualization.

Conflict of Interest: The authors declare no conflict of interest.

Use of Artificial Intelligence (AI): The authors declare that AI was not used.

Received: 25.01.2026
Revised: 03.03.2026
Accepted: 05.03.2026
Published: 27.03.2026